

**Ministry of Transportation
Provincial Highways Management Division Report
Highway Infrastructure Innovation Funding Program**



**TITLE: UAVs for Highway
Mapping and Asset Inspections**

Final Report
September 2020

HIIFP-2018-16

Author(s)	Costas Armenakis and Gunho Sohn with contributions from Evangelos Alexakis-Bousias, Agata Szeremeta, Mahya Jodeiri-Rad, Nacer Naciri, Zahra Arjmandi, Jungwon Kang Geomatics Engineering, GeoICT Lab Department of Earth and Space Science and Engineering, York University
Originating Office	Highway Standards Branch, Ontario Ministry of Transportation
Report Number	ISBN 978-1-4868-5326-7 PDF UAVs for Highway Mapping and Asset Inspections
Publication Date	September 2020
Ministry Contact	Provincial Highways Management Division Executive Office, Ontario Ministry of Transportation 301 St. Paul Street, St. Catharines, Ontario, Canada L2R 7R3 Tel: (905) 704-3998; HIIFP@ontario.ca
Abstract	<p>This research project investigates the use and assessment of low-cost Unmanned Aerial Vehicles (UAVs) for highway mapping applications including topographic mapping, mapping and 3D modelling of bridges, and inspection of bridges for damages, such as crack detection and mapping. Low altitude UAV remote sensing offers a better perspective and coverage over an area and provides the ability for targeted coverage at flexible visiting times.</p> <p>UAV images were taken over the Markham Airport, where the runway and a taxiway were used to simulate highway environments. Various photogrammetric network configurations were tested to assess the level of obtainable accuracies. For asset mapping and inspection UAV images were captured at two highway bridges at Oshawa and St Catharines, Ontario. 3D modelling of the Oshawa bridge has been carried out. For GNSS denied/unreliable environments Ultra-Wide Band (UWB) range multilateration was investigated for UAV localization. For concrete crack detection deep neural convolutional networks were employed.</p> <p>Data collection, processing methods, result and recommendations are presented and discuss in this report.</p>
Key Words	UAV, HWY mapping, Bridge mapping, Low altitude photogrammetric networks, UWB UAV localization, AI-based crack detection, Accuracies
Distribution	Unrestricted technical audience.

Table of Contents

Executive Summary	4
Background and Rationale.....	5
Objectives and Main Tasks	7
Regulations and Safety	8
UAV HWY Mapping – Markham Airport.....	10
Planning of Photogrammetric UAV Aerial Survey	10
Design of Ground Point Targets	13
Ground Coordinate Determination using Land Surveying.....	13
Land Survey Network Adjustment.....	14
Levelling Survey	15
Ground Coordinates Determination using GNSS.....	15
GNSS Data Processing	16
Coordinate Systems and Transformations.....	16
UAV Mapping Systems	17
Execution Of Photogrammetric Surveys	19
Photogrammetric Data Processing	23
Analysis of The Photogrammetric Network Design Configurations	46
Photogrammetric Mapping Products.....	47
UAV Bridge Mapping – HWY 401 / Oshawa Creek.....	49
Planimetric Survey Network.....	50
Vertical Survey Network.....	50
UAV Aerial Survey	50
Photogrammetric Data Processing	53
UAV Bridge Mapping – St Catharines QEW Steel Girder Bridge	63
Bridge Planimetric Survey Network	64
Bridge Planimetric Survey Network Adjustment.....	65
Vertical Survey Network.....	65
Aerial Survey	65
Q-Drone System for HWY and Bridge Inspection	67
Related Works	69
Q-Drone Ssystem	70
System Calibration.....	71
Baseline Positioning Method.....	73
Data Acquisition Results.....	75
Benchmark Data.....	79
Conclusions and Future Works.....	80

Executive Summary	4
Background and Rationale.....	5
Objectives and Main Tasks	7
Regulations and Safety	8
UAV HWY Mapping – Markham Airport.....	10
Planning of Photogrammetric UAV Aerial Survey	10
Design of Ground Point Targets	13
Ground Coordinate Determination using Land Surveying.....	13
Land Survey Network Adjustment.....	14
Levelling Survey	15
Ground Coordinates Determination using GNSS.....	15
GNSS Data Processing	16
Coordinate Systems and Transformations.....	16
UAV Mapping Systems	17
Execution Of Photogrammetric Surveys	19
Photogrammetric Data Processing	23
Analysis of The Photogrammetric Network Design Configurations	46
Photogrammetric Mapping Products.....	47
UAV Bridge Mapping – HWY 401 / Oshawa Creek.....	49
Planimetric Survey Network.....	50
Vertical Survey Network.....	50
UAV Aerial Survey	50
Photogrammetric Data Processing	53
UAV Bridge Mapping – St Catharines QEW Steel Girder Bridge	63
Bridge Planimetric Survey Network	64
Bridge Planimetric Survey Network Adjustment.....	65
Vertical Survey Network.....	65
Aerial Survey	65
Q-Drone System for HWY and Bridge Inspection	67
Related Works	69
Q-Drone Ssystem	70
System Calibration.....	71
Baseline Positioning Method.....	73
Data Acquisition Results	75
Benchmark Data	79
Crack Detection Using Deep Neural Convolutional Network	83
Related Works	85
Methodologies	87
Experimental Setup	90
Conclusions and Future Works	100
Conclusions and Recommendations	101
Acknowledgements	104

Bibliography	105
Appendix A: Markham Ground Survey.....	113
Ground Coordinates Determination using Land Surveying	113
Land Survey Network Adjustment.....	113
Levelling Survey	114
Ground Coordinates Determination using GNSS.....	115
Data Collection	116
Data Processing Procedure	117
Coordinate Systems and Transformations.....	117
Appendix B: Oshawa Bridge Ground Survey	124
Planimetric Survey Network.....	124
Vertical Survey Network.....	125
Appendix C: St. Catharine's Bridge Ground Survey	130
Bridge Planimetric Survey Network	130
Planimetric Survey Network Adjustment.....	131
Vertical Survey Network.....	132
Appendix D: GNSS Surveying St Catharines & Oshawa Bridges	137
Data Collection Procedures	137
Data Processing Procedure	138
Appendix E: Photos From The Bridges.....	142

Executive Summary

Low altitude UAV remote sensing has been used to assess the use of low-cost UAV platforms as a cost-and time-effective alternative approach for highway topographic and engineering products. UAV images over the UAV Range of the Markham Airport have been captured, where the runway and a taxiway were used to simulate highway environments. The planning and execution of the UAV aerial survey are analysed, and the determination of the mission specifications is given. This followed by the establishment of the ground targeted point network and the execution of the UAV flights. Several photogrammetric configurations were tested using two different UAV platforms equipped with two different cameras. The processing of the UAV images to obtain 3D georeferenced data was based on photogrammetric bundle adjustment with self-calibration method.

The results were analysed with respect to the obtainable accuracies. Photogrammetric products such as digital point clouds, orthoimage mosaic and contour generation were produced. Recommendations are provided with respect to the flying height, the image overlaps, the camera lens angular field of view, the accuracy of ground control pints and the exterior orientation parameters, and the use of check points. As the UAV capture large number of images their processing requires time and significant computing capacity.

The potential of UAV mapping and inspection of HWY assets, such as bridges, was also investigated as part of this project. UAV images were captured at two highway bridge sites: the HWY 401 Oshawa Creek Cast Concrete Bridge and the Span 9 of the St Catharines QEW Steel Girder Bridge (section of the Garden City Skyway). Again, two different UAV platforms with two different camera sensors were employed. In both sites the UAV were piloted manually due to fact that the flights were under the bridges and therefore these were GNSS denied environments. Ground point networks of targeted points were established in both sites. For the Oshawa bridge nine UAV flights were executed using one of the UAV platforms. All nine flights were simultaneous adjusted as image blocks (image chunks). This photogrammetric configuration leads to the production of georeferenced engineering products. For example, in the Oshawa bridge case, the UAV images were used to generate a georeferenced 3D model of the shape of the cement bridge tunnel in the forms of 3D point clouds of variable density and texture mapped georeferenced representations of the bridge.

For GNSS denied and/or unreliable environments the Ultra-Wide Band (UWB) range multilateration methods was investigated for the UAV localization. For bridge damage assessment such as concrete crack detection deep neural convolutional networks were employed and investigated.

Recommendations are provided on the selection of camera sensor and photogrammetric network design configuration in order to meet the engineering mapping accuracies required by the MTO specifications.

Background and Rationale

Aerial data collection is a way to obtain a better perspective and coverage over an area and provides the ability for targeted coverage at flexible visiting times. Traditional air-surveys have certain limitations, such as high mobilization and flying costs, time of flying, flight restrictions and size of coverage. The emerging small Unmanned Aerial Vehicles (UAVs) and specifically Unmanned Aerial Mapping Systems (UAMS) are now enjoying wide popularity, featuring different types of platforms, for numerous civilian applications such as scientific, commercial, public safety, and recreational activities. They are effective aerial platforms carrying imaging and ranging sensors for geospatial data collection. Usually UAMS are used for generating rapid 3D mapping products over relatively small, remote and inaccessible areas. Remotely piloted mobile mapping systems and, particularly, small aerial platforms are causing a paradigm shift in the field of geomatics and transforming 3D geospatial data acquisition and 3D mapping. The growing use of small and light-weight UAVs are changing the applications of geomatics and creating new and innovative opportunities for exploring, measuring and modelling outdoor and indoor environments. UAVs compliment, and in many cases replace, total stations and laser scanners, and operate as flexible aerial mobile survey systems.

UAVs can be used in many diverse applications. These include mapping (3D point clouds, DSM, orthoimages), cadastral surveys, land-cover/land-use monitoring, corridor mapping (inspection of pipelines and power lines), volumetric surveys, traffic monitoring, landslides, mining, precision farming, forest fire fighting, disaster management, search and rescue operations and emergency response, traffic and accident monitoring, conservation and biodiversity monitoring, including wildlife and forest tree diseases, mapping and monitoring of remote arctic areas (glacier studies and ice flow), geophysical exploration, surveillance, border patrol, and archaeology. Other geomatics applications include terrain following at specific altitude and following of linear features such as roads, rivers and pipelines, infrastructure inspections, thermography of buildings, change detection based on temporal observations, tailing ponds, pre-disturbance and reclamation site mapping, and assessment and planning. The ability of small UAVs to acquire high resolution data is clearly a valuable tool for new techniques in mapping and surveying. Capturing images and laser scanner data and using advanced computer photogrammetric and feature extraction approaches can generate products that can meet accuracy standards suitable for engineering-level mapping and surveying. The quick launch of the UAVs together with the rapid capture of the aerial images and the automated data processing result in significant time and cost savings compared to the field surveying methods. The availability of commercial and open source software offers automated and analytical processing tools and total solutions to exploit, analyse the data and generate location-based products. To process the large number of images effectively for deriving the final geospatial products, a high level of automation is recommended to ensure rapid data processing and product delivery. Fast data processing with fully automatic workflow for operations such as multi-view

image matching, bundle adjustment, 3D point clouds, DSM and 2D orthoimages/mosaics can be performed both with internet accessible and with commercially available software.

The MTO Geomatics Section has already recognized the potential of using UAVs for generating topographic and engineering products. It has employed two relatively inexpensive UAV units that can be mobilized quickly and has successfully created a number of orthoimages, digital terrain models and dense 3D point cloud models that can be used for preliminary engineering design. With suitable equipment, procedures, and weather, some of these products may approach or meet MTO standard accuracies for detailed engineering design needs. However, accuracy testing has been limited, mostly only over low-risk areas such as aggregate pits, farms, and a former landfill park, with limited flights and data collection over roads, highway segments and infrastructure element, such as bridges and road furniture assets such as COMPASS cameras poles.

MTO is also interested in studying the use of UAV for bridge inspection considering that in Ontario each bridge is inspected every 2 years. For bridges that are low to the ground where the inspector is able to see the bridge elements from a close distance, traditional inspections are effective. MTO currently does close-up visual inspections using under-bridge inspection trucks with telescopic buckets. There is potential to use UAV inspection technology in certain circumstances where it is difficult to view the bridge closely or where heavy traffic makes lane closures difficult. Same if the bridge is over water. However, MTO is seeking to gain more experience to determine both the potential uses and limitations of UAV inspection. Bridge engineers need to understand what parts of a bridge may be inspected by UAVs, what areas of a bridge are difficult to access by UAVs, and what type of information is possible to obtain. Understanding of practical issues such as legal restrictions on flights especially when inspecting bridges in urban areas or when UAVs may visually distract road users is also an important issue for MTO.

Recognizing this need MTO has issued a HIIFP 2018 call to investigate the use of UAV in assessing their use in highway mapping and infrastructure asset assessment such as bridges where that use of UAV-based remote sensing has the potential of providing safer and cost-effective inspections using multi-viewing sensor systems, safely caged UAV, and obstacle detection and avoidance technologies.

Objectives and Main Tasks

In this work, we investigate the use of UAVs as a cost- and time-effective alternative for the mapping and monitoring of highways.

Objective 1 - Accuracy assessment of UAV-based highway mapping. UAV images over the UAV Range of the Markham Airport have been captured, where the runway and a taxiway were used to simulate highway environments.

Objective 2 - UAV-based highway assets inspection. UAV images and GeoSLAM point data have been captured at two bridges, at Oshawa and St Catharines, Ontario. 3D modelling of the Oshawa bridge has been carried out based on the integration of various flight lines to achieve a 360° view.

Objective 3 - Assessment of new technologies. New UAV technologies have been investigated and introduced regarding safety, rapid and automated processing, autonomy of UAV operations, UWB UAV localization, AI-based crack detection and crack georeferencing. These will be related mostly to the intermediate and high-end hardware and software technologies.

Recommendations are provided on minimum, intermediate and high-end hardware and software requirements along with best practices to conduct UAV highway mapping.

Regulations and Safety

Everyone's safety is a paramount requirement for this project due to the safety risks involved by operating UAV and conducting experiments in the proximity of or even on highways segments. The operation of UAVs is regulated by Transport Canada based on the UAV platform, test location, and piloting and control.

Safety risk management has been exercised during the field works of this project. As UAV users we obtained permission by Transport Canada by applying for Special Flight Operations Certificate (SFOC) (Fig. 1 and 2). Proper insurance was also obtained with the support of York University. Markham Airport has its own UAV Test Range certification from Transport Canada.

1.0 Operation Information

1.1 UAV Operation Site

Table 1: Summary of UAV Operation Site Details

Date of Operation	
Location	Toronto/Markham Airport (CNU8) 10953 ON-48 Markham, ON L3P 3J3 Geometric Centre Coordinates: (43°56'09" N, 79°15'44" W) Elevation 807'
Airspace Class	Class B-1 Class C-2,3,4,5,6
Operator	Toronto/Markham Airport Inc. (905-642-4536/416-720-1465)
Mandatory Frequency	
FIC	London 866-WXBRIEF or 866-541-4104

All flight operations will be conducted on Markham Airport property, indicated through the yellow polygon in the figure below. Permission has been granted by the airport owner to use the facility (letter attached).

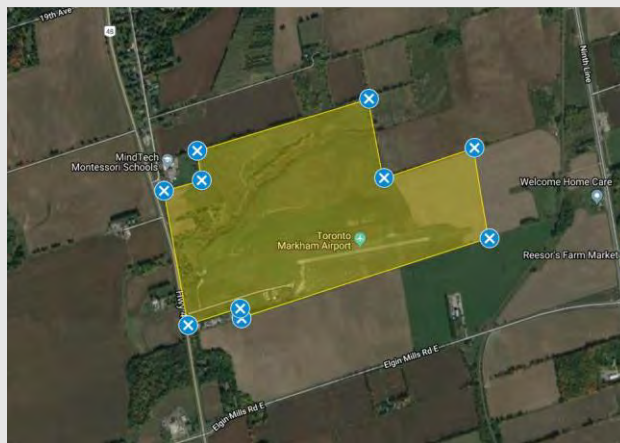


Figure 1: Markham Airport Property and Boundary of Flight Operation

Figure 1 – SFOC application – UAV Operation site at Markham Airport

SPECIAL FLIGHT OPERATIONS CERTIFICATE CERTIFICAT D'OPÉRATIONS AÉRIENNES SPÉCIALISÉES				
	CANADA		Transport Canada	Transports Canada
SFOC No. / COAS n° : ATS-19-20-00009010	Name of Responsible Person / Nom de la personne responsable : COSTAS ARMENAKIS			
Effective Date (YYYY-MM-DD) / Date effective (AAAA-MM-JJ) : From / Du : 2019-05-13 To / Au : 2019-05-31	Legal Name / Dénomination sociale : YORK UNIVERSITY DEPARTMENT OF EARTH AND SPACE SCIENCE ENGINEERING			
This Certificate will cease to be valid on the date which regulations pertaining to Small UAVs operated within visual line-of-sight come into force in the Canadian Aviation Regulations. Ce certificat cessera d'être valide à la date à laquelle les règlements relatifs aux petits UAV exploités en visibilité directe entreront en vigueur dans le Règlement de l'aviation canadien.	Operator Address / Adresse de l'exploitant : 4700 KEELE STREET TORONTO, ON M3J 1P3			
	Telephone / Téléphone : (416) 736 - 2100 EXT 55221, (647) 986 - 1553			
	E-mail / Courriel : armenc@yorku.ca			

Figure 2 – SFOC – UAV Operation site at Markham Airport

UAV HWY Mapping – Markham Airport

The data collection for highway mapping is based on data collected by imaging and/or ranging sensors carried by the UAV mapping platforms. Considering that the 3D georeferenced mapping products are highly dependent on these operations, the following tasks for the highway mapping components were performed:

- a) planning of the UAV flight mission,
- b) execution of the ground and UAV aerial surveys using two UAV mapping platforms
- c) execution of photogrammetric triangulations for determination of the position and orientation of the camera and the coordinates of the object points
- d) generation for digital surface models (point clouds)
- e) generation of orthoimages
- f) assessment of the results obtained
- g) recommendations

The Markham Aerodrome was used as general test facility. The Markham Aerodrome has been approved by Transport Canada as site for flying and testing UAVs. The UAV aerial mission was conducted on May 29, 2019.

PLANNING OF PHOTOGRAMMETRIC UAV AERIAL SURVEY

The aerial mission for the collection of remotely sensed data is a very important operation as the entire project is highly depended on the quality of the aerial data. Planning and executing the aerial mission are therefore critical operations. In the planning phase the specifications of the aerial survey are determined. This includes the flight plan based on the landscape and land-cover of the study area, the ground spatial resolution, the design and size of the ground point targets, the sensor used, the quality of data capture by the sensor, the flying altitude, the scale, the ground coverage per image, the forward and side overlap, the allowable tilts, the speed of the small UAVs and environmental aspects such as wind velocity and sun angle. Design parameters are the UAV trajectory that includes direction, altitude, speed, waypoints, forward and side overlaps, camera triggering, and the ground sampled distance (GSD) or ground resolution.

The higher we fly with the same UAV mapping platform, the more economical is (e.g., larger ground coverage, less images, less field and processing time). The lower we fly the better the accuracies obtained. Two UAV flights at different flying altitudes (namely 40m and 80m) were conducted over the runway and taxiway areas of in Markham airport, in order to assess the accuracies obtained based on two different image scales. Two low-cost UAV mapping systems we used equipped with two different RGB cameras. The first one was the DJI Phantom II Vision + and the second was the DJI M100.

Based on the camera literature, an approximate camera focal length of 5.5mm was used for the planning phase. Using the initial focal length, we determined the ground resolution of a given pixel to be approximately 1cm for the 40m flight height and 2cm for the 80m flight height. Taking into account the battery life limitations of our UAV, we split each flight into two separate flights/mapping tasks: (a) the mapping of the main runway and (b) the mapping of a smaller road (taxiway) that leads to the main runway. Thus, the total number of planned flights based on the region to be mapped and the flight height for Phantom II Vision+ was set to 4.

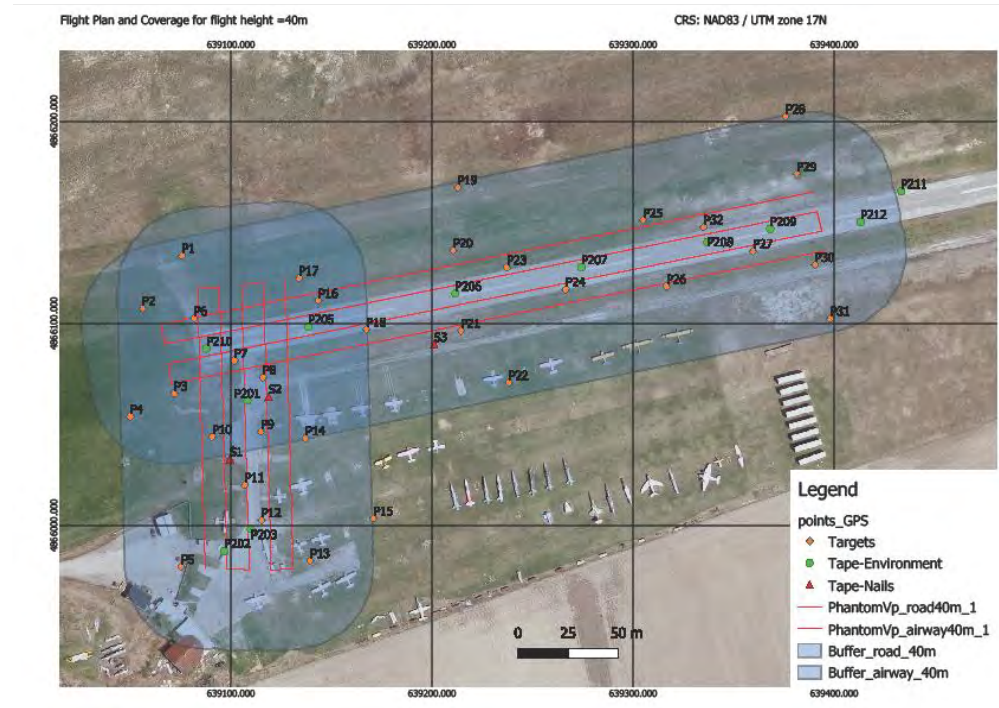


Figure 3 – Flight plans and coverage areas for UAV flight height equal to 40m

The overlap between images, both for the front and the side lap, was selected to be 80%. In order to produce the final flight paths, we have used the Survey tool of the QGroundControl software and QGIS to refine the paths and select the locations for the Ground Control Points (GCPs). The GCPs' locations were selected in such a way as to cover the whole mapping area (for all four flights)- with special attention being given to covering the boundaries of each flight task - and to provide redundant observations for the photogrammetric bundle adjustment solutions. Figures 3 and 4 respectively present the flight paths and coverage areas for each flight as well as the location and distribution of the ground coordinated and targeted points. Points represented with an orange colour were implemented using targets, while points implemented using a nail and duct tape are represented with a red colour. The green circles depict points that were implemented using landmarks (like corners or intersections of white lines), as it was not possible to use nails on the runway or the road. The image footprint coverage area was determined by the camera's image resolution and the pixel size on the ground and was estimated to be around

40mx40m for the 40m flight height and 85mx85m for the 80m flight height.

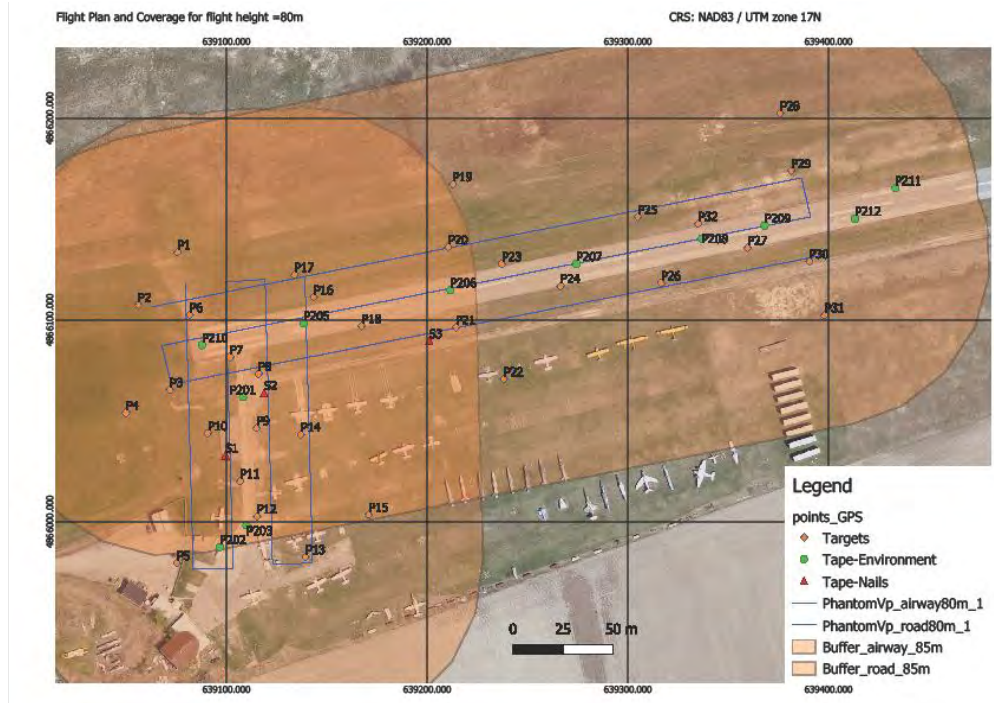


Figure 4 – Flight plans and coverage areas for UAV flight height equal to 80m

Table 1 presents the survey area, the number of images, the time interval, and the trigger distance between sequential images for each and every flight plan we have prepared.

Table 1 – Flight Plan Overview

Runway	Phantom 2 Vision+ (H:40m) Stats	(Overlap 80% Front and Side)
	Survey Area (m ²)	11977
	Photo count (#)	182
	Photo interval (sec)	1.5
	Trigger Distance (m)	7.44
	Phantom 2 Vision+ (H:80m) Stats	(Overlap 80% Front and Side)
	Survey Area (m ²)	16541.5
	Photo count (#)	69
	Photo interval (sec)	3
	Trigger Distance (m)	14.88

Taxiway	Phantom 2 Vision+ (H:40m) Stats	(Overlap 80% Front and Side)
	Survey Area (m ²)	8606.1
	Photo count (#)	125
	Photo interval (sec)	1.5
	Trigger Distance(m)	7.44
	Phantom 2 Vision+ (H:80m) Stats	(Overlap 80% Front and Side)
	Survey Area (m ²)	10127.5
	Photo count (#)	52
	Photo interval (sec)	3
	Trigger Distance (m)	14.88

Note: These values estimated for planning. The actual ones may be slightly different.

DESIGN OF GROUND POINT TARGETS

Using the initial focal length, we determined the ground resolution of a given pixel to be approximately 1cm for the 40m flight height and 2cm for the 80m flight height. Based on the larger pixel ground resolution we have decided to create targets of size 40cm x 40cm (Fig. 5), which translates into targets having a size of approximately 20pixel x 20pixel in the images captured from 80m flight height. We have also included a target number ID to facilitate the surveying crew and eliminate blunder naming errors in the ground surveying measurements (Fig. 5).

GROUND COORDINATE DETERMINATION USING LAND SURVEYING

In the Markham survey area, 44 points were surveyed using GNSS methods, while a total of 47 points were surveyed using a total station. For the ground surveying task, a TS11 Leica Total Station has been used. In all three locations a small number of points has been selected to be used as set-up/station points. A traverse of 4 points was set for the total station survey. This was between points S1, 210, S3, and 208. Initially, it was desired to have a network of 5 points (including station S2). However, due to observations errors to and from this station, it was omitted and disregarded from further observations. When a single point was observed multiple times throughout the traverse (that is, from different setups), the point's computed coordinates were averaged.

The station points have been solved in all cases in a local coordinate system as a network

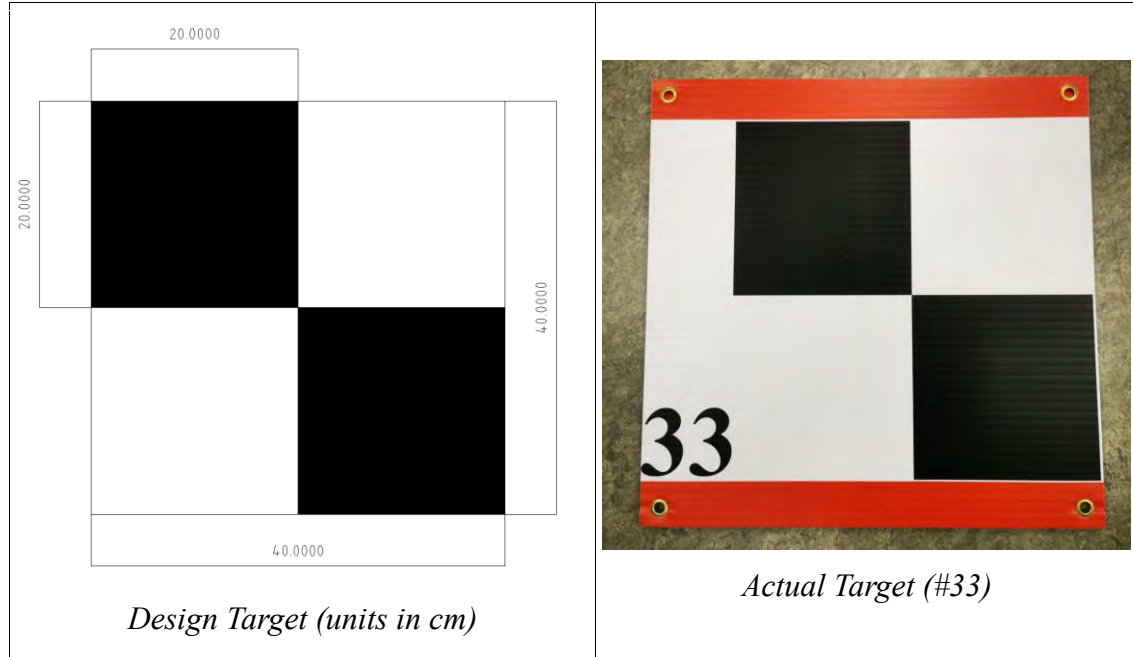


Figure 5 – Design and actual targets

with the minimum number of constraints, without taking into account the coordinates derived from the GPS observations. The rest of the points have been measured from multiple stations and their coordinates have been averaged.

LAND SURVEY NETWORK ADJUSTMENT

To perform the network adjustment and determine the coordinates of the 4 control points, a total of 23 observations were used – 7 directional angles, 8 zenith angles, and 8 slope distances. The system had 12 degrees of freedom, with a total of 12 unknowns (the XYZ of each of the S1, 210, and S3 control points). It was assumed that the coordinates of point 208 were fixed at 1000m, 1000m, 1000m. To perform traverse network adjustments, GNU Gamma open-source adjustment software was used. In each survey region case, a solution was determined in local coordinates. Then, applying tachymetric techniques, the local coordinates of the remaining survey points were determined. Once the locally defined coordinates of each network's points were determined, a transformation was performed to bring the network to the desired coordinate system.

Solving the network at a confidence level of 95% resulted in local coordinates for the remaining control points. The mean errors and parameters of the error ellipses of the remaining control were determined and are given in Table 2.

Table 2 – Mean Errors and Parameters of the Error Ellipses of Markham (Local) Traverse Network

Point	mp (mm)	mxy (mm)	Mean Error Ellipse			Confidence Error Ellipse		g
			a (mm)	b	Alpha (gons)	a' (mm)	b'	
210	2.8	2.7	3.8	0.0	100.0	10.5	0.0	0.0
S1	6.9	4.9	5.2	4.6	99.5	14.4	12.8	0.0
S3	5.3	3.8	3.8	3.7	134.3	10.7	10.3	0.0

LEVELLING SURVEY

The determined CGVD28 HT2_2010v70 system orthometric heights (from the coordinate conversion process) of the GNSS surveyed points were used to transfer elevation to the remaining observed points through either differential levelling or trigonometric levelling techniques.

In the Markham survey area, spirit levelling was performed in two loops between the points outlined below. The first was conducted in a single-run manner, while the second in a double-run.

The GNSS-based orthometric elevation of point S1 was propagated through to the remaining loop points, as per standard differential levelling techniques (that is, height differencing and adjustment). The determined height of point S3 found in loop 1 was then treated as the fixed elevation in loop 2 differential levelling was applied again. In both cases, adjustments to the raw determined heights were applied based on the number of setups in the levelling loops.

Having orthometric heights for all points of the traverse (S1, 210, 208, S3), the remaining orthometric heights of surveyed points were determined by applying trigonometric levelling techniques on the total station survey data. The previously determined orthometric heights at the traverse station points were used as the instrument setup elevations in the remaining levelling calculation process.

As GNSS data was collected for most surveyed points, the total station derived and GNSS orthometric heights were compared. Unfortunately, a random discrepancy appears between the two determined heights. The cause of this is unclear.

Computed orthometric elevations are provided in Appendix A

GROUND COORDINATES DETERMINATION USING GNSS

GNSS surveying of the positions of these targets was performed using post-processed relative positioning. To do so, the Leica GS15 receivers have been used.

First, stakeout of the GCPs was performed. Approximate positions of the GCPs were already pre-determined and so the stakeout function in the Leica receivers were used to place the targets in their pre-determined spots. To do so, the GCP coordinates were converted to the right format before inputting them into the Leica receivers. The latter then gives directions that lead to the spot where the GCP should be placed. This was repeated until all GCPs were placed around the highway.

For the surveying part, one of the receivers has been set up as a base station (target “S1”) which was left running for the whole duration of the data collection.

GNSS DATA PROCESSING

Following the field observations, (Fig. 6), the data was extracted from the Leica receivers using USBs and sorted into a computer. A first check was done to make sure that all the points have been extracted properly and that they are properly named for the processing. Once that was done, all the points were imported into the Leica Infinity software. Point “S1” was set up as a base station in the software while the rest of the points were set up as rovers. The RTK solution was then initiated and reports for each of the files were generated by the software.

The next step was to extract the final positions from the reports as well as other relevant information, compute the 2D and 3D standard deviations and put everything together into one document.



Figure 6 – Ground coordinates determination using GNSS

COORDINATE SYSTEMS AND TRANSFORMATIONS

The coordinates found through the GNSS surveys of each site were converted from the WGS84 coordinate system to NAD83(CRS)v6 2010 MTM Zone 10 system using Natural Resources Canada’s TRX tool. As suggested by NRCan, WGS84 was considered equivalent to the ITRF2008 reference system. When inputting the surveyed latitude,

longitude and ellipsoid height values, the ITRF2008 system at epoch 2010-01-01 was used. The orthometric heights at such points were converted from GNSS derived ellipsoid height using Natural Resources Canada's GPS-H tool. The previously derived NAD83(CSRS) MTM Zone 10 coordinates were used as input. The vertical datum was selected to be CGVD28, while the geoid model as HT2_2010v70.

Computed coordinates are provided in Appendix A.

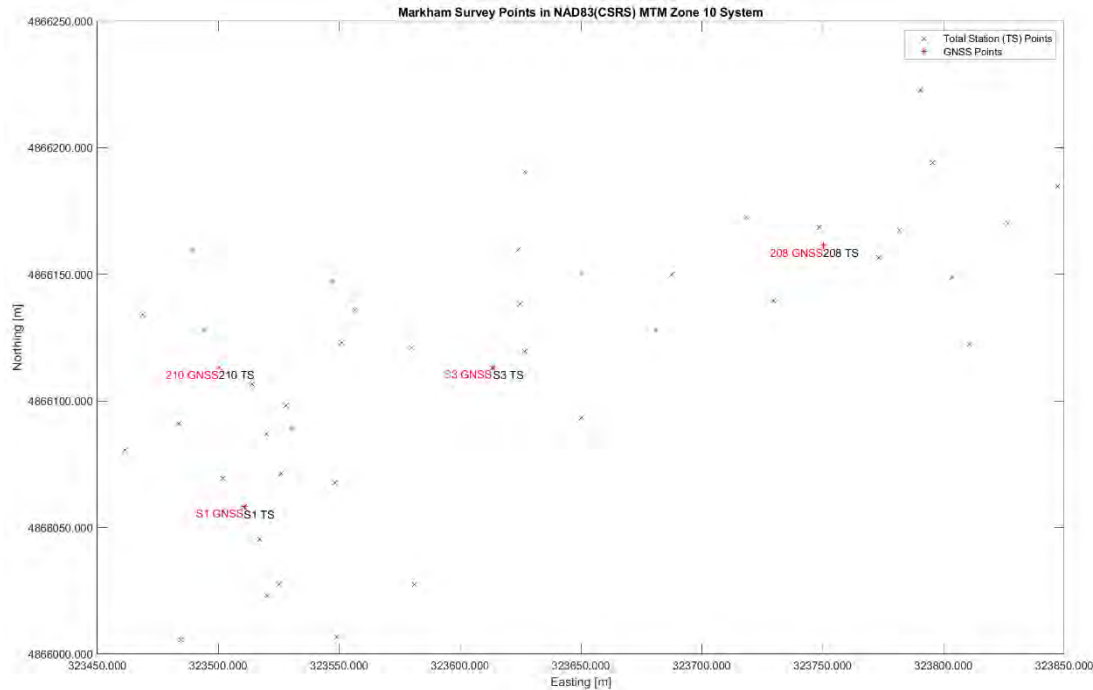


Figure 7 – Transformed Markham Area Total Station Coordinates Compared Against GNSS Measured Points

UAV MAPPING SYSTEMS

For the HWY UAV mapping part of this project, we use two low-cost UAV platforms.

1) DJI Phantom Vision 2+ system. The system comes equipped with a camera mounted onto a 3-axis gyrostabilized gimbal. The camera can record video in 1080p HD video at 30 frames per second, or be set into image capture modes, triggered manually, or at regular intervals.

- Weight: 1.242 kg
- Max Speed: 15 m/s
- Diagonal motor-to-motor distance: 350mm
- Onboard GPS
- Onboard Compass

- Controlled from an RC controller or pre-programmed flight plan
- Ground station software for real-time navigation



Figure 8 – The DJI Phantom Vision 2+

2) DJI M100 system: We equipped the system with a GoPro HERO5 camera mounted on the proper gimbal.

- Weight (no payload): 2.355 kg
- Max Speed: 22 m/s
- Diagonal motor-to-motor distance: 650mm
- Onboard GPS
- Onboard Compass
- Controlled from an RC controller or pre-programmed flight plan
- Ground station software for real-time navigation



Figure 9 – The DJI M100

EXECUTION OF PHOTOGRAMMETRIC SURVEYS

Two UAVs were flown over the Markham Airport region – the DJI M100 and DJI Phantom 2 Vision+ (Fig. 10). The M100 was equipped with a GoPro Hero 5 Black camera mounted on an EVO SS gimbal, while the Phantom 2 Vision+ was equipped with its default, manufacturer provided camera Vision FC200 and gimbal. Both cameras enabled the geotagging of captured images. The UAVs flew over the airport runway and taxiway in the flight configurations listed in Table 3.

Due to UAV battery complications, it was necessary to divide the Phantom 2 Vision+ flight at 40m into two sub-flights. Captured images from both parts of the flights were then combined to form one dataset during image processing. Furthermore, due to complications with the flight planning software at the time of survey, an 80m flight with this UAV over the runway could not be executed.

To plan the flight path and fly each of each of the UAVs, Litchi's Mission Hub software was used for the Phantom UAV, while Pix4D software was used for the M100. Both UAV mission software were used on a mobile platform. In the former, the survey lines were automatically generated based on the entered coordinates of the survey line end points (determined from previous flight planning calculations). Flight speed of the Phantom UAV was set to approximately 6km/h and 12km/h for altitudes of 40m and 80m, respectively. Through the software, the UAV was set to hover over the endpoint of survey line as the camera was orienting itself for the next survey line. Once oriented and turned to face the appropriate direction, the UAV continued along its path. Sample flight paths from the Phantom UAV over the taxiway at the two altitudes are shown in Figure 11 below.

Table 3 – UAV Flight Configurations of Markham Airport

UAV	Coverage Area	Altitude (m)
M100	Runway	40
		80
	Taxiway	40
		80
Phantom 2 Vision+	Runway	40
	Taxiway	40
		80

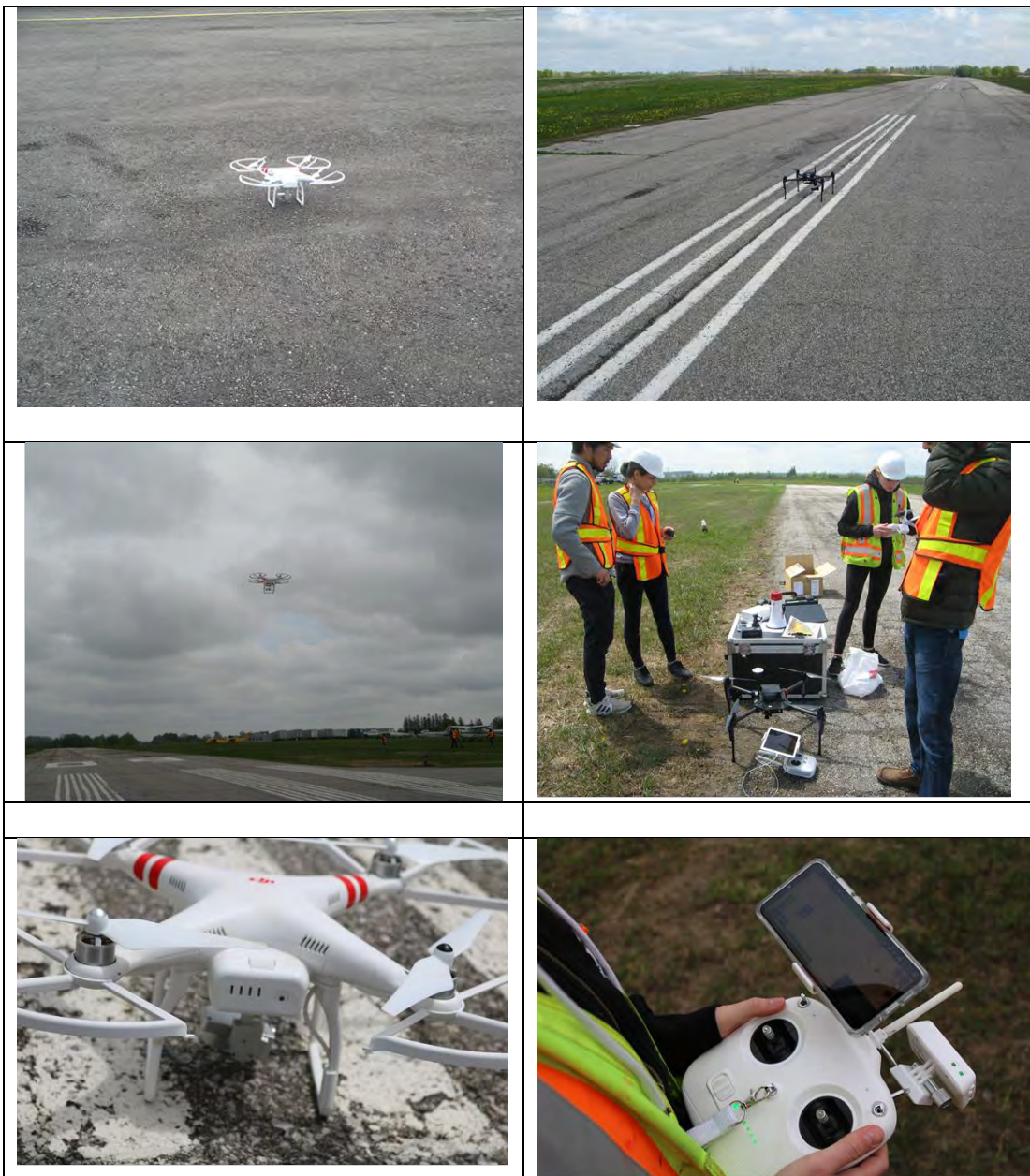


Figure 10 – Field UAV operations at Markham Airport



Figure 11 – Phantom 2 Vision+ Taxiway Flight Path at 40m (L) and at 80m (R)

To ensure the desired 80% overlap between sequential images, the Phantom 2 Vision+ was set to capture new images every 1.5 seconds for all its flights. Unfortunately, the camera could not be better configured to take images at an appropriate frequency for the desired overlap at 80m altitudes. This was expected to be due to the increased UAV speed and minimum delay between images by the camera system. Therefore, the overlap in images of the Phantom's 2 Vision+ 80m flight is slightly greater than 80%. Nevertheless, these parameters resulted in the number of captured images provided in Table 4.

It should be noted that images were captured prior to the start of the survey. That is, when the UAV was flying to its desired altitude or its starting waypoint on the survey line. As such, these image counts are inclusive of images which would not be used in final processing. Unfortunately, during the M100 survey of the runway at an altitude of 40m, the gimbal seemed to have encountered a motor problem resulting in vibrations of the system. This may have affected the quality of some of the images taken.

Table 4 – Total Number of Images Captured Per Flight

UAV	Flight Region	Altitude (m)	Number of Images Captured
M100	Runway	40	2358
		80	764
	Taxiway	40	630
		80	487
Phantom 2 Vision+	Runway	40	351 (Part 1: 171; Part 2: 180)
		80	182
	Taxiway	40	110



Figure 12 – Phantom sample images taken from 40m and 80m





Figure 13 – M100 sample images taken from 40m and 80m

PHOTOGRAMMETRIC DATA PROCESSING

All of our UAV images were captured at the UAV Range of the Markham Airport, where we have used the runway and a taxiway to simulate highway environments. Our main objective is the assessment of the horizontal and vertical mapping accuracy that can be achieved through a photogrammetric solution of the RGB imagery data collected from two low cost UAV systems in an attempt to evaluate their use for highway mapping applications. Based on the available UAV systems, the process followed for the photogrammetric triangulation -determination of the camera exterior parameters and the object coordinates - was GCP-based (indirect sensor orientation approach).

Two coverage areas were selected based on the nature / texture of the paved surfaces. The one is the runway and the other is the taxiway image blocks. To examine the impact of the image scale the areas were surveyed from two different altitudes of 40m and 80 m respectively. Due to the relative flat terrain of the airport a combined triangulation consisting of images from both altitudes was also performed. The two UAV platforms used were also equipped with different cameras (different image plane size, nominal focal lengths, lens distortions).

The photogrammetric triangulation methods used was the rigorous approach of photogrammetric bundle block adjustment with camera self-calibration. The Agisoft MetaShape commercially available software was used. The bundle adjustment solution applied is the Structure from Motion (SfM) type which solves the camera pose, the camera calibration parameters, and scene geometry simultaneously and automatically, using a highly redundant bundle adjustment based on matching features (point) on multiple overlapping images. The approach is most suited to block of images with high degree of overlap that fully capture three-dimensional landscape of the scene viewed from a moving sensor or from an array of several camera positions.

The SfM photogrammetric triangulation can be performed with or without ground / object

control points. In the first case the results are georeferenced in GCP space, while in the second case the results are in the image / model space. In the latter we can still transfer the results of the bundle adjustment to the georeferenced space via a 3D similarity transformation. Figure 14 shows a typical workflow diagram of the SfM steps.

In most cases the UAVs carry small non-metric cameras. Therefore, the proposed solution is a simultaneous bundle adjustment with self-calibration. The Agisoft Metashape supports two major types of camera: frame camera and spherical camera. Frame cameras have been used in this work, thus for the estimation of camera interior orientation parameters the information on approximate focal length (pix) is required. To calculate the focal length value in pixel its focal length in mm along with the sensor pixel size in mm should be known. The software usually identifies the type of the camera used and considers the specified camera calibration parameters as the initial values, and these values are refined later during the photo alignment operation.

The camera calibration parameters are:

- fx, fy: focal length in x- and y-dimensions measured in pixels.
- cx, cy: principal point coordinates, i.e. coordinates of lens optical axis interception with sensor plane.
- Skew: skew transformation coefficient.
- k1, k2, k3, k4: radial distortion coefficients.
- p1, p2: tangential distortion coefficients.

The characteristics for a successful self-calibration bundle adjustment network are:

- Multi image, highly convergent photogrammetric network
- Depth variation in the object space
- Highly redundant point determination (point determination from 6 or more rays)
- High image measurement accuracy (about 0.3 pixel for targetless points; about 0.1 pixel for targeted points).

Considering the very low terrain relief at the Markham Airport, large forward and side overlaps were used. As well as images from different flight altitudes were merged to one bundle solution to introduce scale variation between images. The photogrammetric process followed is shown in Figure 15 and its steps are given below:

- entry of the images
- entry of GCP, EOP, if used (called markers in the Agisoft MetaShape)
- measurement of the image coordinates of the marker points (GCP),
- keypoint extraction for image matching
- image sensor model reconstruction (image alignment) using iterative bundle adjustment with camera self-calibration
- sparse and dense point cloud generation
- TIN and or GRID DSM generation
- orthoimage /mosaic generation

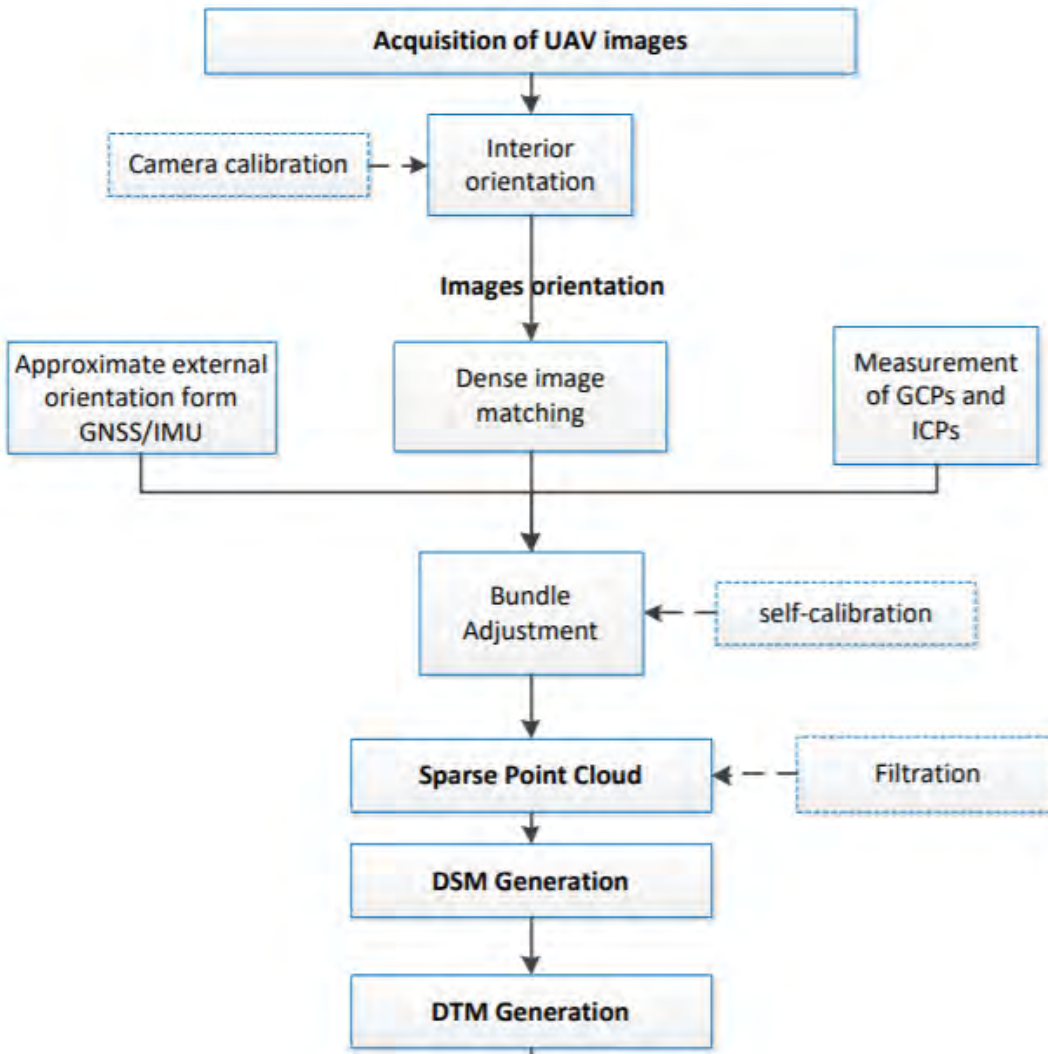


**Figure 14 – Typical Structure-from Motion workflow
(Wierzbicki and Nienaltowski, 2019)**

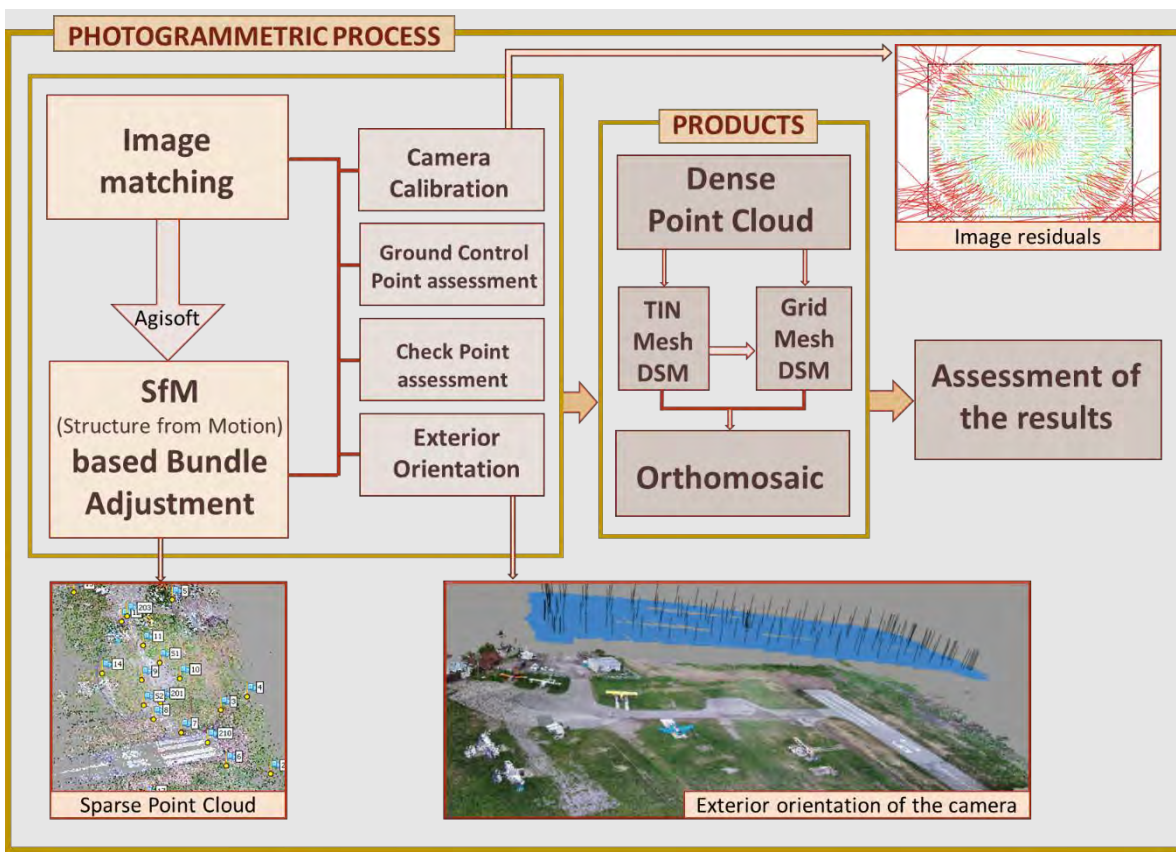


Figure 15 – Photogrammetric process

A significant number of configurations was executed based on the different UAV and their cameras, the two altitudes, the different number and distribution of GCP and CHK points, and the determination of the ground point coordinates either by topographic land surveying or by GNSS methods. Due to the large number of images and the various configurations, the execution of the photogrammetric process took significant computer run time to complete based on the available resources. The X, Y, Z accuracy of the ground points used was set to 2cm or 2.5cm, while the parameters of the exterior orientation were treated as free parameters (very low positional and angular accuracies). The accuracy of the image measurements was set to 0.3 pixels.

The following eight (8) representative photogrammetric network configurations are presented in this report:

Table 5 – Representative photogrammetric configurations

Configuration	Platform	Altitude (m)	Area	GCP determination
1	Phantom	40	taxiway	surveying
2	Phantom	80	taxiway	surveying
3	Phantom	80	taxiway	GNSS

4*	Phantom	40+80	taxiway	surveying
5	Phantom	40	runway	surveying
6	Phantom	40	runway	GNSS
7	M100	40	taxiway	surveying
8	M100	80	taxiway	surveying

*Configuration 3 combines images from different flight heights

The results for each configuration are given next.

Configuration 1: Phantom, 40m, taxiway

UAV	Nominal Altitude of Images	Area	Images	Ground Coordinates	GCP 3D Accuracy
Phantom 2V+ Vision FC200	40m	Taxiway	161	Surveying	2.5cm

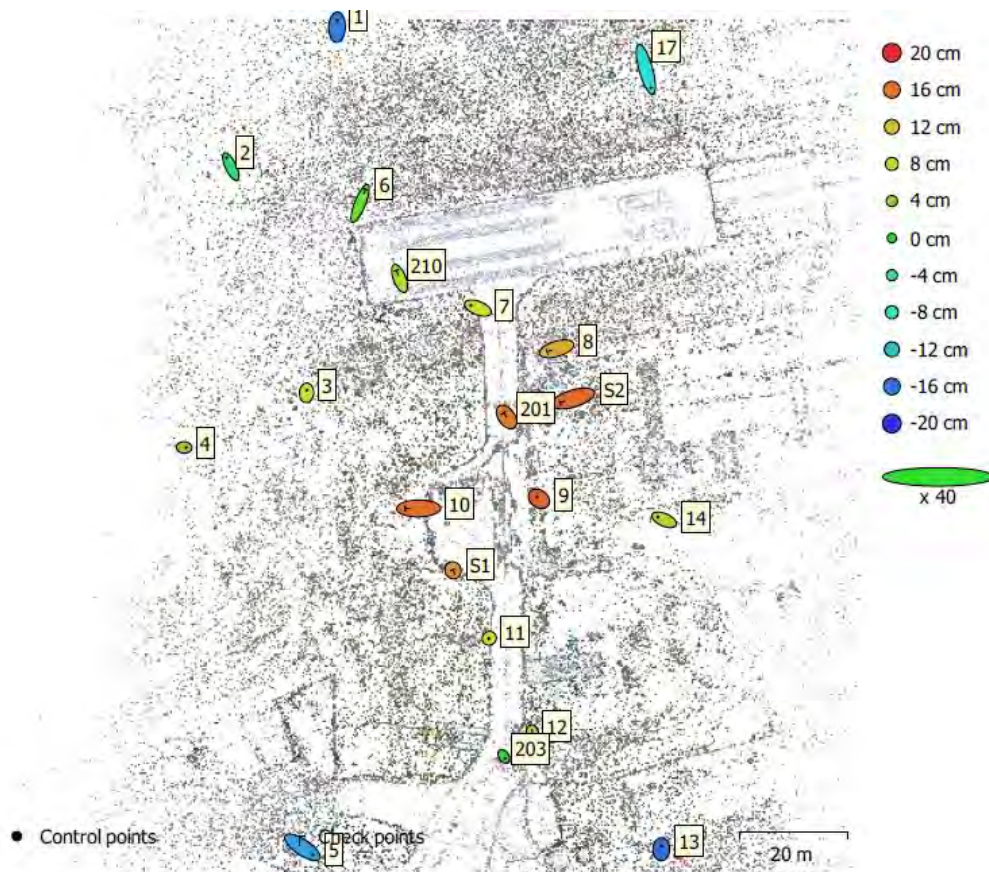


Figure 16 - GCP locations and error estimates.

Z error is represented by ellipse color. X, Y errors are represented by ellipse shape.
Estimated GCP / CHK locations are marked with a dot / crossing, respectively

Table C1-A: RMSE Control Points

GCP (#)	X (cm)	Y (cm)	Z (cm)	XY (cm)	Total (cm)	Image (pix)
12	4.3	6.2	11.0	7.6	13.4	0.4

Table C1-B: RMSE Check Points

CHK (#)	X (cm)	Y (cm)	Z (cm)	XY (cm)	Total (cm)	Image (pix)
8	7.3	5.7	12.5	9.3	15.6	0.5

Label	X error (cm)	Y error (cm)	Z error (cm)	Total (cm)	Image (pix)
1	0.186813	6.43172	-15.6102	16.8843	0.255 (5)
2	-3.8209	8.09554	-3.51426	9.61702	0.191 (5)
3	0.125455	2.53251	10.5634	10.8634	0.376 (8)
4	1.97838	-0.117346	4.60831	5.0164	0.248 (3)
5	9.96447	-6.69126	-13.5242	18.0823	0.510 (7)
7	-6.38632	2.46444	9.20305	11.4697	0.374 (7)
9	-2.09045	1.51879	17.3058	17.4976	0.488 (7)
11	-0.249652	-0.173478	9.604	9.60881	0.323 (8)
13	0.0838568	2.79395	-16.2456	16.4843	0.408 (8)
14	-5.82952	2.53222	7.05233	9.49372	0.276 (8)
17	4.72126	-16.9433	-9.24693	19.8714	0.586 (8)
203	1.43049	-2.04683	-1.17382	2.75929	0.362 (6)
Total	4.29534	6.27162	10.9875	13.3607	0.397

Table 5. Control points.
X - Easting, Y - Northing, Z - Altitude.

Label	X error (cm)	Y error (cm)	Z error (cm)	Total (cm)	Image (pix)
6	5.13379	12.8641	3.16022	14.2066	0.257 (5)
8	-9.02392	-2.6306	12.9512	16.0026	0.511 (9)
10	-12.5909	-0.169262	16.3422	20.6307	0.476 (8)
12	0.218283	-1.56068	6.0862	6.28691	0.332 (7)
201	-2.64551	3.78339	15.4418	16.1171	0.424 (5)
210	-2.87147	7.44737	6.72094	10.4345	0.534 (8)
S1	-0.276903	0.598342	14.3966	14.4117	0.743 (5)
S2	-12.083	-3.68679	16.6676	20.9141	0.655 (5)
Total	7.31169	5.68547	12.5026	15.5596	0.507

Table 6. Check points.
X - Easting, Y - Northing, Z - Altitude.

Configuration 2: Phantom, 80m, taxiway

UAV	Nominal Altitude of Images	Area	Images	Ground Coordinates	GCP 3D Accuracy
Phantom 2V+ Vision FC200	80m	Taxiway	110	Surveying	2.5cm

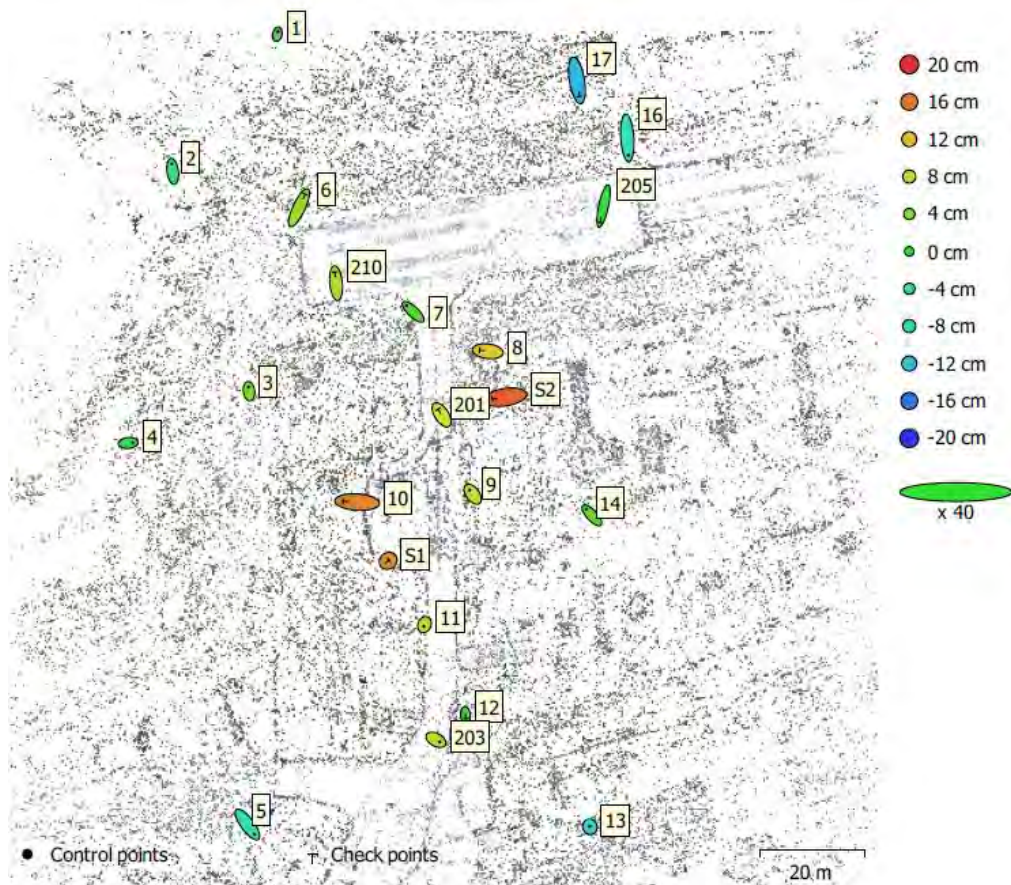


Figure 17 - GCP locations and error estimates.

Z error is represented by ellipse color. X, Y errors are represented by ellipse shape.
Estimated GCP / CHK locations are marked with a dot / crossing, respectively

Table C2-A: RMSE Control Points

GCP (#)	X (cm)	Y (cm)	Z (cm)	XY (cm)	Total (cm)	Image (pix)
12	3.6	6.6	6.3	7.5	9.8	0.4

Table C2-B: RMSE Check Points

CHK (#)	X (cm)	Y (cm)	Z (cm)	XY (cm)	Total (cm)	Image (pix)
10	6.8	9.0	10.9	11.3	15.7	0.5

Label	X error (cm)	Y error (cm)	Z error (cm)	Total (cm)	Image (pix)
1	0.572645	2.39281	0.307547	2.47953	0.247 (4)
2	-0.915526	7.07795	-4.29535	8.3298	0.328 (5)
3	-0.462818	3.84928	4.2595	5.75974	0.221 (4)
4	4.40489	0.424197	-3.08717	5.39571	0.194 (4)
5	6.89818	-9.32787	-7.77055	13.9634	0.271 (5)
7	-6.24893	5.85716	2.22038	8.84791	0.441 (4)
9	-2.79277	3.81376	8.07942	9.36062	0.253 (5)
11	-0.646455	-1.62019	7.91697	8.10687	0.401 (7)
13	-0.189775	0.588148	-10.642	10.66	0.810 (8)
14	-5.31199	5.7712	2.29027	8.17125	0.285 (6)
16	1.06421	-16.7108	-7.93508	18.5297	0.362 (5)
203	3.67018	-2.0059	7.72754	8.78685	0.612 (6)
Total	3.63422	6.62214	6.32893	9.85473	0.443

Table 5. Control points.
X - Easting, Y - Northing, Z - Altitude.

Label	X error (cm)	Y error (cm)	Z error (cm)	Total (cm)	Image (pix)
6	6.05039	12.8785	5.98559	15.4366	0.490 (7)
8	-7.81784	0.980232	11.2192	13.7095	0.353 (4)
10	-13.5836	0.823795	15.2763	20.4587	0.304 (5)
12	0.256344	-3.40117	0.889042	3.52478	0.314 (7)
17	2.51412	-15.3543	-12.1334	19.7306	0.429 (4)
201	-3.53455	5.4134	9.80959	11.7484	0.363 (5)
205	-3.45043	-15.7931	-0.785878	16.1847	0.714 (5)
210	-1.03044	10.6877	6.95225	12.7915	0.670 (7)
S1	0.896389	0.722537	14.5396	14.5851	0.334 (4)
S2	-12.3548	-1.93915	17.2737	21.3257	0.409 (4)
Total	6.83763	9.0114	10.9455	15.7405	0.471

Table 6. Check points.
X - Easting, Y - Northing, Z - Altitude.

Configuration 3: Phantom, 80m, taxiway

UAV	Nominal Altitude of Images	Area	Images	Ground Coordinates	GCP 3D Accuracy
Phantom 2V+ Vision FC200	80m	Taxiway	73	GNSS	2.5cm

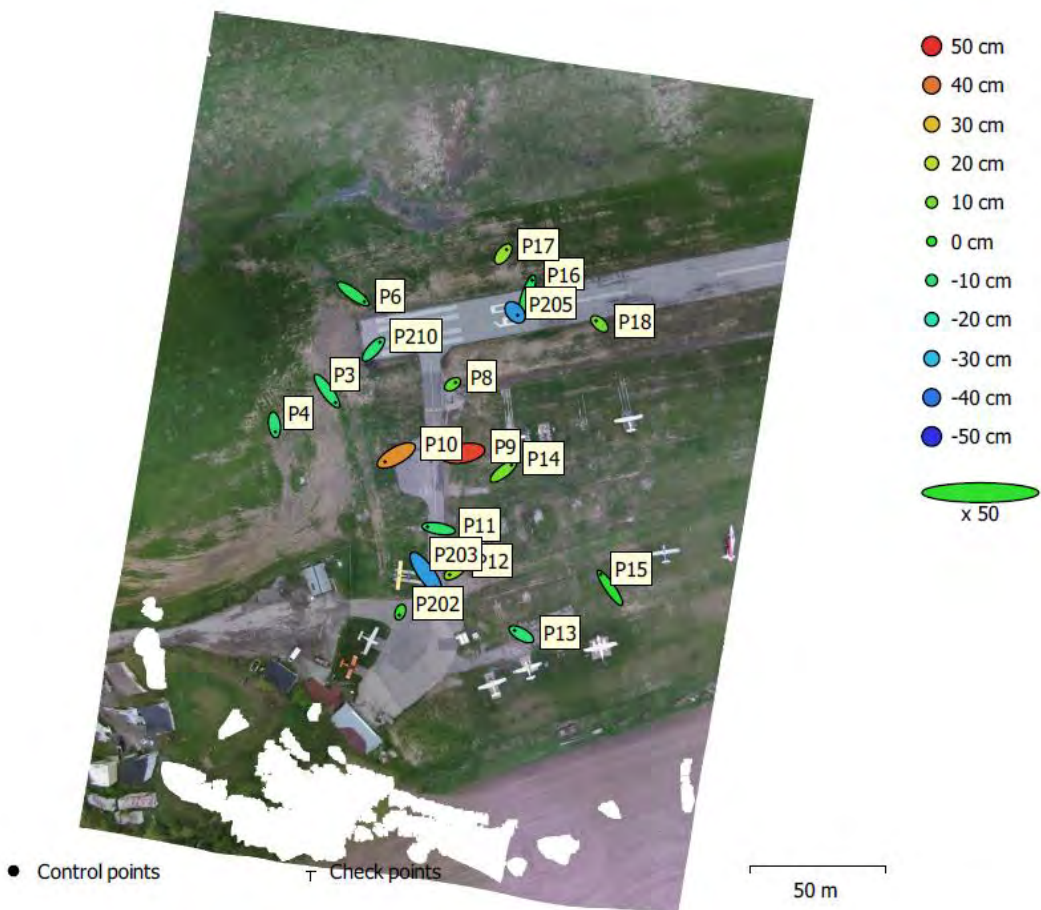


Figure 18 - GCP locations and error estimates

Z error is represented by ellipse color. X, Y errors are represented by ellipse shape.
Estimated GCP / CHK locations are marked with a dot / crossing, respectively

Table C3-A: RMSE Control Points

GCP (#)	X (cm)	Y (cm)	Z (cm)	XY (cm)	Total (cm)	Image (pix)
18	11.1	11.2	20.0	15.8	25.5	0.8

Table C3-B: RMSE Check Points

CHK (#)	X (cm)	Y (cm)	Z (cm)	XY (cm)	Total (cm)	Image (pix)
0						

Label	X error (cm)	Y error (cm)	Z error (cm)	Total (cm)	Image (pix)
P3	12.4364	-17.1037	-9.88025	23.3414	0.515 (6)
P4	1.31121	-10.3585	-10.4718	14.7878	0.902 (4)
P6	16.2076	-11.4519	-6.81471	20.9826	0.910 (11)
P11	-16.1863	2.78545	-8.32712	18.4145	1.064 (8)
P12	-8.40273	-5.97932	13.9689	17.3634	0.483 (8)
P13	-10.2107	5.75279	-10.4956	15.7324	0.845 (9)
P15	-13.5895	19.7819	-0.42379	24.0037	0.661 (7)
P16	7.25019	21.4844	-5.77708	23.3991	0.570 (18)
P17	4.9428	6.53182	14.5918	16.7337	0.535 (12)
P18	-5.12826	4.52689	9.41332	11.6363	0.511 (9)
P202	-1.63679	-4.29105	2.0397	5.0252	0.943 (9)
P203	14.3606	-20.1886	-34.8146	42.7301	0.669 (10)
P205	3.81562	-4.32826	-35.3045	35.7729	0.821 (17)
P210	9.46571	10.4508	-9.69204	17.1101	1.482 (18)
P8	4.36023	2.83106	6.3443	8.20224	0.351 (4)
P9	-18.1631	-3.32947	47.3002	50.7768	0.570 (8)
P10	-16.6132	-9.21914	36.1494	40.8384	0.583 (8)
P14	11.9803	9.18782	9.79673	17.9978	0.342 (4)
Total	11.119	11.2203	20.0004	25.4862	0.825

Table 4. Control points.
X - Easting, Y - Northing, Z - Altitude.

Configuration 4: Phantom, 40m+80m, taxiway

UAV	Nominal Altitude of Images	Area	Images	Ground Coordinates	GCP 3D Accuracy
Phantom 2V+ Vision FC200	40m and 80m	Taxiway	213	Surveying	2cm

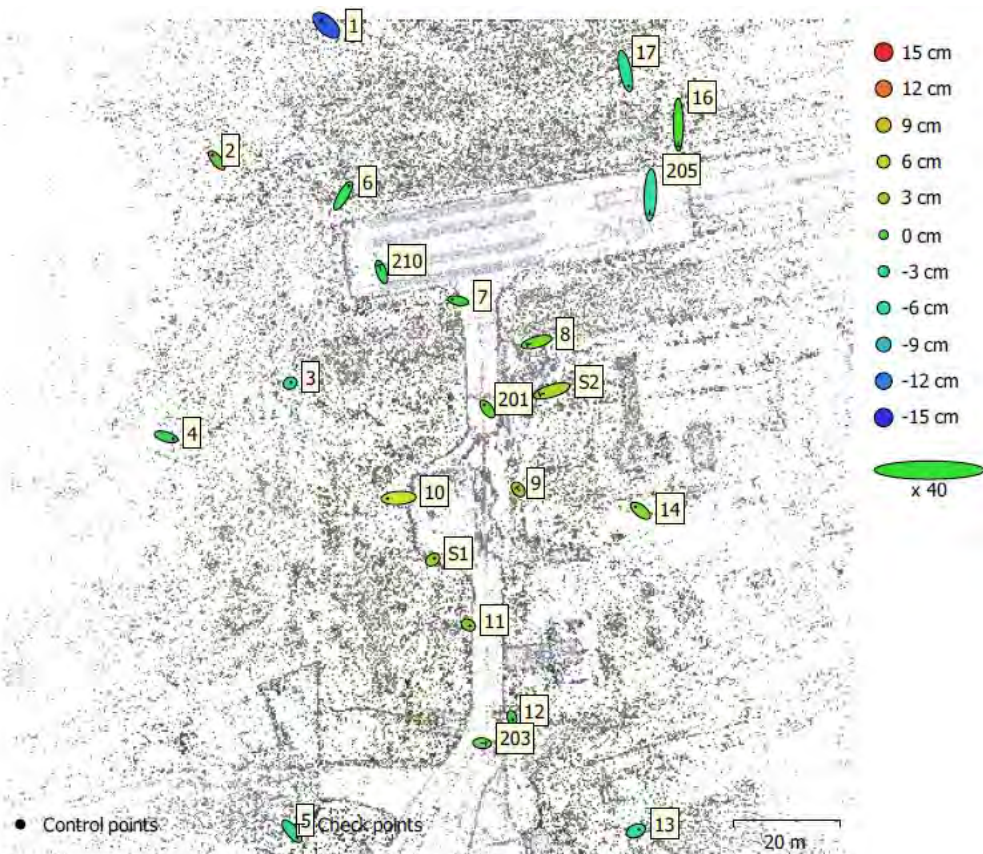


Figure 20 - GCP locations and error estimates.

Z error is represented by ellipse color. X, Y errors are represented by ellipse shape.
Estimated GCP / CHK locations are marked with a dot / crossing, respectively

Table C4-A: RMSE Control Points

GCP (#)	X (cm)	Y (cm)	Z (cm)	XY (cm)	Total (cm)	Image (pix)
14	4.7	5.3	3.5	7.0	7.8	0.6

Table C4-B: RMSE Check Points

CHK (#)	X (cm)	Y (cm)	Z (cm)	XY (cm)	Total (cm)	Image (pix)
8	5.8	10.3	5.7	11.8	13.1	0.7

Note: Z-RMSE is “smaller” than expected compared to the planimetric ones

Label	X error (cm)	Y error (cm)	Z error (cm)	Total (cm)	Image (pix)
S1	1.55677	1.17052	3.58401	4.07906	0.511 (14)
2	-4.07239	4.95066	1.22279	6.526	0.114 (3)
3	0.942002	0.492252	-4.36049	4.48816	0.256 (6)
4	6.51074	-1.93981	-1.0931	6.88095	0.258 (2)
5	4.89492	-5.96328	-3.42736	8.44202	0.375 (6)
6	5.37756	9.16088	-1.58036	10.7395	0.306 (11)
7	-5.46933	1.0725	0.00693366	5.5735	0.493 (8)
10	-10.3185	-0.635825	6.6166	12.2742	0.215 (5)
11	1.51978	-0.822636	3.24868	3.67972	0.349 (7)
12	0.574818	-2.20468	0.437976	2.3201	0.942 (12)
13	3.13241	1.2466	-5.76847	6.68142	0.724 (8)
14	-4.58443	3.64101	3.3495	6.74486	0.267 (5)
17	3.11877	-14.1531	-4.26121	15.1061	1.087 (5)
201	-2.99328	3.93783	1.74955	5.24663	0.581 (8)
Total	4.65759	5.25823	3.47472	7.83683	0.574

Table 5. Control points.
X - Easting, Y - Northing, Z - Altitude.

Label	X error (cm)	Y error (cm)	Z error (cm)	Total (cm)	Image (pix)
S2	-11.4216	-3.54338	5.22096	13.0486	0.500 (12)
1	-5.36604	4.96375	-13.2583	15.1398	0.235 (4)
8	-9.2171	-2.61519	3.05536	10.0563	0.931 (8)
9	-1.466	1.8848	3.92194	4.59164	0.335 (6)
16	0.0799162	-20.2852	1.16932	20.3191	1.166 (5)
203	3.75111	-0.274976	2.15196	4.33329	0.857 (12)
210	-2.3002	6.41904	-1.08607	6.90468	0.544 (10)
205	-0.709807	-18.7022	-5.13746	19.408	0.714 (9)
Total	5.7687	10.3085	5.71542	13.1229	0.718

Table 6. Check points.
X - Easting, Y - Northing, Z - Altitude.

Configuration 5: Phantom, 40m, runway

UAV	Nominal Altitude of Images	Area	Images	Ground Coordinates	GCP 3D Accuracy
Phantom 2V+ Vision FC200	40m	Runway	337	Surveying	2cm

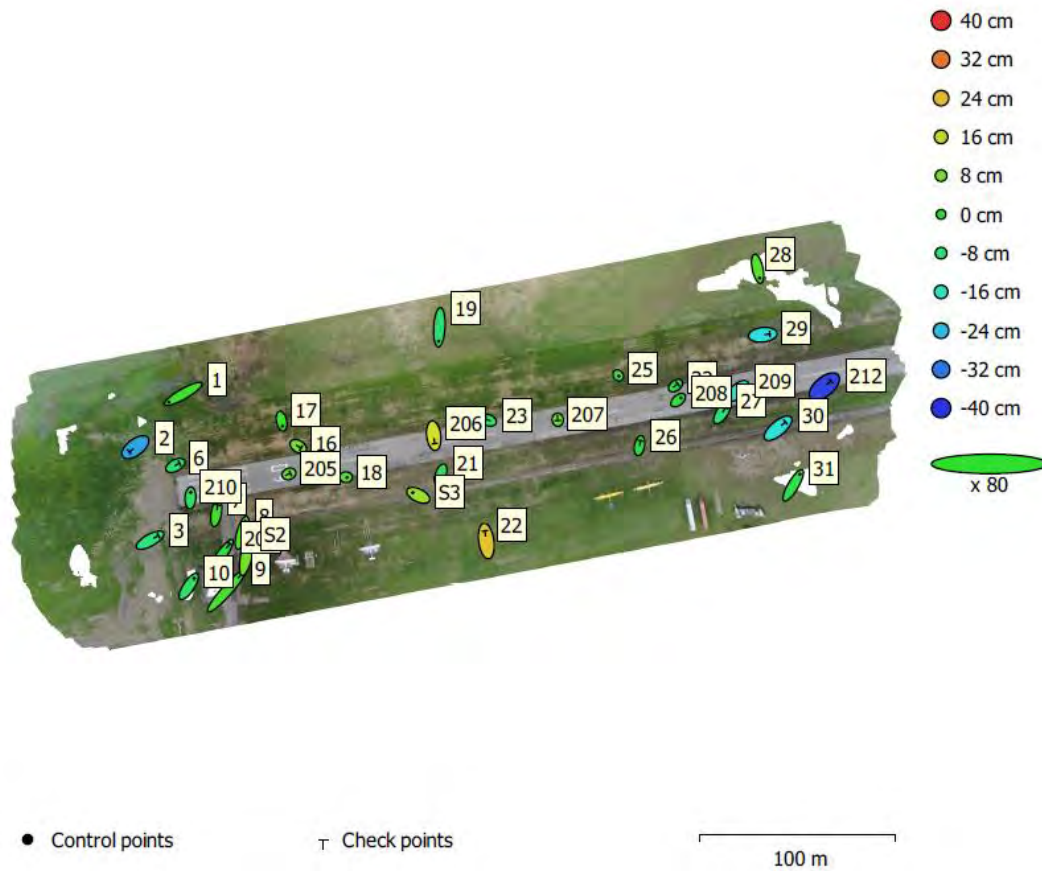


Figure 21 - GCP locations and error estimates

Z error is represented by ellipse color. X, Y errors are represented by ellipse shape.
Estimated GCP / CHK locations are marked with a dot / crossing, respectively

Table C5-A: RMSE Control Points

GCP (#)	X (cm)	Y (cm)	Z (cm)	XY (cm)	Total (cm)	Image (pix)
13	6.5	9.8	5.3	11.7	12.9	2.2

Note: Z-RMSE is “smaller” than expected compared to the planimetric ones

Table C5-B: RMSE Check Points

CHK (#)	X (cm)	Y (cm)	Z (cm)	XY (cm)	Total (cm)	Image (pix)
20	7.5	9.8	15.1	12.4	19.5	2.2

Label	X error (cm)	Y error (cm)	Z error (cm)	Total (cm)	Image (pix)
1	-18.385	-10.4904	2.16532	21.2778	0.680 (6)
8	4.06631	14.4506	4.03865	15.5456	0.484 (9)
10	6.87817	10.4346	-5.64274	13.7124	0.010 (2)
17	1.29553	-6.28588	2.03753	6.73367	0.471 (3)
18	1.363	-0.0979539	4.51213	4.71452	0.428 (3)
19	-1.01795	-17.7691	-7.14012	19.177	0.139 (3)
21	-2.44251	-7.08068	-4.46577	8.72038	3.236 (6)
25	0.663986	-0.927149	1.19375	1.65091	0.450 (10)
28	2.53744	-11.7905	4.50186	12.8732	1.153 (6)
31	8.45991	14.2345	-2.76974	16.7887	0.282 (4)
208	3.46021	2.93051	-1.74117	4.85722	0.235 (6)
210	0.375573	7.09885	-4.81817	8.58776	1.152 (11)
S3	-6.93302	3.39444	12.5828	14.7619	5.592 (9)
Total	6.51048	9.79068	5.27848	12.8882	2.194

Table 4. Control points.
X - Easting, Y - Northing, Z - Altitude.

Label	X error (cm)	Y error (cm)	Z error (cm)	Total (cm)	Image (pix)
2	-7.81279	-5.91387	-26.7953	28.5307	1.113 (5)
3	10.7033	5.91104	-8.84905	15.0933	1.270 (8)
6	5.31065	2.79307	-7.41276	9.53694	1.428 (4)
7	1.8547	10.72	2.37995	11.1365	0.516 (8)
9	19.4407	21.6556	2.76132	29.2324	0.327 (3)
16	3.42128	-2.11121	8.65795	9.54581	0.325 (4)
22	-1.81423	13.043	22.8767	26.3961	0.061 (2)
23	-3.66477	1.29759	-5.99449	7.1448	6.582 (5)
26	1.27494	6.39521	-2.03707	6.83183	0.175 (3)
27	4.76761	7.05988	-7.72175	11.4977	0.261 (5)
29	8.99177	0.954667	-20.1003	22.0405	1.247 (7)
30	9.65348	8.04015	-19.3662	23.0843	0.528 (7)
32	2.79693	2.1644	-2.94447	4.60188	0.325 (7)

Label	X error (cm)	Y error (cm)	Z error (cm)	Total (cm)	Image (pix)
201	13.5719	19.2635	-1.61724	23.6198	0.577 (5)
205	1.73354	0.707233	6.74805	7.00296	0.200 (5)
206	1.21546	-10.0033	18.3973	20.9763	5.901 (7)
207	0.0825574	-1.14274	6.74757	6.84414	0.233 (4)
209	6.41435	5.72577	-16.3722	18.4926	0.598 (7)
212	8.42899	7.08206	-37.7386	39.3117	0.775 (8)
S2	4.30601	19.1627	8.36551	21.3479	0.271 (5)
Total	7.54735	9.80292	15.0742	19.5011	2.172

Table 5. Check points.

X - Easting, Y - Northing, Z - Altitude.

Configuration 6: Phantom, 40m, runway

UAV	Nominal Altitude of Images	Area	Images	Ground Coordinates	GCP 3D Accuracy
Phantom 2V+ Vision FC200	40m	Runway	342	GNSS	2.5cm

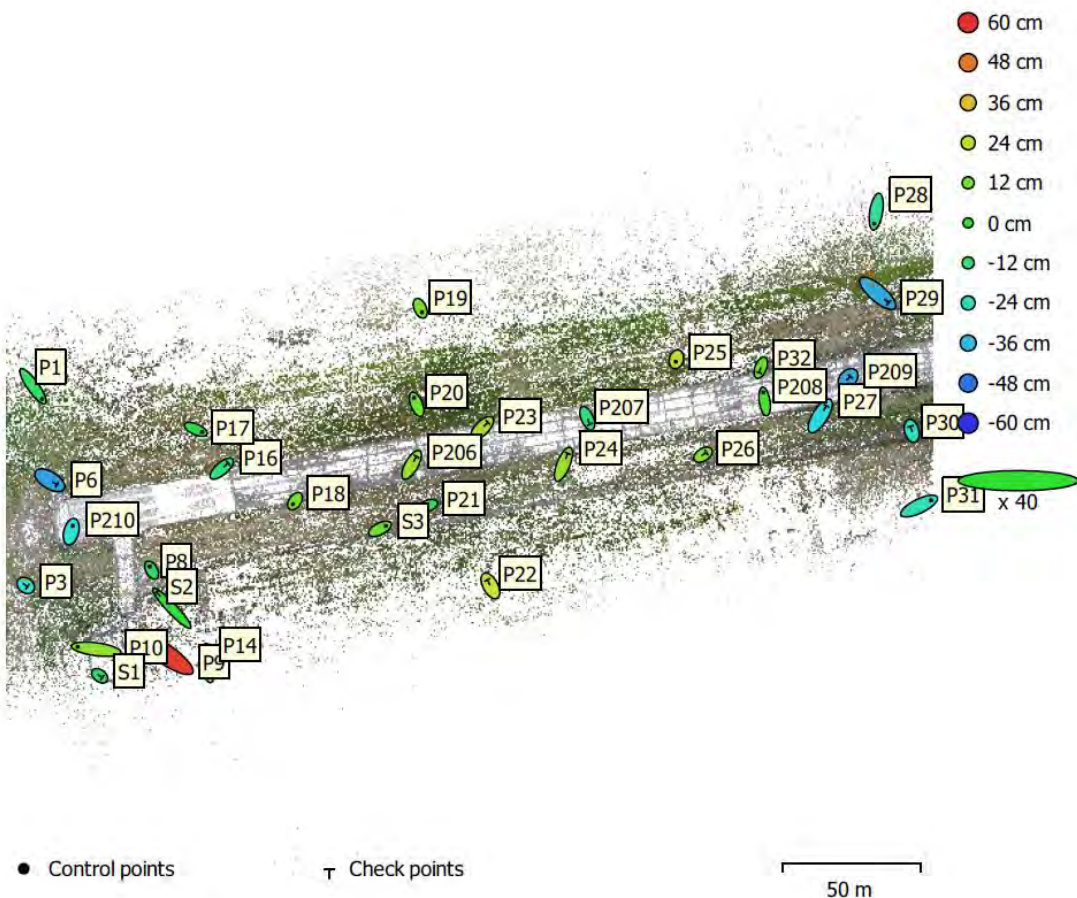


Figure 22 - GCP locations and error estimates

Z error is represented by ellipse color. X, Y errors are represented by ellipse shape.
Estimated GCP / CHK locations are marked with a dot / crossing, respectively

Table C6-A: RMSE Control Points

GCP (#)	X (cm)	Y (cm)	Z (cm)	XY (cm)	Total (cm)	Image (pix)
14	12.7	11.6	15.4	17.2	23.1	0.8

Table C6-B: RMSE Check Points

CHK (#)	X (cm)	Y (cm)	Z (cm)	XY (cm)	Total (cm)	Image (pix)
18	13.6	14.8	27.4	20.1	34.0	0.9

Label	X error (cm)	Y error (cm)	Z error (cm)	Total (cm)	Image (pix)
P1	16.386	-23.1712	-8.72504	29.6906	1.028 (8)
P8	-3.62217	6.5275	-8.46947	11.2898	0.230 (5)
P10	-33.4841	4.37257	16.9841	37.799	0.277 (4)
P17	11.4504	-5.00591	-4.06761	13.1422	0.486 (4)
P18	-3.69043	-5.43397	12.607	14.2156	0.426 (7)
P19	3.25265	-7.35007	12.5105	14.87	0.651 (6)
P20	-4.68266	11.7527	11.0235	16.7801	0.761 (8)
P21	-9.06908	-3.66471	-6.95446	12.0018	1.091 (7)
P25	-1.21359	-4.44253	24.2294	24.6632	0.405 (7)
P28	-3.56302	-21.8888	-16.7896	27.8156	1.880 (6)
P31	21.6353	10.4961	-23.8037	33.836	0.025 (2)
P208	-2.44858	16.3957	4.41795	17.1561	0.541 (8)
P210	2.79464	10.8376	-28.7317	30.8346	0.480 (4)
S3	10.7487	5.38556	10.03	15.657	0.732 (7)
Total	12.7444	11.5977	15.398	23.109	0.822

Table 4. Control points.
X - Easting, Y - Northing, Z - Altitude.

Label	X error (cm)	Y error (cm)	Z error (cm)	Total (cm)	Image (pix)
P3	3.05614	-2.24063	-28.0924	28.3468	0.536 (4)
P6	12.9755	-7.86451	-40.7384	43.4722	1.308 (8)
P9	-36.0259	24.6666	57.7652	72.4094	0.017 (2)
P14	-2.84591	23.3007	21.3075	31.7022	0.265 (4)
P16	11.5686	9.97443	-12.8385	19.9537	0.375 (6)
P22	-5.89831	10.8315	28.0241	30.618	2.256 (4)
P23	10.4539	10.6776	21.1994	25.9367	0.283 (7)
P24	7.95675	19.723	17.301	27.4159	0.476 (10)
P26	6.11292	3.84391	14.2034	15.9336	0.388 (7)
P27	11.3707	18.2411	-30.8833	37.6272	0.560 (6)
P29	19.8462	-17.1038	-39.1188	47.0818	1.707 (8)
P30	-2.16727	8.11905	-25.2896	26.6492	0.640 (6)

Label	X error (cm)	Y error (cm)	Z error (cm)	Total (cm)	Image (pix)
P32	-3.52046	-8.95704	9.85606	13.7755	0.421 (7)
P206	8.69126	15.2777	17.6589	24.9155	0.545 (6)
P207	4.72102	-10.9482	-11.9798	16.9017	0.534 (5)
P209	4.02749	4.51614	-39.3596	39.822	0.944 (5)
S1	4.45188	-3.36047	-11.5667	12.8413	0.010 (2)
S2	-27.8288	29.102	-0.596105	40.2707	0.381 (3)
Total	13.5622	14.8252	27.3858	33.9662	0.879

Table 5. Check points.
X - Easting, Y - Northing, Z - Altitude.

Configuration 7: M100, 40m, taxiway

UAV	Nominal Altitude of Images	Area	Images	Ground Coordinates	GCP 3D Accuracy
M100 HERO5 Black	40m	Taxiway	485	Surveying	2.5cm

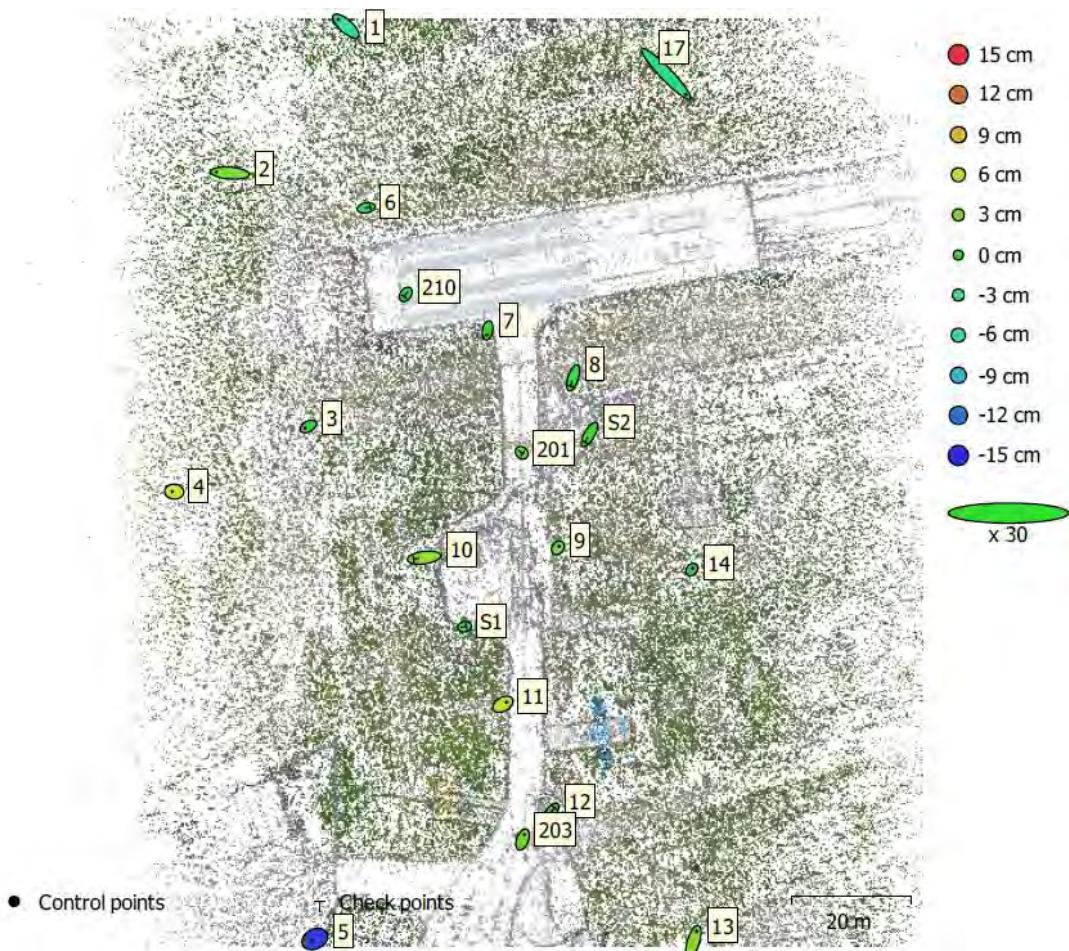


Figure 23- GCP locations and error estimates

Z error is represented by ellipse color. X, Y errors are represented by ellipse shape.
Estimated GCP / CHK locations are marked with a dot / crossing, respectively

Table C7-A: RMSE Control Points

GCP (#)	X (cm)	Y (cm)	Z (cm)	XY (cm)	Total (cm)	Image (pix)
12	8.4	8.1	5.4	11.7	12.9	0.6

Table C7-B: RMSE Check Points

CHK (#)	X (cm)	Y (cm)	Z (cm)	XY (cm)	Total (cm)	Image (pix)
8	5.2	4.9	1.6	7.1	7.3	0.6

Note: Z-RMSE is “smaller” than expected compared to the planimetric ones

Label	X error (cm)	Y error (cm)	Z error (cm)	Total (cm)	Image (pix)
1	-8.38004	7.43047	-4.54489	12.0869	0.463 (5)
2	-15.1295	1.15565	2.81501	15.4325	0.331 (7)
3	-3.61769	-1.99285	-0.629752	4.178	0.223 (5)
4	-2.3126	0.172209	7.40262	7.75735	0.294 (5)
5	-3.64018	-1.83911	-14.4266	14.992	0.870 (5)
7	-0.872913	-4.98779	0.404729	5.07974	0.418 (6)
9	1.26674	1.55018	2.06491	2.87603	1.029 (5)
11	3.98945	2.27625	5.67902	7.304	0.510 (5)
13	3.63556	12.0115	3.16324	12.9422	0.216 (5)
14	1.11512	1.36658	-0.719963	1.90509	0.329 (5)
17	22.0171	-22.801	-3.46564	31.885	0.551 (5)
203	1.99641	5.45022	2.57514	6.34996	0.727 (5)
Total	8.42762	8.1247	5.46006	12.917	0.547

Table 5. Control points.
X - Easting, Y - Northing, Z - Altitude.

Label	X error (cm)	Y error (cm)	Z error (cm)	Total (cm)	Image (pix)
6	4.5292	0.802963	0.0627427	4.60026	0.742 (5)
8	-2.94404	-8.95131	-0.60958	9.44271	0.610 (8)
10	-11.6855	-1.57023	3.70248	12.3582	0.483 (5)
12	4.13395	5.37619	0.442214	6.79622	0.792 (5)
201	1.01957	-0.819085	2.09592	2.47048	0.708 (7)
210	-1.62743	-2.30075	-1.26149	3.08761	0.600 (5)
S1	2.05219	0.365701	-0.404596	2.12342	0.394 (5)
S2	-4.93594	-8.44469	0.219425	9.78389	0.370 (5)
Total	5.18512	4.86763	1.59982	7.28964	0.611

Table 6. Check points.
X - Easting, Y - Northing, Z - Altitude.

Configuration 8: M100, 80m, taxiway

UAV	Nominal Altitude of Images	Area	Images	Ground Coordinates	GCP 3D Accuracy
M100 HERO5 Black	80m	Taxiway	281	Surveying	2cm

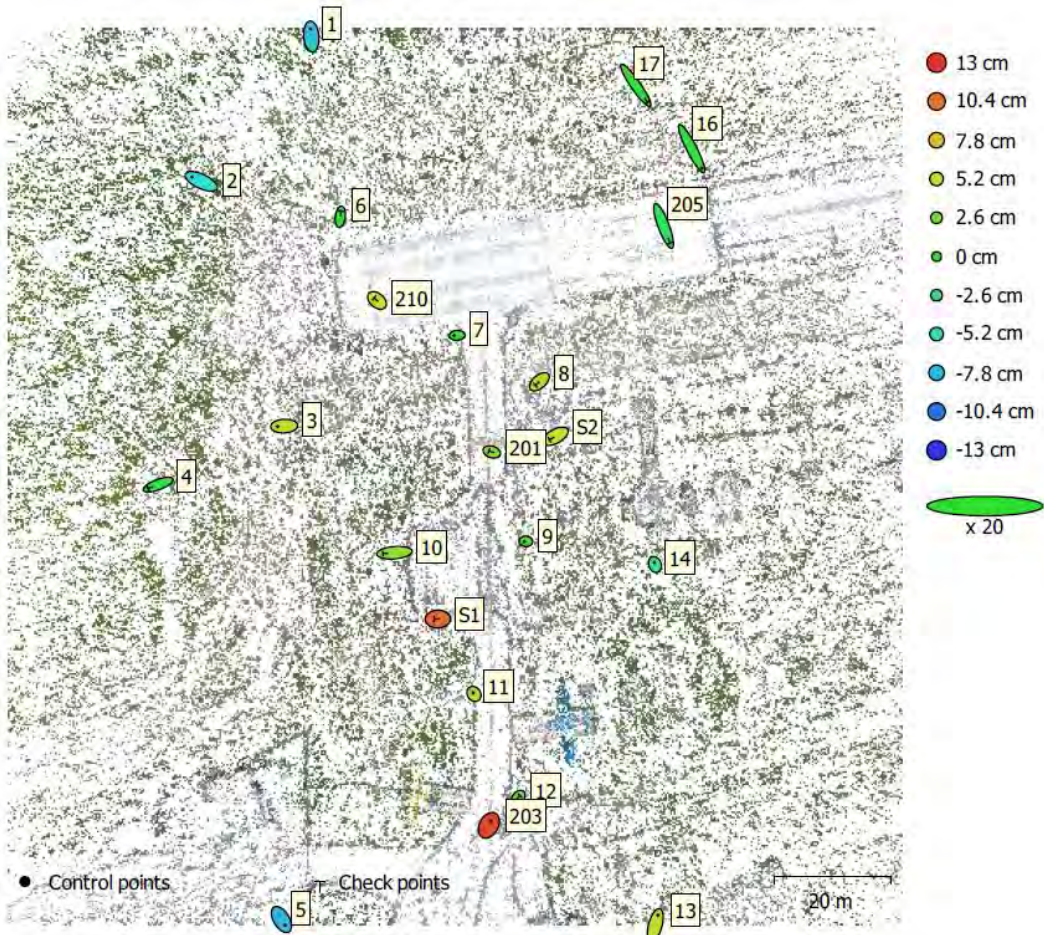


Figure 24 - GCP locations and error estimates

Z error is represented by ellipse color. X,Y errors are represented by ellipse shape.
Estimated GCP / CHK locations are marked with a dot / crossing, respectively

Table C8-A: RMSE Control Points

GCP (#)	X (cm)	Y (cm)	Z (cm)	XY (cm)	Total (cm)	Image (pix)
11	8.6	12.9	6.0	15.5	16.6	0.7

Table C8-B: RMSE Check Points

CHK (#)	X (cm)	Y (cm)	Z (cm)	XY (cm)	Total (cm)	Image (pix)
11	11.7	13.4	4.6	17.8	18.4	0.8

Note: Z-RMSE is “smaller” than expected compared to the planimetric ones

Label	X error (cm)	Y error (cm)	Z error (cm)	Total (cm)	Image (pix)
1	-1.1366	13.4738	-7.54489	15.4842	0.989 (6)
2	-16.3376	7.48903	-6.16358	18.9998	0.726 (7)
3	-11.5627	-0.551411	5.30636	12.7341	0.619 (7)
5	5.8777	-9.71123	-8.08856	13.9384	0.747 (9)
7	-5.24949	-0.348485	0.23803	5.26643	0.690 (9)
9	-2.85746	0.13251	0.858154	2.98648	0.656 (10)
11	-1.3272	1.90429	4.68893	5.232	0.659 (9)
13	4.73789	17.2825	5.13869	18.6424	0.782 (7)
14	-1.30397	3.39935	-3.60808	5.12583	0.922 (10)
16	17.3571	-33.6856	-0.591588	37.899	0.753 (11)
203	3.6411	6.60848	12.124	14.2801	0.390 (5)
Total	8.59499	12.8793	6.01545	16.6113	0.742

Table 5. Control points.
X - Easting, Y - Northing, Z - Altitude.

Label	X error (cm)	Y error (cm)	Z error (cm)	Total (cm)	Image (pix)
4	-17.2271	-6.40341	-0.853002	18.3985	0.844 (5)
6	1.21879	9.94551	-0.374283	10.0269	0.782 (6)
8	-6.88836	-6.03696	4.43178	10.1752	0.564 (8)
10	-20.0478	-1.65833	3.52628	20.423	0.662 (10)
12	2.91383	3.22167	2.24753	4.89091	0.771 (9)
17	20.3166	-29.3308	-0.0659433	35.68	0.587 (5)
201	-5.1249	1.65419	2.65487	6.0041	0.915 (10)
205	11.0902	-29.636	-1.79145	31.6938	1.059 (8)
210	-5.0429	4.29063	5.8355	8.82572	1.146 (9)
S1	-6.4632	-0.208372	10.8925	12.6674	0.812 (6)
S2	-10.5812	-6.07789	5.5982	13.4254	0.634 (7)
Total	11.667	13.4374	4.5954	18.3793	0.830

Table 6. Check points.
X - Easting, Y - Northing, Z - Altitude.

ANALYSIS OF THE PHOTOGRAMMETRIC NETWORK DESIGN CONFIGURATIONS

The selected configurations were selected to investigate the impact of various flight design parameters, accuracy of the GCP, and the use of different camera sensors. At the time of the field work and the UAV flights the expected equipment, that is higher end platforms and navigation and cameras had not arrived yet at our lab. Therefore, we conducted the experiments with the available low-end UAV platforms, cameras and navigation systems.

The UAV images were captured with two cameras onboard two different UAV platform. The Vision FC200 ($f=5\text{mm}$) camera onboard the Phantom 2 Vision+ and the GoPro HERO5 Black ($f=3\text{mm}$) onboard the M100. The Vision FC200 has an angular field of view of 75.38° , therefore is at the border line between narrow and wide angle lens cameras (N/W), while the GoPro HERO5 has an angular field of view of 103.78° which is at the border line between wide and super-wide lens cameras (W/SW). Therefore, the GoPro HERO5 camera has a wider angular field of view than the Vision FC200. Both cameras operate with rolling shutter so the image quality may be affected by the time of exposure, although we did not notice it.

Photogrammetric accuracy in relation to different flying altitudes – Phantom UAV

As the accuracy is a direct function of the image scale, the UAV images were taken from two different flight altitudes, 40m and 80m, respectively. The results showed that flying at lower altitude resulted in more significant improvement in the elevation component Z rather than the planimetry component of X and Y.

Photogrammetric accuracy in relation to GCP and EO accuracy – Phantom UAV

The coordinates of GCPs were determined with both ground land surveying and GNSS methods. Due to inexperience the GNSS derived coordinates were less accurate than those determined from the land surveying methods and thus the configurations where the coordinates of the GCPs and CHK were determined by ground surveying methods resulted in much better results (smaller X, Y, Z RMSE). Therefore, the accuracy of the GCPs and/or the accuracy of the EO camera parameters of the UAV images directly affects the accuracy of the 3D coordinates derived through the photogrammetric processing of the UAV images. Other options would be a) to conduct the bundle adjustment without GCP, that is perform a SfM solution and then using some accurate GCP to perform a 3D similarity transformation to obtain the georeferenced 3D object points from the image/model space; and b) using RTK for accurately determining the EO parameters of the camera sensor.

Photogrammetric accuracy in relation to combining UAV images from different altitudes

As the Markham Airport is a relative very flat area with no significant relief variations, one of the conditions -depth variations in the object space- is not met, therefore impacting the bundle adjustment with self-calibration. Using images from different flying heights as well high image overlap and GCPs assist in overcoming this problem. Comparing the results from the combined 40m+80m images with those from the 40m and 80m, respectively we observed: a) the X, Y RMSE at the GCPs are similar while there is some improvement in the Z RMSE; and b). the X, Y RMSE at the check points are also similar, however there is

a significant improvement of about 50% in the Z RMSE.

Photogrammetric accuracy in relation to the two cameras used – Phantom with N/W camera lensa and M100 with W/SW camera lens

The flights of the two UAVs carrying two different cameras were also assessed. We observed that at the 40m flying height the N/W camera resulted a) for the GCP better X,Y RMSE while the W/SW camera gave much better Z RMSE, and b) for the CHK both cameras gave comparable X,Y RMSE but the wide/super-wide camera gave better Z RMSE. For the 80m flying altitude the N/W camera for the GCP gave better X, Y and similar to W/SW for the Z RMSE. For the CHK points the N/W gave better X, Y RMSE while the W/SW camera gave better Z RMSE.

The reason that the Z RMSE are smaller in the case of the W/SW GoPro HERO5 camera is the fact that the B/H ratio is larger than the one of the N/W camera flying from the same flying height H. This is why when higher accuracy is required for relative low relief terrain, cameras with super-wide angle lenses are used. For hilly terrain and urban areas with medium and high building cameras equipped with normal angle lenses should be used. Therefore, for low altitude UAV photogrammetric projects it is recommended that cameras with wide angle lenses should be used.

Photogrammetric vertical accuracies on the hard surfaces (pavement)

Considering the above analysis and inspecting the Z RMSE values at the CHK points we note that:

- the combination of 40m and 80m altitude images using the Phantom with the FC200, results in vertical errors in the range of 3cm for CHK points located on the pavement.
- flying from 40m altitude using M100 with the GoProHERO5 camera, results in vertical errors of about 2cm for CHK points located on the pavement.

PHOTOGRAMMETRIC MAPPING PRODUCTS

Figure 24 illustrates photogrammetric mapping products such as a dense DSM and a high resolution orthoimage mosaic with superimposed contours lines generated from the DSM.





Figure 25 - DSM and contour generation

UAV Bridge Mapping – HWY 401 / Oshawa Creek

The potential of UAV mapping and inspection of HWY assets such as bridges was also investigated as part of this project. One of the selected bridges was the HWY 401 Oshawa Creek Cast Concrete overpass Bridge (tunnel (covered) type concrete bridge with the 401 HWY running over it). The bridge is located at lat: $43^{\circ} 52' 50.48''$ N and lon: $78^{\circ} 51' 30.25''$ W, (Site #:22X-0175), Oshawa, ON (Fig. 26).

The UAV survey conducted on August 29, 2019. The M100 and Falcon-8+ UAVs were used in manual control as flying within the bridge was a GNSS-denied area. The caged/collision tolerant Elios UAV was also demonstrated for accessing and inspecting confined, inaccessible, and difficult to view spaces (Fig. 28).



Figure 26 – Location and views of the Oshawa bridge

PLANIMETRIC SURVEY NETWORK

Three points were surveyed using GNSS methods, (Appendix D), while a total of 44 points were surveyed using a total station. A traverse of 4 points was set for the total station survey TOPO1, RIVER1, TOPO2, and S1. Besides the ground targets, we have also used reflective tape survey targets for the areas that were accessible and landmarks (graffiti edges- cracks- cement plates connections) for the inaccessible areas.

To solve the network, a total of 24 observations were used – 8 directional angles, 8 zenith angles, and 8 slope distances. The system had 12 degrees of freedom, with a total of 16 unknowns (the XYZ of each of the 4 points). Being constrained, the coordinates of S1 and TOPO2 were held fixed during the adjustment process.

VERTICAL SURVEY NETWORK

For the ground elevation determination of the ground points, trigonometric levelling was performed. Similarly, first the orthometric heights of the defined traverse points were found and adjusted, then heights were propagated to remaining survey points.

Traverse points in the survey area consisted of TOPO1, TOPO2, RIVER1, and S1 (Fig. 26). As observation to each traverse point were made in both directions (ex. from TOPO2 to S1 and S1 to TOPO2), loops were treated in a double-run manner. The GNSS orthometric height at point TOPO1 was used as the fixed elevation and propagated through to the remaining traverse points. Each loop was adjusted based on a weighted contribution of distance to the total misclosure. That is, loop segments were adjusted based on the distance between points to the total distance of the loop. The calculated elevations for the control points through the double-run were then averaged.

The ground point network is shown in Figure 27, while the details of the computations and the coordinates of the ground points are given in Appendices B and D.

UAV AERIAL SURVEY

Two UAVs were also flown in the Oshawa Bridge site – the DJI M100 and Intel Falcon 8. The M100 UAV was equipped with a GoPro HERO 7 camera on the EVO SS gimbal camera and was flown multiple times. The Intel Falcon 8+ was equipped with Sony Alpha 7R camera.

A summary of the total number of images captured in each flight by the M100 is provided in the Table 6 below.

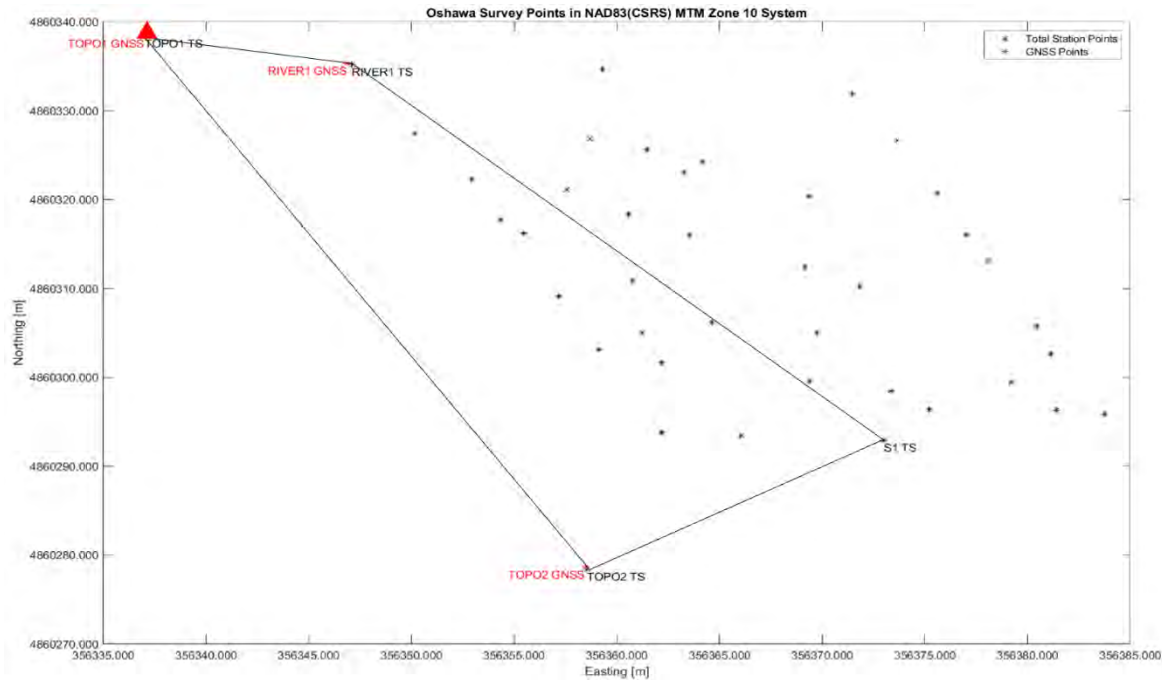


Figure 27 – Ground points and levelling loop of the Oshawa Survey site

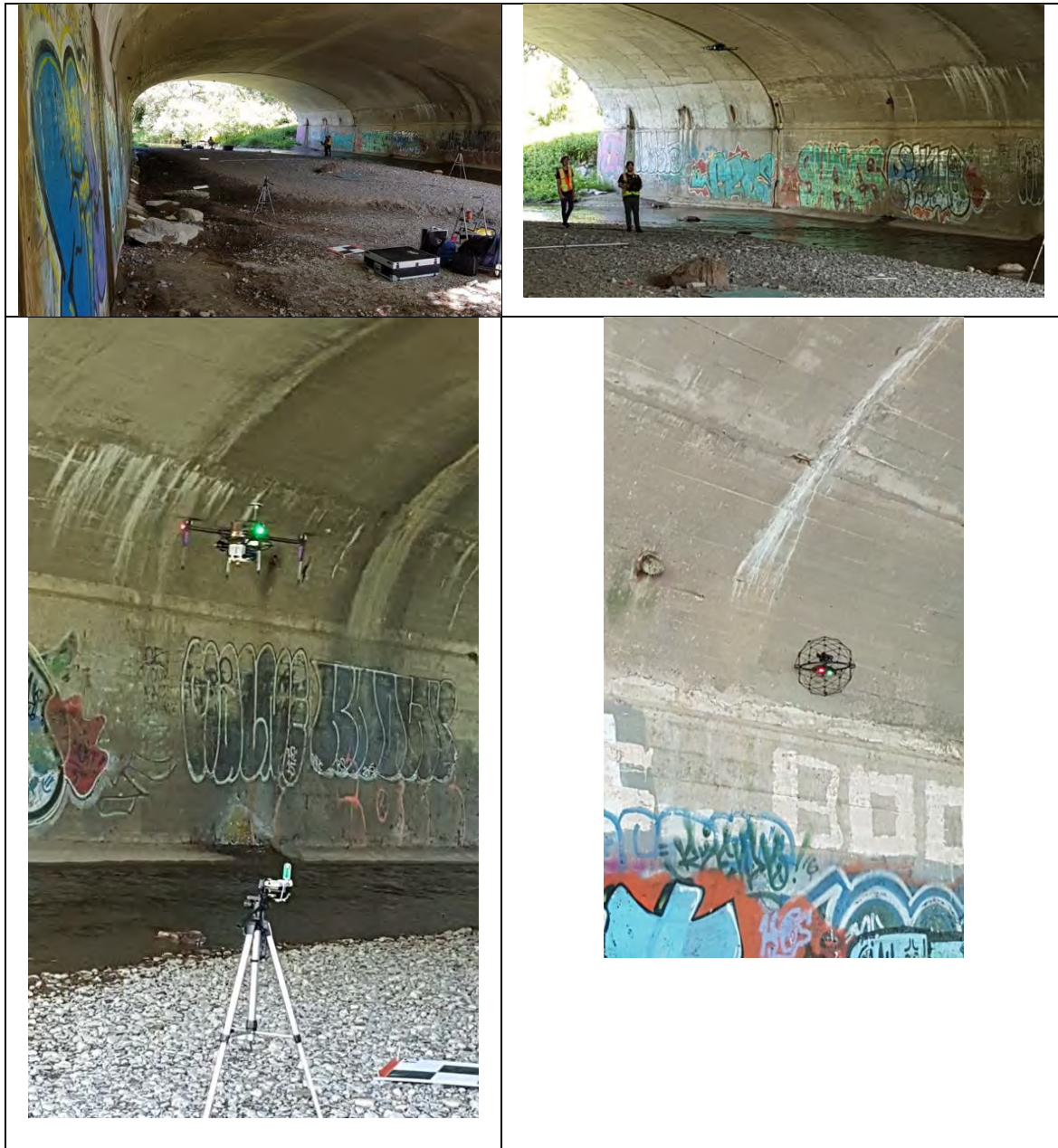
Table 6: Number of Images Captured in Oshawa Region Using M100

M100 Flight Number	Number of Captured Images
1	432
2	310
3	326
4	263
5	368
6	586
7	421
8	458
9	375
Total Number of images	3539

These counts are inclusive of images which were taken prior to the start of the survey and therefore there are images which are not included in photogrammetric processing.

The Intel Falcon 8+ equipped with Sony Alpha 7R was operated by Industrial SkyWorks Inc., a professional drone operation and data service company in Toronto. A total 623 images with 36 mega pixel resolution were captured by the Intel Falcon 8+. The Intel Falcon 8+ drone is an advanced and patented V-shaped multicoper providing multiple electronic system redundancies in power, communications and sensing for aerial-sensing solutions. The Intel Falcon 8+ can fly max 26 minutes with 2.8kg take-off weights with

triple redundant Inertial Measurement Unit (IMU) and two Global Navigation Satellite Systems (GPS and GLONASS).



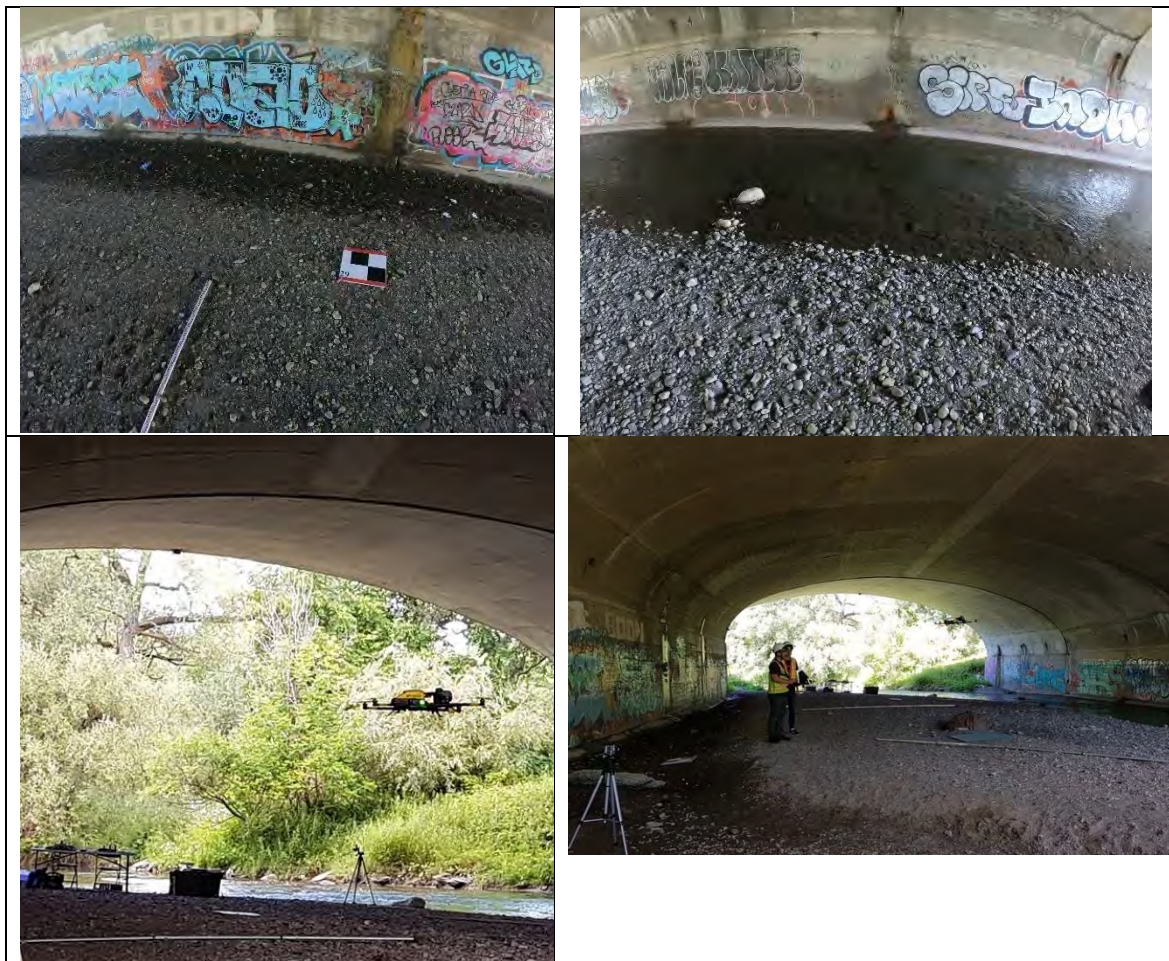


Figure 28 – UAV operations and images at the Oshawa Bridge site

PHOTOGAMMETRIC DATA PROCESSING

The nine flights were executed at different times and at different flight altitudes due to the manual control of the UAV, and mainly due to the need to change the viewing angle of the camera from nadir look to about +/- 45 degrees in order to capture both the ground floor and the cement walls of the bridge. Adjusting each flight would result in weak photogrammetric networks and would require “stitching” of the resulted strips of 3D data. In addition, the photogrammetric processing of the nine flights could not be done as one photogrammetric block due to differences in the interior orientation parameters, the viewing geometry and the large number of images due to flying low resulting in small image coverage ground footprints.

Therefore, we use the option of “chunks” available in Agisoft MetaShape. The photogrammetric project was split in several separate photo sub-blocks –“chunks”- within the project. The alignment of photos, building geometry and forming the texture mapping can be performed on each chunk separately and then the resulting 3D models may be

combined together. Working with chunks follows the general photogrammetric workflow. The program always has at least one active chunk and all the 3D model processing workflow operations are applied to this chunk.

After each chunk is created by the various photo sets the normal process workflow is applied (i.e., loading photographs, aligning them, building geometry model, building texture atlas, exporting 3D model and so on). The models in the chunks are not linked with each other.

After the "partial" 3D models are built in several chunks they can be merged together. Before merging the photo chunks, they need to be aligned. The chunks alignment / merging method can be a) point based by matching photos across all the chunks, b) camera based using the estimated camera locations, and c) marker based using the GCP (markers) as common points for the alignment of the different chunks. Chunk alignment can be performed only for chunks containing aligned photos. After alignment is complete the separate chunks can be merged into a single chunk.

A total of 1131 images of 4000 x 3000 resolution were processed using Agisoft MetaShape. The average flying height was about 5.6m above ground. Camera calibration was included in the adjustment solution. The exterior orientation parameters of the images were estimated using bundle adjustment based on the ground control points located on the ground, the walls and the ceiling of the bridge tunnel.

A number of configurations were tested consist of different photo chunks, number of GCP and number of CHK points. Given below are the results of the configuration of all 9 photo chunks with 13 GCP and 11 CHK points, respectively. The accuracy of the ground points used was of 2cm, while the parameters of the exterior orientation were treated as free parameters (very low positional and angular accuracies). The accuracy of the image measurements was set to 0.5 pixels.

Oshawa Bridge Photogrammetric Network Configuration:

UAV	Nominal Altitude of Images	Area	Images	Ground Coordinates	GCP 3D Accuracy
M100 HERO7 Black	5.6m	Oshawa	1131	Surveying	2cm

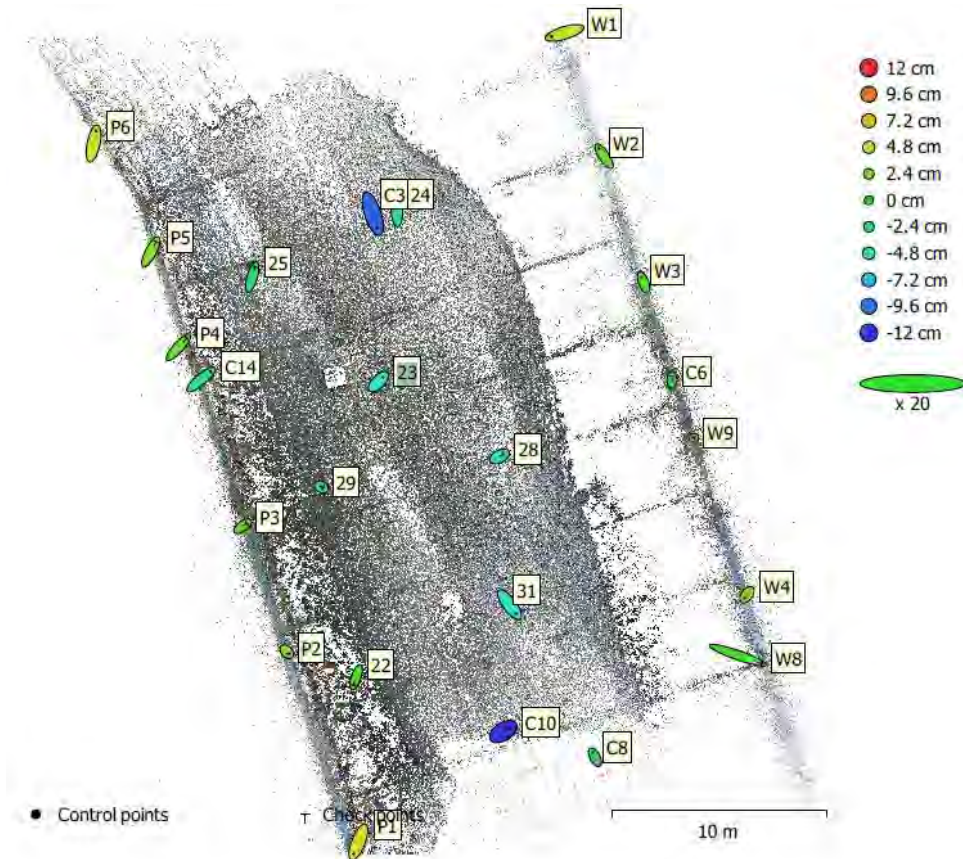


Figure 29 - GCP locations and error estimates

Z error is represented by ellipse color. X, Y errors are represented by ellipse shape.

Estimated GCP / CHK locations are marked with a dot or crossing

Table C-A: RMSE Control Points

GCP (#)	X (cm)	Y (cm)	Z (cm)	XY (cm)	Total (cm)	Image (pix)
13	2.7	3.6	4.8	4.5	6.6	2.5

Table C-B: RMSE Check Points

CHK (#)	X (cm)	Y (cm)	Z (cm)	XY (cm)	Total (cm)	Image (pix)
11	3.9	3.4	4.3	5.2	6.7	2.5

Label	X error (cm)	Y error (cm)	Z error (cm)	Total (cm)	Image (pix)
C3	2.11285	-6.4011	-10.2564	12.2733	3.957 (4)
C8	-1.09568	2.10424	-1.83208	2.99748	2.281 (3)
C14	4.53319	3.77446	-2.88897	6.5683	4.771 (6)
W1	-6.13238	-1.84193	5.12307	8.20028	1.416 (12)
W2	-2.42408	3.58571	1.97919	4.75928	1.705 (13)
W3	-1.11388	2.83083	1.44613	3.36833	2.565 (20)
W4	-1.01489	-1.36795	3.14485	3.57651	3.756 (21)
W9	0.0209751	0.032963	0.31306	0.315488	2.382 (18)
P1	-2.16839	-5.51735	6.22555	8.59654	0.541 (5)
P2	0.826495	-0.807411	2.65978	2.89991	1.036 (14)
P6	1.17566	5.73902	5.50249	8.03715	0.881 (7)
23	2.09856	2.10567	-5.42782	6.18862	1.256 (6)
31	3.18158	-4.23716	-5.98879	7.99635	1.085 (4)
Total	2.67843	3.63954	4.80845	6.59859	2.517

Table 4. Control points.

Label	X error (cm)	Y error (cm)	Z error (cm)	Total (cm)	Image (pix)
C6	0.0587702	1.69324	-1.21664	2.08584	4.069 (18)
C10	2.5534	1.68226	-11.7344	12.1263	2.772 (5)
W8	11.27	-3.90357	0.664152	11.9454	4.093 (15)
P3	2.03388	1.44869	1.60218	2.96688	0.911 (22)
P4	3.86658	4.25303	1.74583	6.00722	1.019 (17)
P5	2.41355	4.75979	2.8946	6.0712	1.406 (8)
22	-1.28646	-3.81801	0.947155	4.13875	0.851 (9)
24	-0.164428	4.93635	-3.51941	6.06472	0.901 (5)
25	1.37137	4.7797	-2.0427	5.37576	0.777 (4)
28	1.85779	1.00806	-5.1173	5.53664	0.775 (5)
29	0.801516	-0.438199	-3.25905	3.38465	2.712 (12)
Total	3.88594	3.39486	4.34716	6.7471	2.489

Table 5. Check points.

Due to the complexity of the image block the accuracies are in the range of 3-5cm despite the low flying height. We also note the image residuals are also larger than the expected sub-pixel ones as they are in the range of 2.5 pixels. This is most likely due to the weak performance of self-calibration due to insufficient GCP per image block.

Solving for all images simultaneously allows for the generation of georeferenced products for the complete coverage and representation of the bridge, such as georeferenced sparse and dense point clouds, DSM, colourised point clouds, and texture mapping (Fig. 31, 32, 33 and 34). These products can serve for the bridge visualization but also as tools for bridge inspection, assessment and maintenance engineering works.





Figure 30 - Oshawa bridge - Photogrammetrically generated georeferenced point clouds

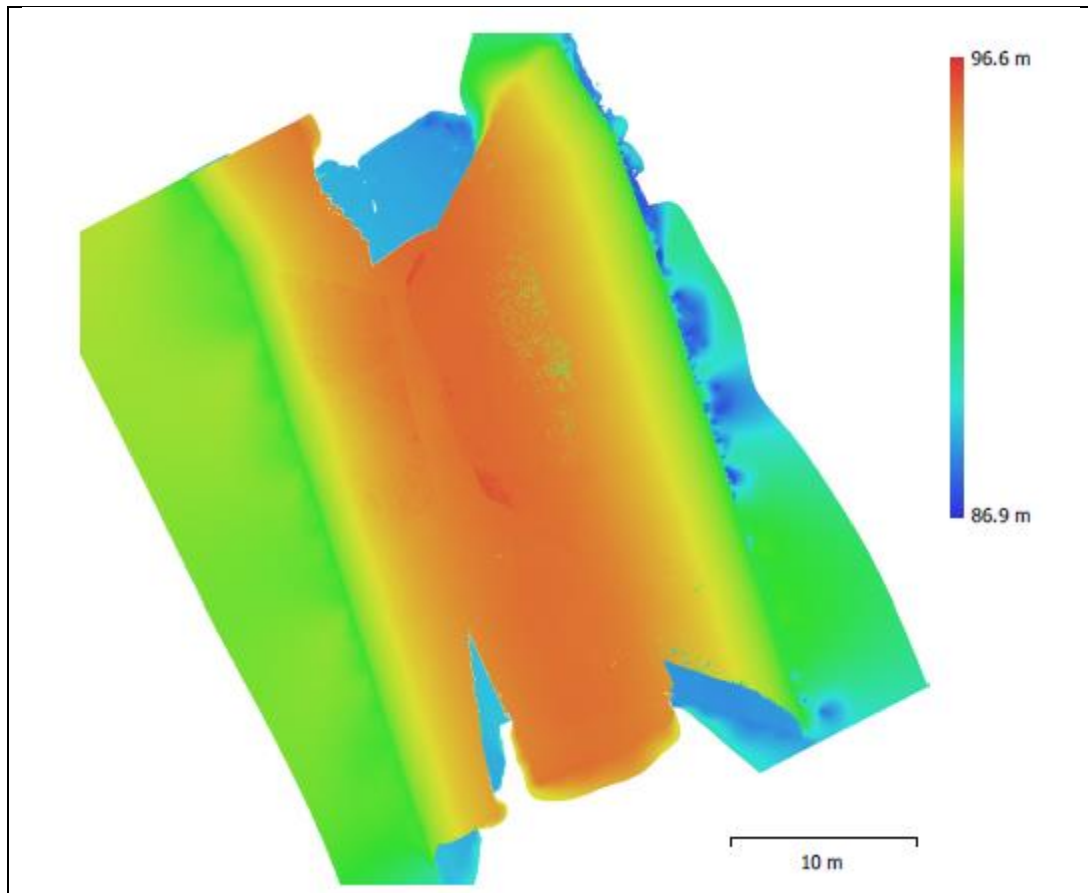


Figure 31 - Oshawa bridge - Photogrammetrically generated georeferenced DSM

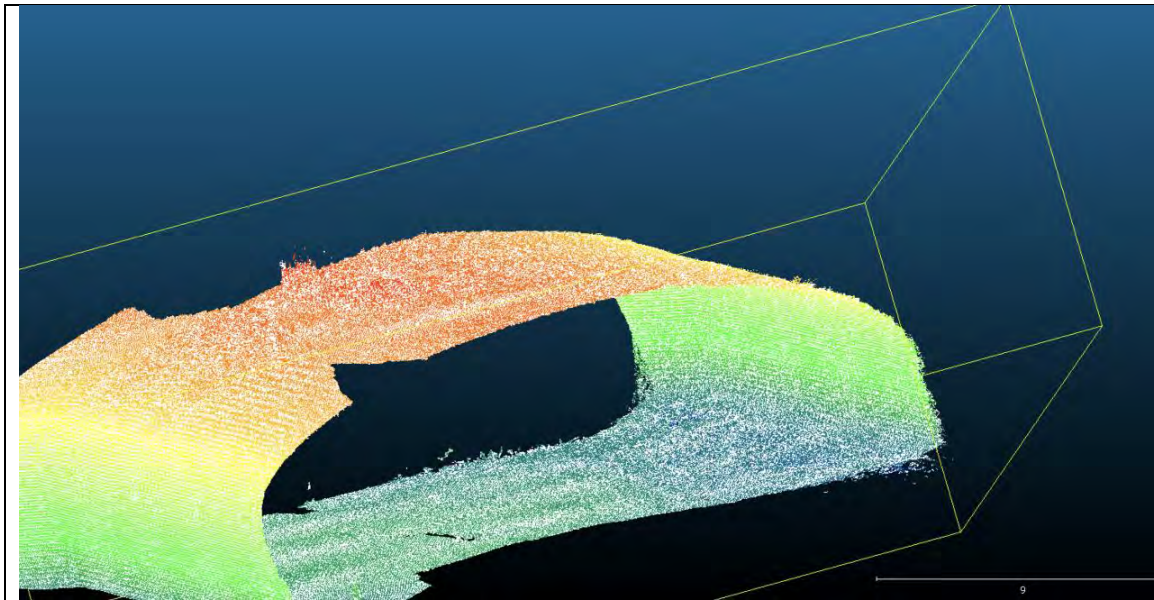


Figure 32 - Oshawa bridge - Photogrammetrically generated georeferenced sparse point cloud

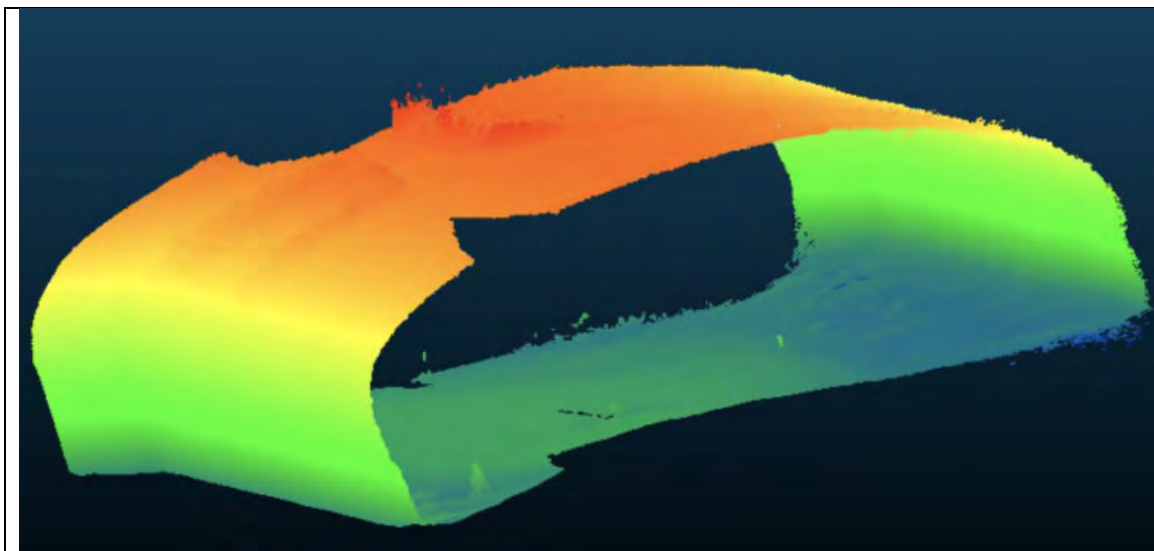
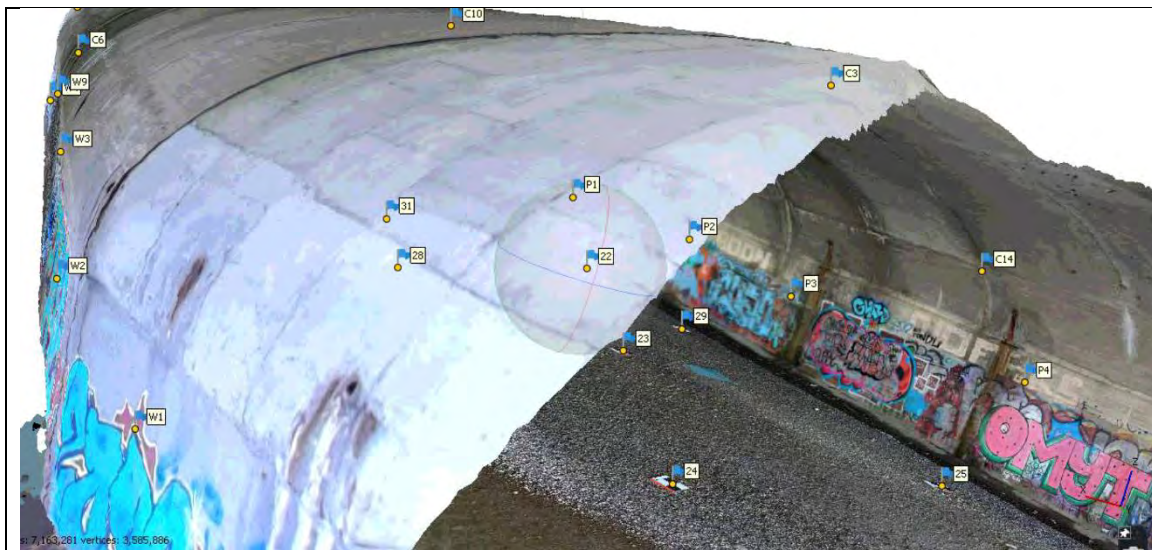


Figure 33 - Oshawa bridge - Photogrammetrically generated georeferenced dense point cloud



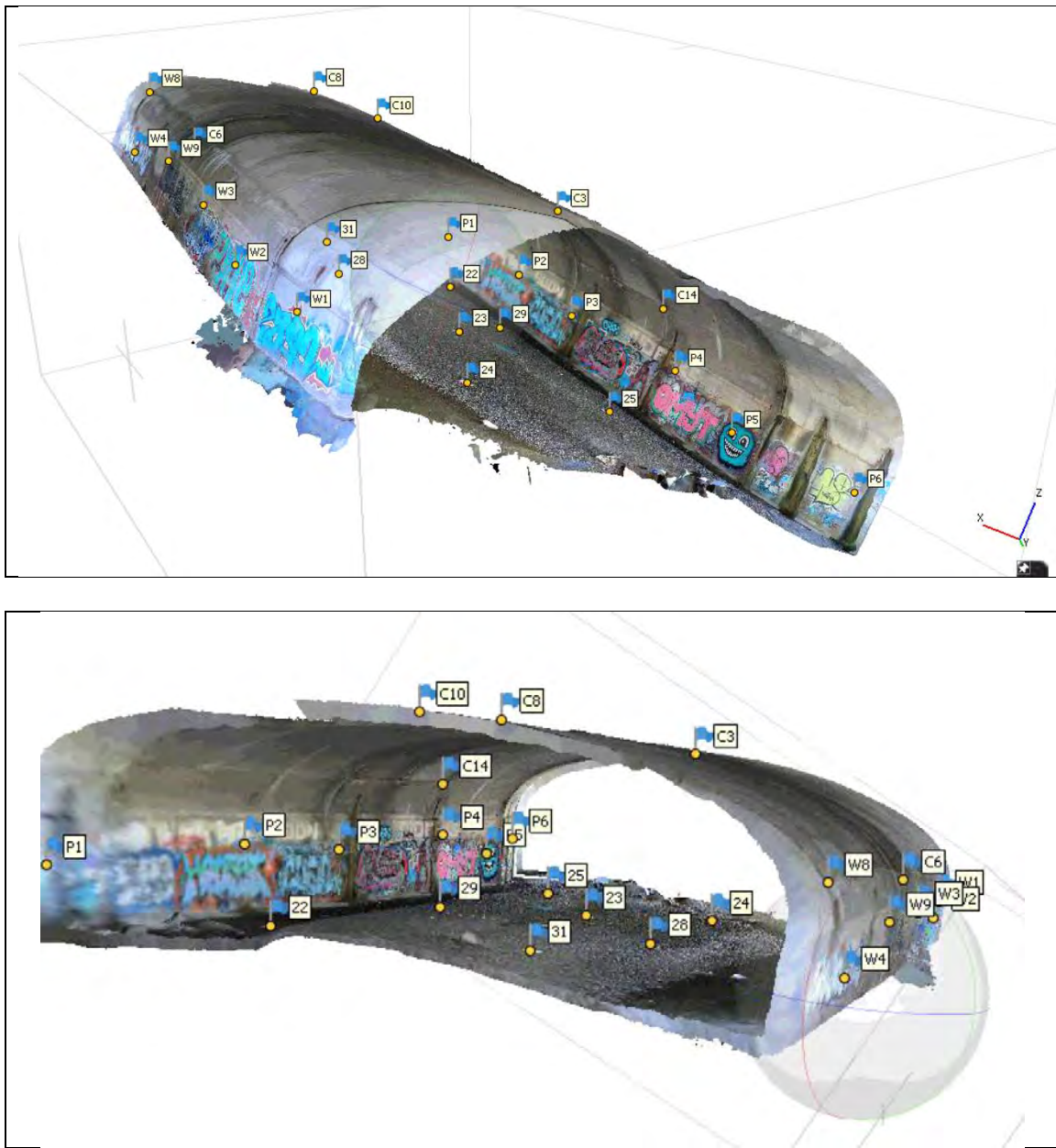


Figure 34 - Oshawa bridge - Photogrammetrically generated texture mapping

UAV Bridge Mapping – St Catharines QEW Steel Girder Bridge

The second selected bridge was the St Catharines QEW Steel Girder Bridge (Garden City Skyway), where the Span 9 was selected for the field testing. The bridge is located at lat: 43° 10' 02.19" N and lon: 79° 12' 24.39" W, St Catharines, ON (Fig. 35).

The UAV survey conducted on August 28, 2019. The M100 and the Intel Falcon-8+ UAVs were used in manual control as flying under the bridge was a GNSS-denied area. Strong winds were present making the manual piloting of the UAV quite challenging, as there was no automatic stabilization due to lack of GNSS signals as we were operating under the bridge.

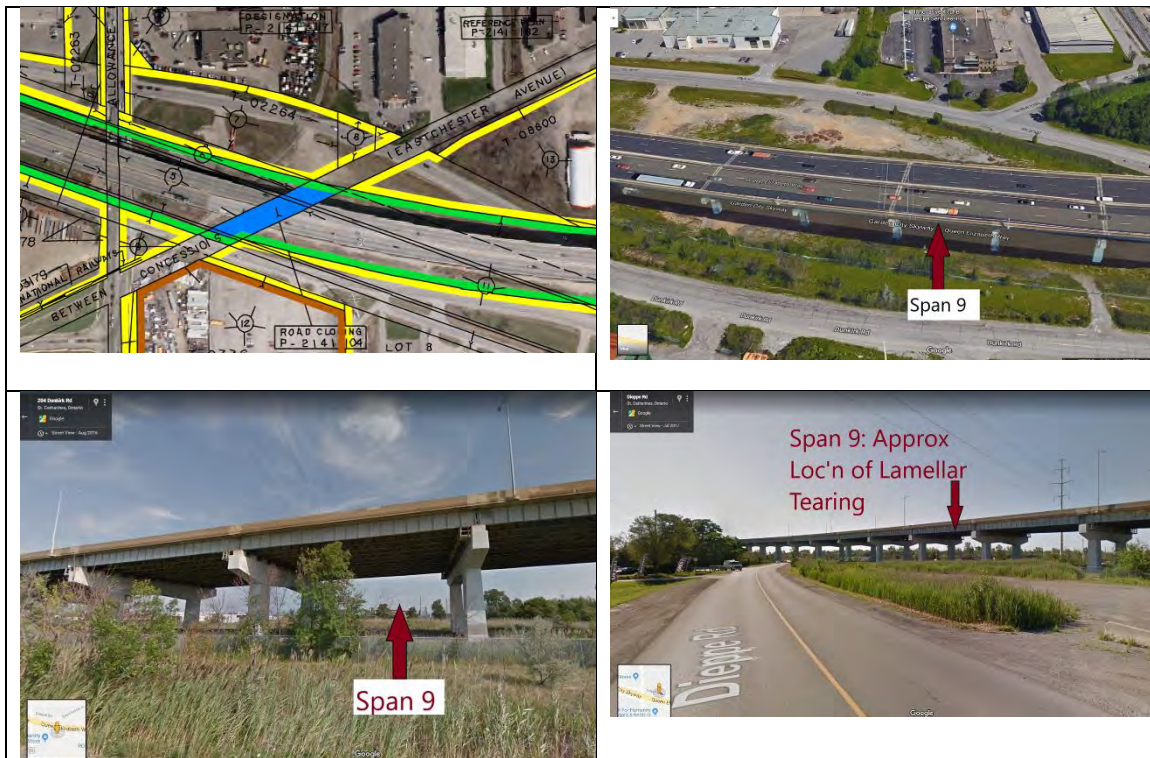


Figure 35 - Location and views of the St Catharines bridge

BRIDGE PLANIMETRIC SURVEY NETWORK

In the St. Catharine's survey area, 4 points were surveyed using GNSS methods while a total of 45 points, including the previous 4, were surveyed using a total station (TS). A traverse of 6 points was set for the total station survey.

To perform the transformation, the local coordinates of the total station observed points were shifted from P25_Local to P25_GNSS and rotated by the difference in azimuths of P25_Local-BASE_Local and P25_GNSS-BASE_GNSS.

Transformation residuals between expected coordinates (ex. GNSS derived coordinates) and transformed coordinates suggest an error to occur in the GNSS measured coordinate of point G1 (Fig. 36). This is further supported by the error in 3D position provided in it's GNSS post-processing report.

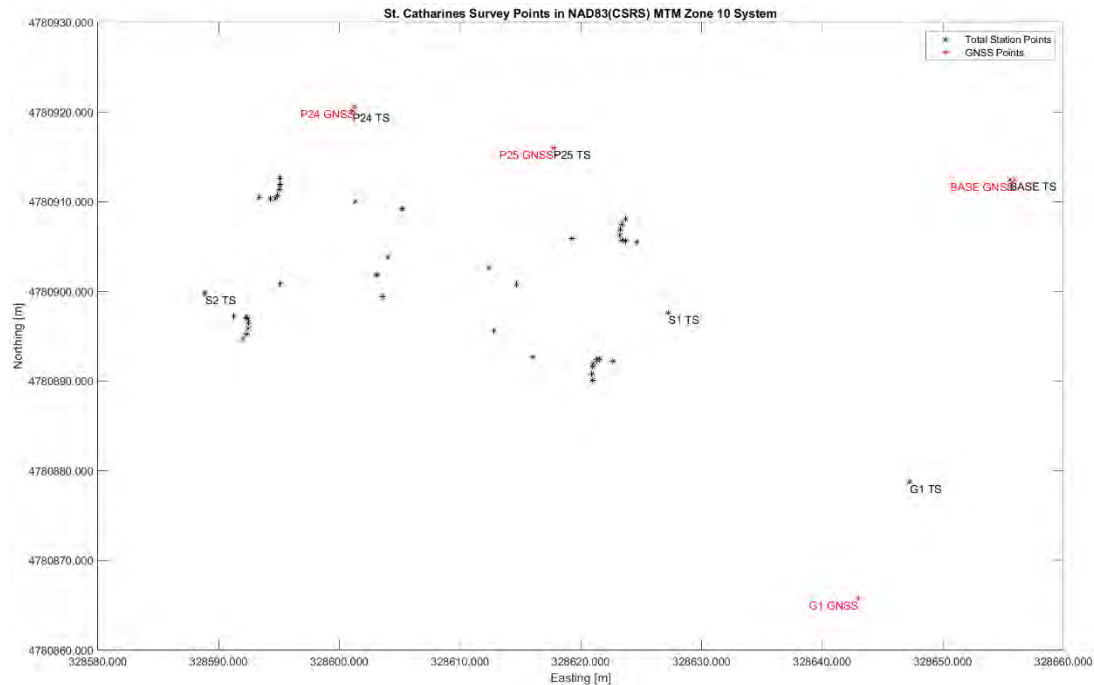


Figure 36: Transformed St. Catharines' area total station coordinates as compared against GNSS measured points

The ground point network is shown in Figure 26, while the details of the computations and the coordinates of the ground points are given in Appendices C and D.

BRIDGE PLANIMETRIC SURVEY NETWORK ADJUSTMENT

A total of 6 control points was used when traversing in the Oshawa region – S2, P24, P25, BASE, G1, and S1.

To solve the network, a total of 57 observations were used – 19 directional angles, 19 zenith angles, and 19 slope distances. The system had 37 degrees of freedom, with a total of 24 unknowns (the XYZ of each of the 6 points). Being constrained, the coordinates of S2 and P24 were held fixed.

VERTICAL SURVEY NETWORK

In the St. Catharines' survey area, only trigonometric levelling was performed (Fig. 37). However, in a similar manner as in differential levelling, first the orthometric heights of the defined traverse points were found and adjusted, then heights were propagated to remaining survey points.

It is observed that a large discrepancy exists between the GNSS derived orthometric heights and levelling determined orthometric heights for points G1 and BASE. It is believed that this is a result of a poor GNSS survey of the points (as suggested by their large positional errors in the GNSS processing report). It is believed that the GNSS survey points have had incorrect antenna heights entered when processing and surveying, therefore causing errors in determined ellipsoidal and orthometric heights.

AERIAL SURVEY

As in the Oshawa survey region, the Intel Falcon 8+ and M100 with the GoPro HERO 7 camera were also flown in the St. Catharines bridge region.

Similarly to the Oshawa bridge site, multiple flights were conducted by the M100, and several datasets of the bridge images were acquired. A summary of the total number of images captured through each of its flight is provided in the Table 7 below. Again, these counts are inclusive of images which will not be included in processing.

As in the Oshawa bridge, the Intel Falcon 8+ flight was conducted by an external company and the collected data were not available at the time of the writing of this report. A total of 940 images was collected by the Intel Falcon 8+. However, results have been shown to us.

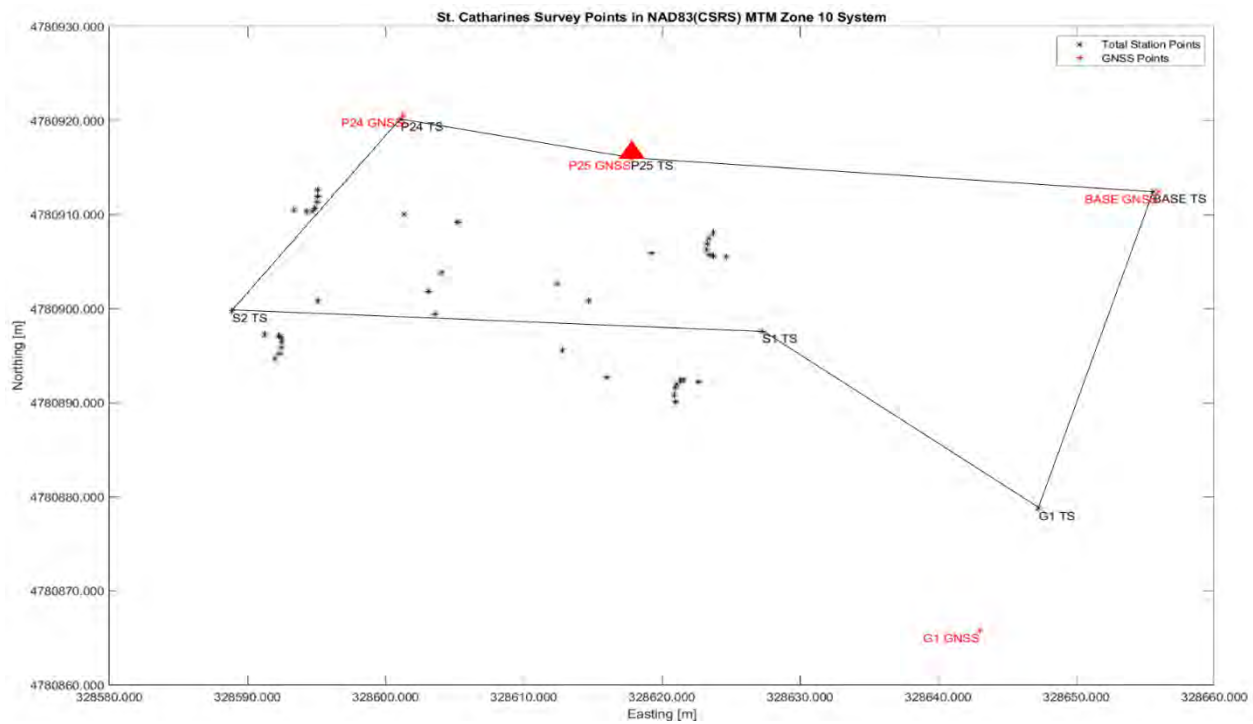


Figure 37: Levelling Loop of St. Catharine's Survey Area

Table 7: Total Number of Images Captured in St. Catharines Site using the M100 UAV

M100 Flight Number	Total Number of Captured Images
1	568
2	511
3	604
4	505
5	397
6	271
7	585
8	795
9	568
Test	753

Q-Drone System for HWY and Bridge Inspection

Precise positioning of the Unmanned Aerial Vehicle (UAV) is critical to conduct many sophisticated civil and military applications in challenging environments. Many of the-state-of-the-art positioning methods rely on active range sensors. Among many available ranging sensors, Ultra-wideband (UWB) can provide many benefits such as high precision, power efficiency, and not prone to multipath propagation and noise. Thus, the UWB has recently been attracting many interests from the research community as a complementary positioning sensor. However, there is a significant lack of UWB benchmark data available to support developing, testing and generalizing their own positioning methods using UWB sensors. In this paper, we present a unique benchmark dataset that provides UWB and IMU signals acquired by a Q-Drone system in a diverse environment, including an indoor, open field, close to buildings, underneath the bridge, and semi-open tunnel. This benchmark also provides ground truth of UAV positions independently measured with robotic total stations. In this paper, we present the characteristics of the UWB benchmark dataset, Q-Drone UAV platform and the results of the quality assessment conducted by a baseline positioning algorithm implemented with multilateration principal and non-linear optimization (Fig. 38).

Over the last decade, UAV technologies have been significantly advanced in small vertical takeoff and landing (VTOL), positioning, navigation, sensing and computing technologies. This fast technology advancement enables today's UAV to provide adequate payload, endurance, and operational facility for a wide range of civil and military applications. There are many application fields, in which UAV can complement or replace the existing labor-intensive practices. Especially, asset inspection such as telecom towers, building facades, hydroelectric towers, oil tanks, flare stack, mine cliffs and dams have a vertical structure. The health status of these vertical assets must be inspected on a regular basis. Currently, certified climbers conduct most of the vertical asset inspection by taking photos and measurements with handheld devices. These labor-centric inspection methods are prone to error, tedious, costly, and above all, dangerous due to the restricted movement of the climber (Sa & Corke, 2014).

To address these issues, the use of climbing robots and static sensor networks have been successfully demonstrating their applicability to these inspection tasks. However, the proposed techniques also show their own limitations: requiring a direct contract with the surface to obtain data, complicated mechanical design and dynamic analysis (Kim et al., 2008); requiring a pre-installation of necessary infrastructure and high maintenance costs (Chae et al., 2012).

Recently, UAV has been rapidly attracting much attention from research and industry community as a primary tool of asset inspection. Low weight UAVs reduce hazards due to their deployment and are capable of holistically capturing the reality of asset environments. However, one of the critical roadblocks to hinder its immediate adaptation for the metric inspection applications is unreliable accessibility to GNSS signals, which is the primary source of UAV positioning. GNSS can be blocked in indoor space or cause significant errors when it operates near to vertical assets or in the urban canyon. To overcome these deficiencies, many researchers have been actively studying UWB ranging data for achieving a precise positioning of UAV in both indoor and outdoor environments. As a leading-edge radio frequency technology, UWB sensor can potentially provide cm-level accuracy over up to 1 km with a high data rate (e.g., 125 Hz). UWB can increase immunity to interference due to lower spectral power density and robust to multipath propagation. Recent research works discussed the potential of UAV positioning using UWB in outdoor (Li et al., 2018) and indoor (Zhao et al., 2020) environments. Despite the promising results shown in these research works, the performance of the proposed methods was evaluated with private data, which makes it challenging to discuss perspectives of different positioning methods in a normalized research environment.



Figure 38: Positioning System Overview in Different Environments

In this project, we present a unique UWB benchmark dataset, called Q-Drone UWB benchmark. Q-Drone system, a UAV with UWB network built at York University, was used for acquiring this benchmark over five different sites, which include an indoor, open sport field, near to a building with glasses, semi-open tunnel and underneath bridge. The benchmark data were acquired by flying for a total of 1h 50min 28 sec flight time and about

4.3km traveling distances with different maneuvering patterns and spatial configuration between UAV and UWB anchors as shown in Table 8.

Table 8: Datasets Provided in This Research

Site	Environment	Location	Area
Indoor	Indoor	Oshawa, Ontario, Canada	26m(w) x 33m(l)
Field	Outdoor, open sport field	Uxbridge, Ontario, Canada	12m(w)x13m(l)
Building	Outdoor, close to building	Newmarket, Ontario, Canada	7m(w)x7m(l)
Bridge	Semi-open outdoor, under a concrete-metal bridge	Niagara, Ontario, Canada	10m(w)x23m(l)
Tunnel	Semi-open outdoor, under a metal bridge	Oshawa, Ontario, Canada	8m(w)x30m(l)

Related Works

Since 2005, the Federal Communications Commission authorized and set the regulation on the UWB systems for unlicensed use (Federal Government, 2004). Ever Since using UWB sensors for positioning of a moving platform has generated a lot of interest and is considered in many research works. Positioning with UWB is often referred to as a 3D position estimation problem using UWB ranges. Using another sensor alongside UWB like inertial and visual sensors is considered to achieve a higher positioning accuracy.

To handle the problems of estimating the position different methods are being used, for example, non-linear least squares, geometrical algorithms, filtering-based methods like Kalman filter or smoothing-based approaches. There are papers published recently trying to improve conventional methods. Park et al. (2020) presented a multilateration approach to correct geometric ambiguity and showed an effective improvement in errors caused by geometric ambiguity. Li et al. (2018) proposed an Extended Kalman Filter (EKF) algorithm to combine UWB with Inertial Measurement Unity (IMU) in an indoor experiment. Tiermann et al. (2015) also investigated the potentials of UWB for indoor positioning purposes. Their study showed the developed method could achieve 10 cm positioning accuracy in 2D and 20 cm in 3D. By fusing gyroscope and UWB, Mueller et al. (2015) estimated the dynamic state of a quadcopter in an outdoor experiment with static atmospheric conditions. To compensate for the inaccessibility of GNSS signals, Zahran et al. (2018) integrates radar, IMU and a UWB sensor on the quadcopter with a large number of UWB distributed in an open area. Kang et al. (2020) present a novel smoothing approach for UWB-aided UAV positioning. They integrate two types of UWB based measurements

and inertial measurement into a unified factor graph framework and showed that it helped produce better accuracy and robustness.

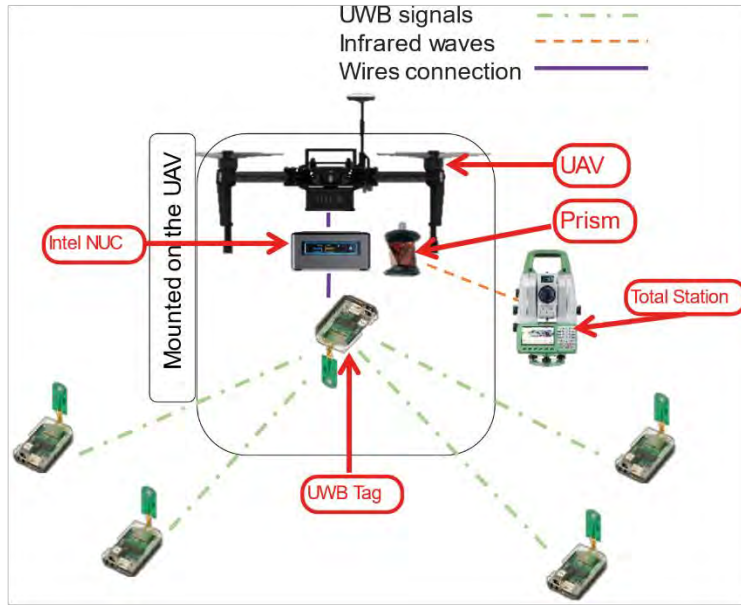


FIGURE 39: SENSORS AND UAV CONFIGURATION

In recent years, several research groups have made their efforts to make UWB data available in public research domains. One of the available datasets is provided by the Institute for Dynamic Systems and Control, ETH Zurich (Ledergerber & Adrea, 2019a; Ledergerber & Adrea, 2019b). The datasets were collected by a Roomba robot moving in 2D motion on the floor with different indoor 2D scenarios for collecting UWB range measurements. This dataset provides channel impulse response (CIR) and range measurements for supporting different signal processing methods (such as received signal strength (RSS), time of arrival (ToA), and time difference of arrival (TDoA)). LocURa4IoT is a UWB-based testbed used for the dataset presented by Bossche et al. (2018). The dataset was collected for a moving reference node across two motorized rails in a 100 square-meters room in different temperatures and 10 UWB anchors. Few other UWB datasets can be found in other research domains. Ridolfi et al. (2018) is a UWB Indoor Positioning for Sport postures. Heydariaan et al. (2018) released a benchmark dataset to study the effect of the material of the walls in non-line-of-sight for an indoor environment. It is worth mentioning that despite a large number of previous researches investigating UWB-based positioning methods, to our best knowledge, there is no benchmark dataset available for supporting the UAV positioning researches in both indoor and outdoor environments. Having access to benchmark datasets is necessary to validate and compare novel methods based on the standard ground.

Q-Drone System

A. UAV Platform and Onboard Sensors

For acquiring the UWB benchmark, we have been developing a UAV system, called Q-Drone. We designed the Q-Drone system for conducting engineering inspections to generate 3D asset environments and detect anomalies in a GNSS-denied environment. The Q-Drone system aims to achieve UWB-based positioning, dynamic path planning, automated quality assessment of the inspection mission and computer vision-based anomaly detection. The current Q-Drone system used in this study enables UWB-based positioning based on pose graph optimization and multi-trilateration techniques (Park et al., 2020; Kang et al., 2020). The system was built based on DJI Matrice 100 with a maximum of 1.3 kg payload capacity. This platform mounts our payload, which consists of UWB tag (112 grams), Intel NUC computer (728 grams) and battery (542 grams). Fig. 40 shows a configuration of the Q-Drone system.

B. UWB Anchor System

TIME DOMAIN™ used to make UWB radio transceiver, called P400. In this experiment, we used a total of 5 PulsON 440 modules, which is one of the P400-family. UWB anchors have four UWB tags mounted on tripods at different heights in a square shape arrangement on the ground. By using Time-of-Flight (TOF) method, it can provide distance measurement between two or more sensors by 2 cm accuracy and up to 125 Hz rate. The UWB anchors can work in temperatures above -40°C and lower than 85°C in high shock and high vibration environments.

C. Robotic Total Station

To have ascertainable and reliable data to validate positioning methods, we used a robotic total station, which is a discontinued prism tracking total station. One GRZ101, 360° mini prism was mounted on the UAV, and the total station actively tracked it using a modulated infrared light wave. Due to its small size, the GRZ101 provides the highest pointing accuracy of 1.5 mm (Sa and Corke, 2014). We used two different types of robotic total stations. For the indoor, bridge and tunnel datasets, Leica Nova MS60 MultiStation was used with the ability to measure range up to 1000m with $1''$ (0.00027°) angle accuracy. For the outdoor dataset, Trimble VX Spatial Station with the ability to measure up to 5,500 m with 4 mm accuracy and 0.4 sec measurement time was used for acquiring the reference positioning data.

D. Communication System

Flight platform of DJI Matrice 100 can be customized through an onboard software development kit (SDK) provided by DJI. The mounted NUC computer was connected to the Micro-USB (Universal Serial Bus) port on the UAV. The SDK allows the computer to communicate with the flight controller and onboard sensors. Through this SDK, onboard IMU data was fed to the NUC computer in a real-time manner. Another mounted sensor on the UAV is the UWB antenna tag. The UWB tag mounted was connected through USB to the NUC computer. Through this connection, a stream of data including ranges between

the UWB onboard tag and four UWB anchors deployed on the ground is sent to the onboard computer. We also mounted the GRZ101 prism on the UAV platform that measures the XYZ using the total station.

System Calibration

A. Time Synchronization

All the sensors employed in the Q-Drone system collects the data in their own clocks. To synchronize the data collected by different sensors, all the sensors should adjust their clocks to a reference clock so that they can use the same time reference. To achieve this goal, we used the NUC time as a reference clock to regulate the reference of other clocks. We implemented a data communication layer based on the DJI's SDK to transfer the time reference of IMU and GNSS to the NUC. The UWB ranging data is directly connected the NUC through USB so that the time reference of UWB is synchronized to the NUC clock. The onboard sensors should be also time-synchronized with the robotic total stations. The time-synchronization was conducted by implementing a systematic translation between the onboard sensor data and total station measurement.

B. Displacement Calibration

Fig. 40 illustrates three coordinate frames: UAV body frame, UWB network frame and total station frame. The UWB network frame was used as our base frame coordinate system.

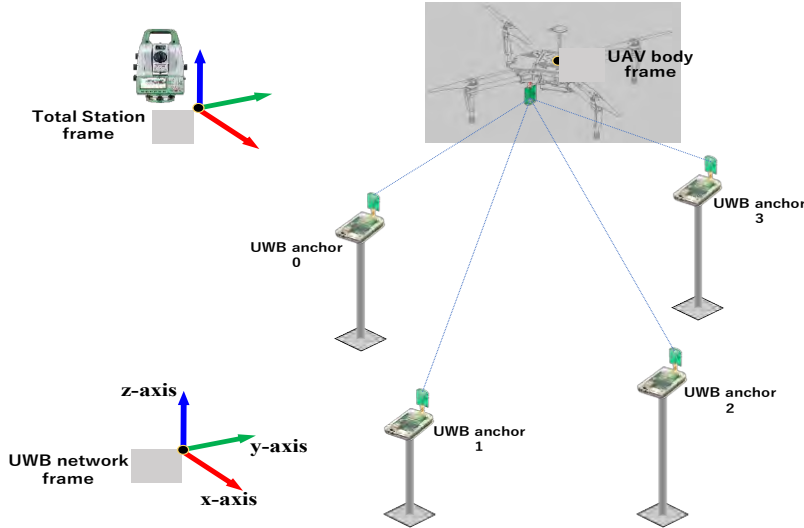


FIGURE 40. Q-DRONE COORDINATE SYSTEMS

1) *Total Station-UWB Displacement Calibration:* As shown in Fig. 40, we used a network of four UWB anchors, {UWB0, UWB1, UWB2, UWB3}, deployed on the ground and one UWB tag, mounted on the UAV platform. The location of all UWB anchors were measured before the flight. We define a global coordinate system of the UWB network in a

2D plane where the position of UWB0 is considered as the origin of the UWB network frame; a linear translation vector between UWB0 and UWB1 is considered as the x-axis, and the z-axis of the network frame is the same as the height of the robotic total station. The ground truth data collected by the total station was translated to the origin of UWB network frame.

2) *IMU-UWB Tag Displacement Calibration:* IMU provides the linear acceleration, angular velocity, height, and absolute orientation of the UAV. An offset distance vector between IMU and UWB tag need to be calibrated for using the height of IMU. The IMU is at the center of the control unit, which placed in the middle of the UAV body. The location of the sensors on the UAV was fixed, and an offset vector, V , between the UWB tag with respect to the UAV's center of gravity was measured. UAV's center of gravity is in the intersection of propellers' beams and at the same level as the rotation plane. The vector components shown in Fig. 41 are defined as

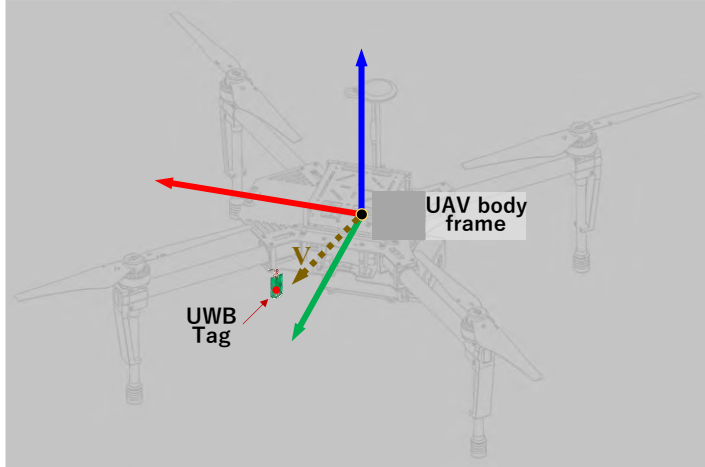


FIGURE 11. Q-DRONE COORDINATE SYSTEMS

3) *Height Calibration:* The height data provided by the IMU and the z data of the total station needs to be calibrated. We also know that as we defined the height data of UWB network frame, it is the same as the total station z direction. The height data provided by the IMU is the relative height from its initial position which depends on the first location of the UAV at the beginning of the flight. This translation was conducted by implementing a translation between the IMU height data and total station z measurement. The translation is shown in (2) where Z_{TS} is the total station z measurement, H_{IMU} is IMU height data and Z_{TS0} is the initial data captured by the total station.

$$Z_{TS} = H_{IMU} + Z_{TS0} \quad (2)$$

4) *Range Calibration*: A range calibration is required for approximating the raw range measurement obtained with the UWB sensors to the ground truth range data acquired by the robotic total stations. A small deviation between the raw range data and ground truth measured in the same local coordinate system might exist. This range deviation might be due to systematic or non-systematic errors induced by differences between two sensor systems, flight environments and sensor configurations. Thus, the raw range data needs to be calibrated with the range correction coefficients described in (3). These coefficients are estimated in (4). The error between the rectified range and ground truth range is minimized through linear regression method.

$$R_{cal} = aR_{UWB} + \bar{b} \quad (3)$$

$$S = \sum_{i=1}^N (aR_{UWB} + \bar{b} - R_{GT})^2 \quad (4)$$

where R_{cal} represents the calibrated range, R_{UWB} is the raw range data acquired by the UWB sensor, R_{GT} is the ground truth of range data, a is the estimated range scale factor, b is the range bias coefficient, S is the total squared difference between the calibrated range data and ground truth data. All data are used in NUC time frame.

Baseline Positioning Method

A. Outlier Removal

For validating the quality of the benchmark data, we implemented a simple data processing pipeline to estimate the position of the UAV using the raw UWB data received from a UWB tag. As a first step of the positioning pipeline, we implemented a two-stages outlier filtering module: a pre-processing stage for removing outliers of the raw range data and a post-processing stage for remove outliers from the positing result.

As presented in Ridolfi et al. (2018), a scholastic model of the UWB outliers can be parameterized with an optimizer such as Kalman filter. In this framework, a predicted noise state associate with observed range data can be used for a hypothetical outlier test. However, the performance of this stochastic approach heavily depends on the accuracy of *a priori* assumption of noise characteristics and positioning algorithms adopted. In this study, we employed a regional consensus-based thresholding technique to filter-off outlier range data (Kang et al., 2020). Given N consecutive range data set, $R_n = \{R_1, R_2, \dots, R_N\}$, a range proximity between two adjacent data, D_T , is heuristically determined. This norm of outlier data is used as a threshold value to conduct a hypothetical outlier test of R_i by comparing a range difference between R_i and R_{i-1} with D_T . However, instead of determining the outlier state of R_i with comparison of its adjacent data only, the outlier decision of R_i is made only if any member from a range kernel ($N=8$) is identified as the outlier. However, R_i is determined as the inlier only if all the members from a range kernel are identified as the inliers. This regional consensus-based thresholding is described in (5) and (6):

$$\Delta R_n = |R_n - R_{n-1}|, \quad n = 1, 2, \dots, N \quad (5)$$

$$\begin{cases} \text{if } \Delta R_n, \Delta R_{n-1}, \dots, \Delta R_{n-N} < D_T \rightarrow R_n \text{ is inlier} \\ \text{if } \Delta R_n \text{ or } \Delta R_{n-1} \text{ or } \dots \text{ or } \Delta R_{n-N} > D_T \rightarrow R_n \text{ is outlier} \end{cases} \quad (6)$$

The similar logic of this thresholding technique is also applied to eliminate further the outliers of the range observations, not based on the regional consecutive range dataset, but using a set of consecutive position dataset. This position-based consensus thresholding algorithm is applied to the range data as a post-processing stage.

B. Outlier Removal

Most of UAV positioning algorithms rely on computer vision-based odometry or GNSS signals. However, these methods might face some difficulties due to undesirable illumination, texture-less environments, signal blockage in indoor environments and multipath of reflected signals. On the other hand, some research groups have proposed range-based techniques such as Extended Kalman filter (Zhao et al., 2020), multidimensional scaling (MDS) (Cui, 2016), triangulation (Esteves, 2003) and trilateration (Zhou et al., 2012). In this study, we implemented a multilateration positioning algorithm based on time of arrival (TOA) reported in More (1977) as a baseline positioning model for validating the quality of the benchmark dataset. Given a set of the range and the positions of the anchors, the approximate position of the UWB tag is the solution of (7), where n is the number of the anchors. The minimum number of three anchors are required to determine the position in 3D ($n=3$). In our experiment, we used four anchors. In some instances of time, the range data from one anchor might fail to be received. In this case, the algorithm solves the equation by three range data ($n=4$). In (7), $P_{n,x,y,z}$ is the position of the reference point defined by the total station.

$$\begin{bmatrix} 1 & -2P1_x & -2P1_y & -2P1_z \\ 1 & -2P2_x & -2P2_y & -2P2_z \\ 1 & -2P3_x & -2P3_y & -2P3_z \\ \vdots & \vdots & \vdots & \vdots \\ 1 & -2PN_x & -2PN_y & -2PN_z \end{bmatrix} \begin{bmatrix} X^2 + Y^2 + Z^2 \\ X \\ Y \\ Z \end{bmatrix} = \begin{bmatrix} R_1^2 - X_1^2 - Y_1^2 - Z_1^2 \\ R_2^2 - X_2^2 - Y_2^2 - Z_2^2 \\ R_3^2 - X_3^2 - Y_3^2 - Z_3^2 \\ \vdots \\ R_n^2 - X_n^2 - Y_n^2 - Z_n^2 \end{bmatrix} \quad (7)$$

where $n = 1, 2, \dots, N$

To overcome problems like multipath, and non-line of sight signals and also refining the multilateration solution we used the Levenberg–Marquardt optimization algorithm (More, 1977). The multilateration outcome has been used as an initial point of the optimization problem. The objective function includes the geometric distance between the UWB tag and

anchors. IMU height Z_{imu} as another constraint is added to the objective function to overcome the negative height result as

$$F = \lambda(Z_{imu} - Z_{MLAT})^2 + \sum_{i \in n} (R_i - \|x_{MLAT} - Pn_{x,y,z}\|)^2 \quad (8)$$

where $x_{MLAT} = [X_{MLAT}, Y_{MLAT}, Z_{MLAT}]$ is the position calculated by the multilateration, R is the ranges measured by the four UWB anchors, $Pn_{x,y,z}$ is the position of the reference point defined by the total station and λ is a regularization parameter.

Data Acquisition Results

A. Overview

As shown in Table 8, the Q-Drone system described in the previous section was used for collecting the UWB benchmark dataset over five different sites. The benchmark sites have diverse characteristics, including indoor, open field, semi-open tunnel, under a bridge and near a building. These diverse environmental characteristics provide optimal conditions for evaluating the performance of testing positioning algorithms in various settings. During the field data acquisition, we slightly changed the configuration of payload sensors, anchor network and platform of the Q-Drone system depending on the chosen site. In this section, we describe a specific configuration adopted in each site and explain the formats of the measurement data and calibration.

B. UWB Configuration

The UWB system has two components: 1) UWB antenna mounted on the UAV platform, and 2) four anchors set on the ground. The configuration of these two components affects the performance of the UWB-based positioning. In our experiment, two different settings of spatial arrangement between the prism and UWB antenna was adopted depending on sites as described below:

(1) *Side antenna configuration for Indoor dataset*: We attached the UWB antenna tag at the side of the platform body, while the battery and the computer were mounted under the UAV platform. The side placement of the antenna can minimize the body occlusions by installing the tag in an open space. The prism was installed at the bottom of the platform to maximize its visibility so that the total station can keep tracking it. It is shown in Fig.42.a.

(2) *Central antenna configuration for Outdoor datasets*: The central configuration is similar to the side confirmation. However, it was designed for placing the UWB antenna tag at the center of the UAV platform to minimize the UWB signal blockage caused by the UAV platform while maximizing its mobility. The central antenna configuration was adopted for all the Outdoor datasets (Field, Building, Bridge and Tunnel) shown in Table 8. It is shown in Fig.42.b.

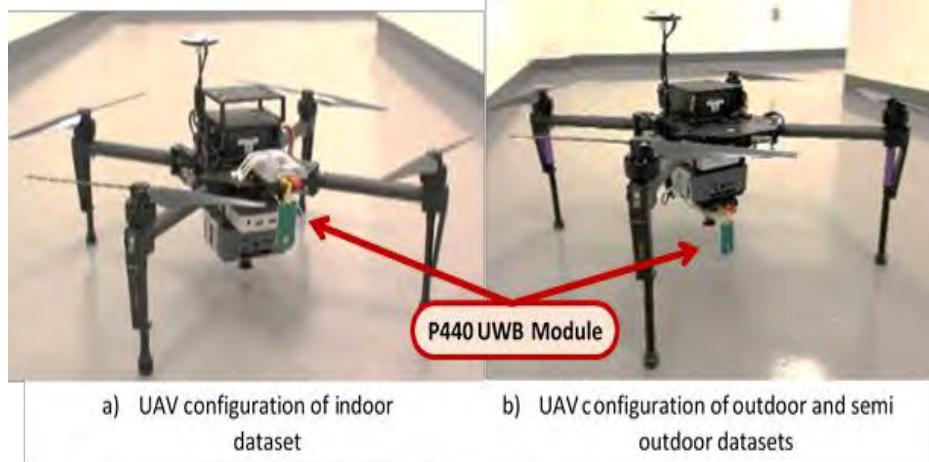


FIGURE 42. UWB TAG

In each test site, we deployed the four UWB anchors on the ground with different spatial configurations. All the spatial arrangements of the ground anchor network follow a rectangular shape, but with different physical dimensions due to the accessibility limited by each site.

C. Data Acquisition Results

(1) *Results*: Table 9 presents a summary of the benchmark data acquired by Q-Drone system. Q-Drone acquired total 23 flight datasets over five test sites (789.4m^2) by traveling about 4.3km during 1h 50min 28 sec. In this benchmark, a total of 253,832 UWB data were acquired together with total 302,647 IMU heights and 605,311 IMU data. In addition, total 20,827 ground truth of range data was measured with the robotic total stations. The physical dimension of the prism is about 30 mm providing a pointing accuracy of 1.5 mm. Due to its small size, the robotic total station might fail to track the prism, which causes missing data in certain period of times. In this case, we filled the missing information in the ground truth for matching them to the raw range measurement using spline interpolation method. The benchmark datasets consist of free motion in indoor environment, square and zigzag pattern in an outdoor field, scanning the walls of an outdoor building, sweeping the ceiling under a bridge, and scanning walls of a tunnel.

(2) *Range accuracy*: As shown in Table 9, we evaluated the accuracy of UWB range measured by comparing them to ground truth obtained with the robotic total stations. We obtained 0.902m Mean Average Error (MAE) of the range accuracy over the five sites. We observed larger RMSE in Building and Tunnel sites as the UWB range data observed were corrupted by multipaths due to the complexity of the structures present in those sites.

TABLE 9. Q-DRONE BENCHMARK AND UWB RANGE ACCURACY

Sites	# of data	Duration (s)	Travelled distance (m)	Area (m ²)	UWB MAE (m)
Indoor	5	1,687	1,260.88	91.96	0.37
Field	5	2,313	1,780.52	158.74	0.17
Building	3	823	388.92	50.10	2.02
Bridge	4	726	330.02	246.80	0.34
Tunnel	6	1,079	504.47	241.80	1.61
Total	23	6,628	4,264.81	789.4	0.902

(3) *Range calibration:* The range accuracy was measured after the observed ranges are rectified with the range correction coefficients explained in Section “System Calibration”. To avoid the overfitting problem, the range correction coefficients were estimated with a sample range and position data acquired by a test flight. The estimated coefficient was applied to the rest of the data for further analysis and position estimation. Fig. 43 shows an example of the range data measured with the four anchors from one of the benchmark datasets. For each anchor, matching three different types of range data (i.e., raw rage, calibrated range and ground truth) are shown. For this set of data, the average error between ground truth and UWB ranges is estimated at three anchors less than 25 cm, while showing less than 50 cm at the remaining anchor. This error was calculated for the raw data without considering the outlier removal.

(4) *Missing range data:* The stream of UWB data coming from four anchors in a random sequence. There are certain instances that one anchor’s data does not get received due to signal blockage, sensor failure or areas like above the anchors that two sensors do not face each other. In these points, the algorithm solves the problem by three ranges data.

D. Evaluation of Baseline Positioning Results

(1) *Results:* We applied the baseline positioning algorithm to the range corrected benchmark dataset after outliers were removed using the regional consensus-based filtering algorithm. Table III describes the baseline positioning results. We used MAE to measure the error between the baseline positioning results and ground truths. As shown in Table 10, the baseline algorithms achieved 0.74m MAE in xyz over the five sites using the benchmark dataset. Field, Bridge and Indoor sites shows less than 1m of positioning accuracy, while Building and Tunnel achieved relatively larger errors. Fig. 44 shows representative trajectories selected for each site, which are computed by the baseline positioning algorithm and ground truths.

(2) *Missing data:* As stated earlier, there are certain instances that the UWB tag might fail to receive the UWB range signal from one of the four anchors due to signal blockage, body occlusions and sensor failure. In this case, the positioning solution can be solved with three ranging data.

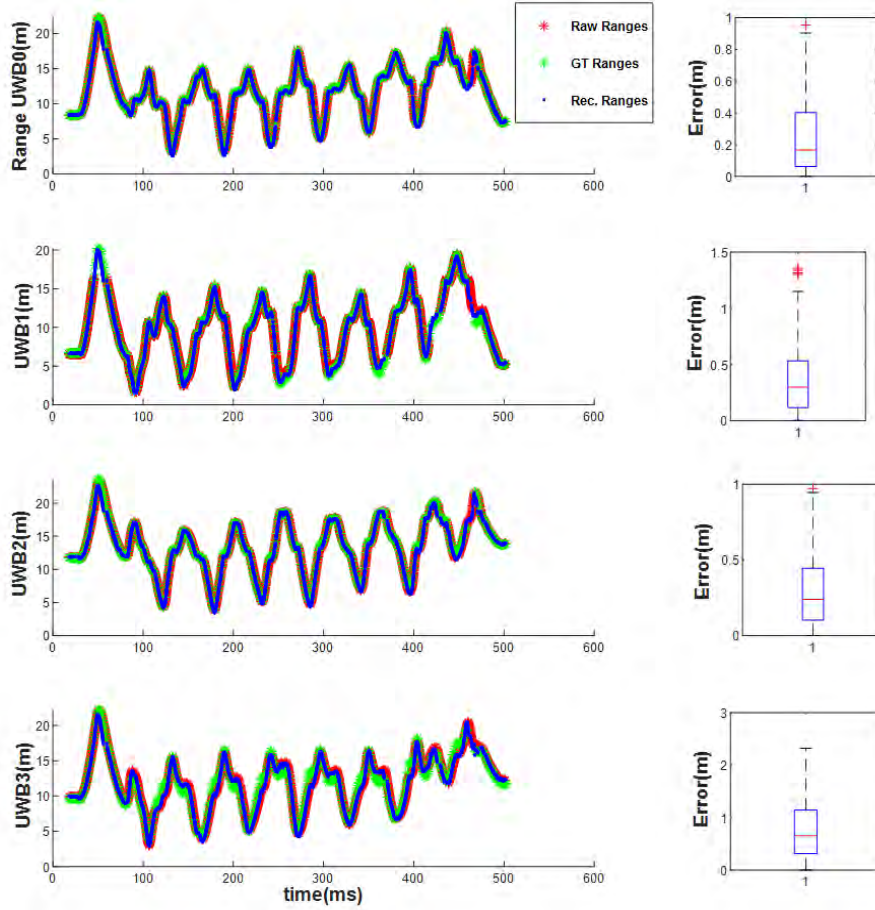


FIGURE 43. RANGE DIFFERENCE BETWEEN UWB AND GROUND TRUTH

TABLE 10. THE RESULT OF MULTILATERATION INDICATING MEAN ABSOLUTE ERROR (UNIT: METER).

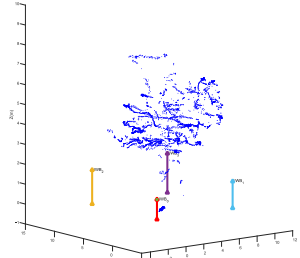
	Indoor	Field	Building	Bridge	Tunnel	Mean
x	0.655	0.245	1.570	0.283	1.094	0.769
y	1.141	0.208	2.253	0.185	1.623	1.082
z	0.566	0.292	0.305	0.302	0.393	0.372
xyz	0.787	0.248	1.376	0.257	1.037	0.741

(3) *Multipath issues:* During the acquisition of the building dataset, we observed that at a certain height the data shows a significant shift in range. We found that this range shift is caused by the well-known multipath issue when UWB signals are reflected by glass walls placed in the building facade. After a certain height, the angle between the signal and the glass wall becomes critical to increase the reflectivity of the UWB signals and thus produce

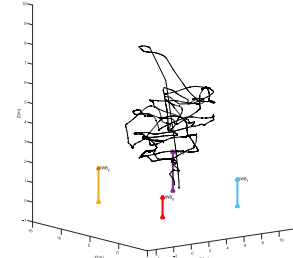
multi-paths in the received ranges. Also, we found that there might be a possibility that the multi-paths in received ranges can be caused by the aluminum surface covering the building facade. We also observed the similar patterns of multipath from Tunnel datasets. These multi-paths ranging issue can be fixed by introducing another set of coefficients that are provided in the benchmark dataset. A more detailed study of error sources of UWB data is beyond the scope of this paper. Errors including the effect of multipath propagation, antenna radiation patterns, and non-line-of-sight are addressed in Shen et al. (2008) and Uvarov et al. (2019).

Benchmark Dataset

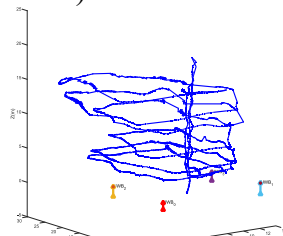
The Q-Drone benchmark datasets acquired over the five sites are publicly available via a benchmark website (<https://benchmark.qdrone.ausmlab.com>). This benchmark website will provide: 1) sensor datasets (i.e., UWB ranging data and IMU), and 2) calibration parameters. The benchmark users can submit the results of their own positioning methods computed with the benchmark dataset. The benchmark website will evaluate the performance of the submitted positioning results based on the reference positioning data of UAV tracked with the robotic total stations. The evaluation results will be informed to the users.



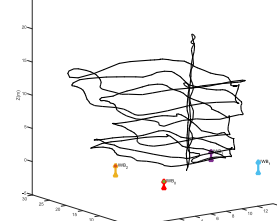
A.1) Indoor dataset



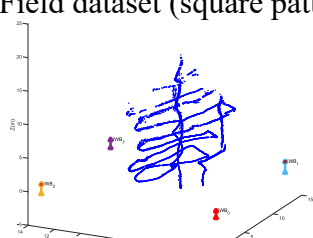
A.2) Indoor dataset ground truth



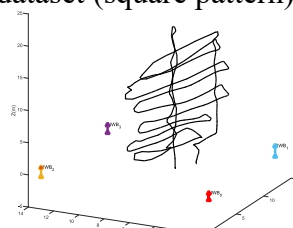
B.1) Field dataset (square pattern)



B.2) Field dataset (square pattern) ground truth



C.1) Field dataset (zigzag pattern)



C.2) Field dataset (zigzag pattern) ground truth

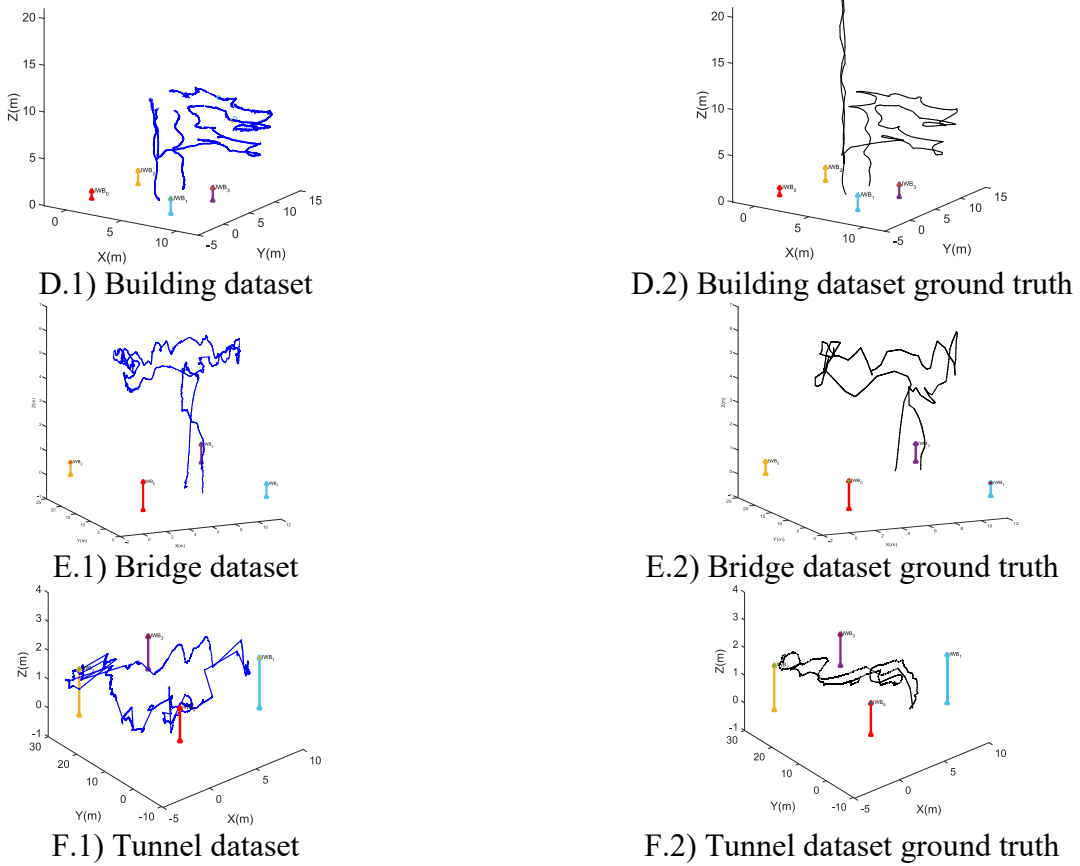


FIGURE 44. MULTILATERATION RESULT AND GROUND TRUTH OF A) INDOOR DATASET B) FIELD DATASET, SQUARE PATTERN C) FIELD DATASET, ZIGZAG PATTERN D) BUILDING DATASET E) BRIDGE DATASET F) TUNNEL DATASET

Conclusion and Future Works

In this project, we present the Q-Drone system and UWB benchmark dataset for supporting UAV positioning research works. The Q-Drone system was designed for positioning a UAV platform using UWB sensors in various types of GNSS-denied environments including indoor, open field, close to buildings, underneath the bridge and semi-open tunnel. The Q-Drone system acquired the IMU and UWB data, which were time-synchronized with the onboard computer clock. The ground truth of UAV positioning was acquired by tracking a mini prism mounted with UAV platform with the robotic total station. An extrinsic sensor calibration between IMU and UWB tag, and between UWB anchors and the robotic total position was conducted. Also, the coefficients of range correction between raw range data and its ground truth were estimated. To validate the quality of the benchmark dataset, we implemented the multilateration positioning algorithm with Levenberg–Marquardt optimization as well as the consensus-based filtering algorithms to remove range outliers. The Q-Drone benchmark data will be publicly available through the benchmark website for supporting UAV positioning research works

using UWB range data. We expect the provided benchmark dataset will contribute to the identification of the limitation of positioning methods under development and the validation of its performance in diverse real environments. In our experiments, we demonstrated that Q-Drone system can position UAV systems with the accuracy of 26 cm in bridge case and 1m in semi-open tunnel (MAE). These results were obtained with a naïve outlier filtering algorithm. In our future research work, we will develop a more advanced outlier algorithm excluding multi-path noises and replace our multi-lateration algorithm with pose-graph optimization method. Also, we will integrate positioning results obtained from camera with UWB.

Crack Detection Using Deep Neural Convolutional Network

As our infrastructure becomes further developed and expanded, new systems are required for the maintenance of this complex and intertwined network. One facet of this problem is the identification and inspection of bridges for physical damage (i.e., cracks, corrosion). Standard practice for inspections requires that humans be directly on the ground. This is time-consuming, expensive, and often infeasible due to the sheer scale or safety concerns. The next step, and the focus of this report, is to streamline this process through the automation of the bridge inspection process with deep learning for computer vision. A convolutional neural network (CNN) architecture like U-Net is used to complete this semantic segmentation task. Despite lacking a large dataset of images for bridges, knowledge transfer is employed by training the network with similar data from roads. The network will be trained on a large dataset of partially labelled images of major provincial highways provided by the Ministry of Transportation Ontario (MTO). To solve the issue of the incompletely annotated data, a generative adversarial network (GAN) will help to augment the amount of available training data available for the CNN. The end goal will be to allow the network to take images of various surfaces and perform a semantic segmentation task to identify and label instances of damage according to its severity. Using the method outlined will potentially cut the monetary and time costs of inspections and create a safer and more efficient transport network, while remaining compliant with inspection regulations.

Bridges form part of the infrastructure backbone that supports the rest of modern society. With such importance placed upon our bridges, it is imperative that they be well maintained, both for the sake of efficiency and for civilian safety. Bridge inspections are traditionally performed manually, with a trained professional engineer for this bridge. This poses an immediate concern in terms of efficiency and scale. The scope of the issue is further compounded by the breakdown of the situation in regard to age. As of 2016 in Ontario, the average of a bridge was 39 years old. However, as seen in Figure 45, many more are significantly older and are approaching or exceed half a century since their date of construction (Mermigas, 2018). The aging of our basic infrastructures necessitates that emphasis be placed on maintaining these structures to extend their lifespan and assure consistent and safe access to the public. Failure to meet these demands could result in unreliable operation of critical infrastructure, thus affecting urban sustainability. As recognized by the Government of Canada's 2016 Investing in Canada plan, \$180 billion in infrastructure will be invested over the 12 years of the Plan.

As reported by Duzgum et al. (2016), visual inspection to identify issues affecting the status of structural health of the bridge using camera has proven its efficiency for general inspections. For instance, the visual inspection method can be sufficient in identifying preliminary issues for smaller bridges with no known structural problems. For larger

structure requiring more in-depth investigation, the visual inspection coupled with structural health monitoring system can be used in identifying potential problems and areas for a more sophisticated monitoring system deployment.

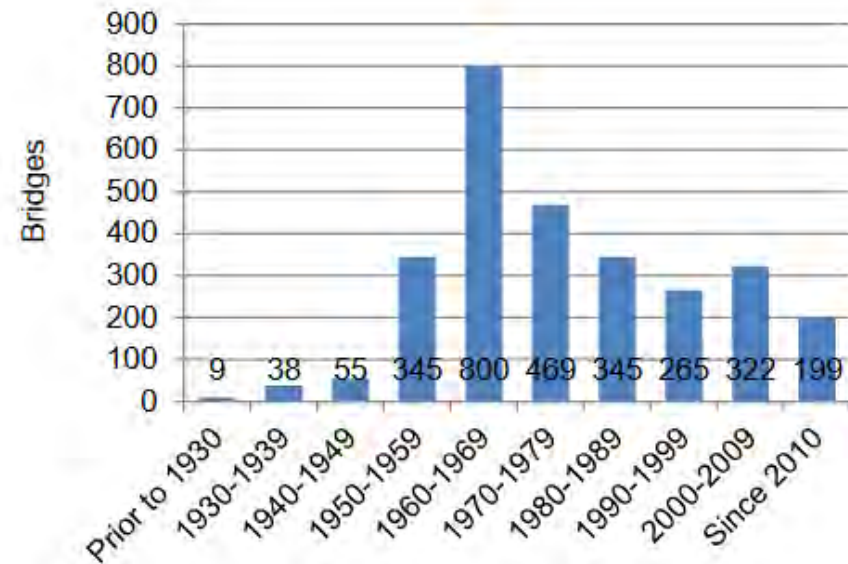


Figure 45: Decade of Construction of Ontario's Provincial Bridges

Previous studies (Hassanain & Loov, 2003; Yu et al., 2007; Oh, et al., 2009; Montero et al., 2015) demonstrate successful applications of vision-based infrastructure-inspection using autonomous systems, e.g., unmanned aerial vehicles (UAVs) (Newcome, 2004). Inspection using autonomous systems is both more challenging and more rewarding compared to conventional inspection methods performed by experienced humans. For instance, UAVs can provide a higher level of accessibility to remote structures without risking human lives Bolourian, 2017; Gomez and Purdie, 2016; Salvini et al., 2015). However, they have limited endurance; thus they need to cover the area of interest as fast as possible. They also cannot get too close to structure due to the uncertainties in their positioning systems. Therefore, in order to observe the damages both accurately and completely, their cameras should offer larger fields of view and higher spatial resolutions, i.e., larger images in both dimension and details. While various types of damages can be automatically detected from images, e.g., spalling (Headyati et al., 2015) and discoloration (Greenings & Landren, 1966), we focus on identifying cracks identifying cracks in this study. Cracks are amongst the most common types of damages in concrete structures, which are typically challenging to identify due to their small size and their visual similarity to edge-like features in concrete texture (Fan et al., 2018).

In this project, we propose in an effort to streamline the inspection process, a deep learning-based approach trained on a semantic segmentation task in order to take image inputs of a structure and output the location of cracks and other structural damage. This method could simplify the inspection process and allow for faster and cost-effective visual inspection of

the bridge infrastructure.

Related Works

Deep Convolutional Neural Network: With advancements of deep-learning approaches, techniques of object detection and semantic segmentation based on deep convolutional neural networks (DCNN) have gained popularity for identifying and characterizing cracks. The main challenges, that these approaches face, include: 1) accessibility to adequate annotated data as well as 2) applicability to large-size images. With regard to the first problem, there are a few datasets publicly available for crack segmentation (Pzgenel, 2019; Shi et al., 2016; Chambon & Moliard, 2011). However, they do not represent a complete range of challenges in real-world scenarios, *e.g.*, ambiguous texture patterns, varying illumination conditions, high resolution, and large field of view. One of the main reasons for the limited availability of crack segmentation datasets is the complexity of manual labeling of cracks' outlines. To deal with issue, a simple solution is augmenting the training data by traditional methods, *e.g.*, applying geometric transformations and brightness changes to existing images (Liu et al., 2019; Krizhevsky et al., 2012; Cirean et al., 2011). With regard to the second problem, there exists two common ways to handle large-size images: down-sampling (Liu et al., 2019; Simard et al., 2003; Zeiler & Fergus, 2014) and cropping into small patches (Noh et al., 2015; Wu et al., 2015). In the case of crack-detection, down- sampling causes a considerable loss of information since fine cracks may only appear in the original resolution. Cropping is also not a suitable approach since the contextual and global information cannot be preserved in small patches (Noh et al., 2015); *e.g.*, the crack loses its identity as an elongated object if cropped into small segments.

Crack Detection: Crack detection on concrete structures has been an active area of research. A variety of approaches are used in the literature which can be divided into two categories: 1) Object Detection; and 2) Semantic Segmentation. In the first category, the goal is to identify the bounding box of the region in which the crack is located. Cha et al. (2017) applied a CNN binary classifier on the patches of a sliding window to classify them either as cracks or intact areas. Kim & Cho (2018) used a similar approach but added more output classes to help the network distinguish between false positive cases such as concrete plane joints. This category of approaches provides coarse information about the location and extension of the crack. However, in many use cases, the exact outline of the crack is needed for further processing *e.g.* metric damage quantification. Semantic segmentation methods can be applied for segmenting the detailed figure of the crack rather than merely identifying the bounding box containing it.

Semantic segmentation, otherwise known as image segmentation, refers to the task of labelling each of the pixels of an image by a class label (Thoma, 2016). Segmentation methods can be divided into two categories: 1) Conventional computer vision techniques such as morphological operations (Jahanshahi & Masri, 2013; Jahanshahi et al., 2013) adaptive filtering and Markovian modelling (Chambon & Moliard, 2011) and edge detection (Shan et al., 2016); and 2) Machine learning-based methods such

as random forest (Shi et al., 2016) and support vector machines (Fan et al., 2018). Recently, deep learning-based approaches are also utilized for segmenting cracks. Hoskere et al. (2018) used a multi-scale deep CNN to classify every pixel for seven different concrete damages. They used one network for classifying every pixel as damaged or intact, and another one for detecting the classes. The second network helped reducing false positives. Lee et al. (2019) proposed a CNN with trainable up-sampling layers for segmenting cracks. Fan et al. (2018) used structured prediction proposed in Liskowski and Kwawiec (2016) for segmenting cracks in concrete. In this category of approaches, classical computer vision techniques do not perform well in real-world complex images and require modifying the design of the algorithms from case to case. They are also prone to errors due to environmental changes such as lighting condition. On the other hand, machine learning- based methods can be robust to these challenges if trained with a rich training dataset. Conventional machine learning approaches are, however, trained based on features that are hand-crafted through considerable human involvement to represent the real data. In CNN-based approaches, the design of the network is also a critical factor in determining the success of the approach. Also, in all deep learning-based semantic segmentation methods, data annotation for creating training datasets is a serious bottleneck. In addition, these studies are applied to low-resolution images up to 227 x 227 pixels (Shi et al., 2016). In recent years, the application of convolutional neural networks for this task has allowed for significant improvements in this domain. Crack detection can also be cast as a problem in this domain where images of cracks are segmented between cracks as opposed to backgrounds. The network U-Net was selected for this task and is discussed in greater detail under Relevant Architectures.

Conditional Generative Adversarial Networks: Much of the architecture of cGANs are shared with standard generative adversarial networks (GANs). At their core, GANs can be decomposed into two competing networks, one being a generative network and another discriminative network. The general architecture can be visualized in Figure 47. The generative network seeks to learn a mapping between random noise vector to an output image (Goodfellow et al., 2014). The purpose of this generative network is to produce images that form part of the input the discriminator network. The discriminator network takes in a “real” image as well as a synthesized image from the generative network and is trained to distinguish between those two. The goal with these adversarial networks is that the output images of the generative network will be indistinguishable from “real” output. cGANs add an additional piece of information in the form of an observed image as input to the generative network. cGANs differ in that they learn a mapping conditioned of both an input image and a random noise vector to an output image. The network Pix2pix, belonging to cGAN, was selected in particular for the data augmentation process and is discussed in greater detail under Relevant Architectures.

There has been ongoing researches for augmenting segmentation datasets. For example, Lee *et al.* (liskowski & Krawiec, 2016) used 2D Gaussian kernels that mimic thin cracks cross-sections for enhancing their training dataset. In CNN-based approaches, traditional augmentation methods, *e.g.*, affine transformation and adding noise (Krizhevsky et al., 2012; Cirean et al., 2011; Simard, 2003), are commonly used.

GANs (Goodfellow et al., 2014) are also more recently explored for data augmentation. Liu *et al.* (Liu et al., 2019) used style transfer for enhancing their dataset. They also used GANs for generating images corresponding to manually annotated labels for augmenting and balancing their segmentation dataset. Wang *et al.* (Wang & Perez, 2018) also used GANs for style transfer to augment existing datasets. Iqbal *et al.* (Iqbal and Ali, 2018) proposed a GAN in which, by providing a label, the corresponding color image is generated. Neff *et al.* (2017) used Deep Convolutional GAN (DCGAN) to generate both the image and the label for enhancing their gray-scale medical images at a resolution of 128 x 128 pixels. However, their results were noisy and did not contribute much in improving the accuracy *i.e.*, no improvement while training their network on their full dataset, and only 0.4 improvement in Hausdorff distance while training on a reduced dataset. Bowles *et al.* (2018) presented an approach based on ProGAN in which both the image and its corresponding segmentation label are generated for brain MRI and CT scan images. The images they generated also had low resolution (128 x 128) pixels.

Transfer Learning: One significant limitation of deep learning is data dependence (A survey on deep transfer learning (Tan et al., 2018). This refers to the fact that deep learning models require a huge amount of data in order to train in comparison to traditional forms of machine learning. A second limitation is the issue of insufficient training data. This is a problem that restricts the application of deep learning in many fields due to the infeasibility of collecting a large-scale and high quality dataset. Transfer learning provides a solution for this issue by allowing for the knowledge gained in training a network for a problem in one domain to be transferred towards a problem in a similar domain. In this case, the collection of a suitable large scale dataset for crack detection on bridges would be expensive and arduous. Thus, a network trained on the detection of cracks on roads (where an in-depth labelled dataset exists) can be used as a starting point for a bridge inspection network.

Methodologies

Semantic Segmentation: U-Net is a convolutional neural network developed initially for biomedical image segmentation by Ronneberger et al. (2015) for the EM segmentation challenge at ISBI 2012 in which it outperformed all other submissions by a large margin. U-Net was proposed as a modification and extension of fully connected networks that were already the baseline for semantic segmentation tasks at the time. Its main benefit is in its high degree of accuracy with a relatively small dataset and short training time.

The architecture of U-Net can be visualized in Figure 46. U-Net can be summarized as consisting of a contracting and expanding path. In the contracting path, the image is repeatedly downsampled by applying two 3x3 unpadded convolution layers each followed by a rectified linear unit layer (ReLU) and finally applying a 2x2 max pooling operation. Each downsampling block is then followed by doubling the number of feature channels. Thus, as the downsampling reduces spatial information, the feature information is increased. The expanding path follows a similar structure as the contracting path but inverted in order to upsample the image. Upsampling blocks feature an upsampling of the

feature maps and 2x2 “up-convolution” that halves the number of feature channels, a concatenation with the correspondingly cropped feature map from the contracting path, and two 3x3 convolutions, each followed by a ReLU. The final output of the contracting path undergoes a 1x1 convolution that maps the feature map to each class in the segmentation task.

As described in the U-Net paper, the loss function used is a pixel-wise softmax over the final image combined with a weighted cross-entropy loss function. To account for the weighted loss function, U-Net introduces a weight map function w (shown in (3)) that aids in forcing the network to better segment fine boundaries. The softmax function is defined in (1) below

$$p_k(\mathbf{x}) = \exp(a_k(\mathbf{x})) / (\sum_{k'=1}^K \exp(a_{k'}(\mathbf{x}))) \quad (1)$$

where $a_k(\mathbf{x})$ denotes the activation in feature channel k at the pixel position $\mathbf{x} \in \Omega$ with $\Omega \subset \mathbb{Z}^2$. K is the number of classes and $p_k(\mathbf{x})$ is the approximated maximum-function. The cross-entropy loss function is defined as in (2):

$$E = \sum_{\mathbf{x} \in \Omega} w(\mathbf{x}) \log(p_{l(\mathbf{x})}(\mathbf{x})) \quad (2)$$

The weight map function (3) is defined as below:

$$w(\mathbf{x}) = w_c(\mathbf{x}) + w_0 \cdot \exp\left(-\frac{(d_1(\mathbf{x})+d_2(\mathbf{x}))^2}{2\sigma^2}\right) \quad (3)$$

where $w_c: \Omega \rightarrow \mathbb{R}$ is the weight map to balance the class frequencies, $d_1: \Omega \rightarrow \mathbb{R}$ denotes the distance to the border of the nearest cell and $d_2: \Omega \rightarrow \mathbb{R}$ is the distance to the border of the second nearest cell.

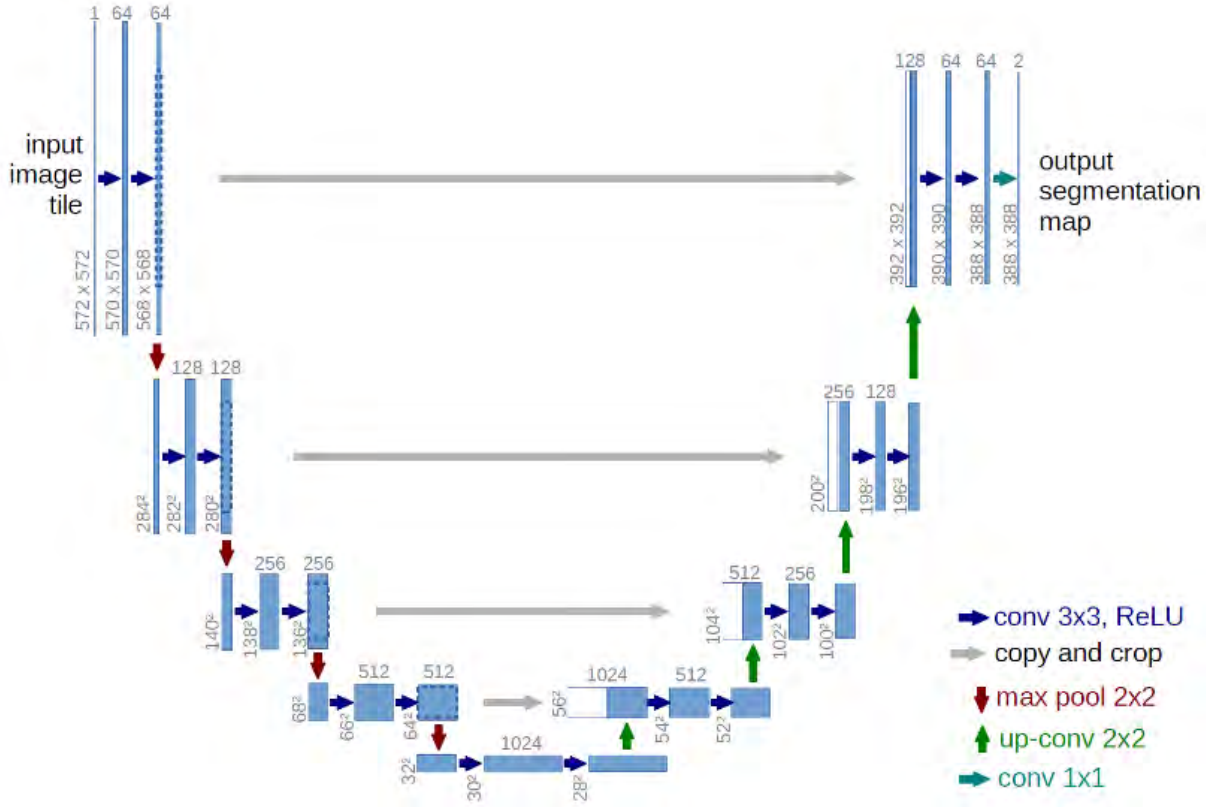


Figure 46: U-Net architecture

Pix2pix: Pix2pix is a conditional generative adversarial network (cGAN) developed for the purpose of image-to-image translation by (Isola et al., 2017). The network architecture can be visualized in Figure 47 below. Image-to-image translation allows for the translation of one image representation into another. For our purposes, we use Pix2pix to translate synthesized ground truth outputs into realistic images of cracked roads. Pix2pix incorporates U-Net’s as part of its generator network as it involves the translation of a high-resolution input image into an equally high-resolution output image with the same underlying structure. For the discriminative network, a unique architecture was proposed called PatchGAN. PatchGAN uses a sliding window approach in discriminating between “real” and “fake” and focuses on individual NxN size windows and classifies each of these patches as “real” or “fake”. The output of all the patches of an image are averaged out to get a final result for the discriminator. The motivation for this new architecture was to maintain sharp resolutions at higher frequencies in an image.

Pix2pix is trained specifically using a composite loss function consisting of an adversarial loss as well as a L1 loss. The adversarial loss influences featured below in equation (4) is responsible for measuring whether the generator model can create plausible images in the domain. The L1 loss found in equation (5) regularizes the generator model to output images that are plausible translations of the input image.

$$\mathcal{L}_{cGAN}(G, D) = \mathbb{E}_{x,y}[\log D(x, y)] + \mathbb{E}_{x,z} \left[\log \left(1 - D(x, G(x, z)) \right) \right] \quad (4)$$

$$\mathcal{L}_{L1}(G) = \mathbb{E}_{x,y,z} [||y - G(x, z)||_1] \quad (5)$$

where G and D are the generator and discriminator respectively and E is the error between the function output and the ground truth. The combination of these two losses results in the final objective of finding generator G*:

$$G^* = \arg \min_G \max_D \mathcal{L}_{cGAN}(G, D) + \lambda \mathcal{L}_{L1}(G) \quad (6)$$



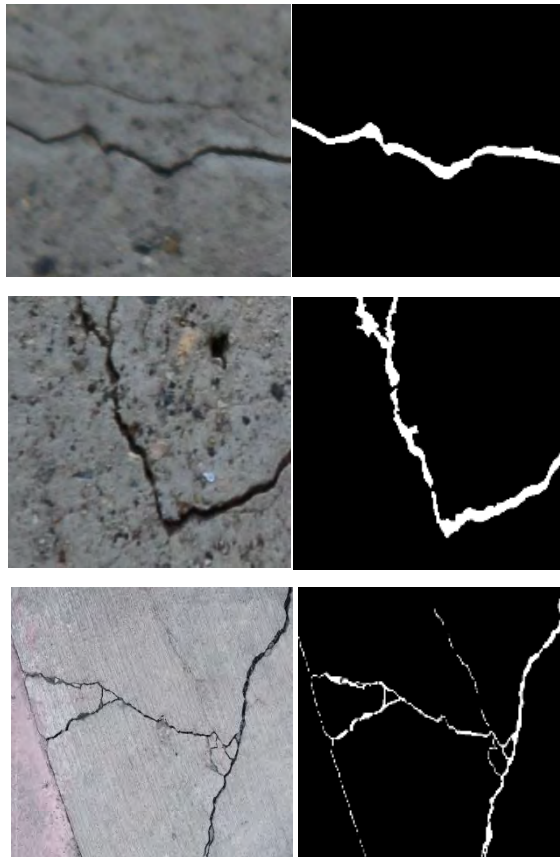
Figure 47: Architecture of Pix2pix; In the figure above, the generator G is given an image x and translates it into an output image G(x), the discriminator network D is given a pair of real and synthesized ground-truth/image pairs and outputs which image is real or fake. The results of the discriminator output are then used to update the weights of the generator.

Experimental Setup

Implementation: Experiment was implemented and performed using a Linux machine with a single GeForce GTX 1080 GPU and Intel CPU. Network architectures were implemented using Keras, a Python based deep learning API and basic image editing software was used to pre-process training and testing samples. Pavometrics Laser Crack Management System (LCMS) was used to annotate the dataset from the MTO.

Training Dataset: The training dataset was drawn from two primary sources as well as augmented data generated from the GAN-based approach.

Figure 48. Sample Training Image Pairs; top row contains images from DeepCrack dataset, bottom row contains images from MTO.



Real dataset: The first original dataset is the DeepCrack public benchmark dataset containing 300 unique image-mask pairs (Zou et al., 2018). The DeepCrack dataset contains images of a large variety of cracks over various surfaces (Figure 48 and 49). The second original dataset is a unique dataset acquired from the Ministry of Transportation Ontario that contained images of various stretches of highways across Ontario. Ground-truth cracks were annotated from the MTO dataset using the LCMS tool provided by the Ministry. The final total was 739 unique image-mask pairs.

Synthetic dataset: The aforementioned GAN-based augmentation was used to produce a much larger synthetic dataset. Training two networks on both of the real datasets, we were able to produce a much larger augmented DeepCrack dataset of 2300 image-mask pairs and 8220 image-mask pairs for an augmented MTO dataset. All images were pre-processed by being resized and cropped to each have dimensions of 256x256 and converted to the png file format. MTO dataset ground truths were also recoloured in order to be suitable for the binary segmentation task.

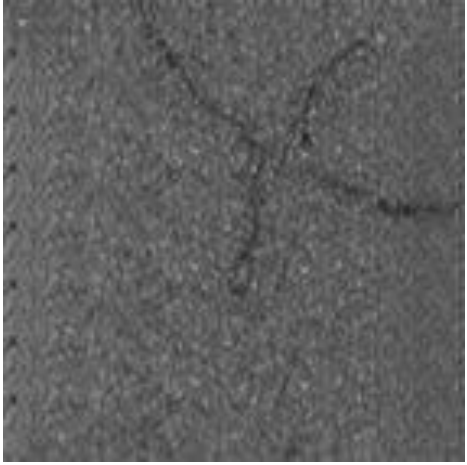
Synthetic Ground Truth	Synthetic Output
	
	

Figure 49: Synthetic Training Image Pairs

Testing Dataset: The testing dataset was similarly separated between the DeepCrack and MTO datasets. The DeepCrack dataset was already given a unique testing dataset of 237 images of similar composition and quality as the training set. The MTO dataset was partitioned into a testing dataset of 245 images before the remaining images were used as the training images. Similar to the training images, the testing set was also converted to png files and each was resized and cropped to 256x256.



Figure 50. Sample Testing Images

Evaluation: The training data sets as described above were each used to train the Pix2pix data augmentation network to produce similar synthetic data. This involved first using the ground truths from a data from a dataset to train Pix2pix into producing realistic ground truths for a given dataset and then training another instance of Pix2pix to translate these ground truths into realistic images based on those ground truths. The motivation for this in-depth augmentation process is to get more varied data than the typical simple image transformations. After augmentation, this created four datasets consisting of the DeepCrack benchmark and MTO dataset and their corresponding GAN generated synthetic data. U-Net was trained four separate times on each dataset at 500 epochs with 300 steps per epoch. Afterwards, each iteration of U-Net was tested and evaluated on either the DeepCrack or MTO dataset corresponding to which was the source of the data.

Evaluation Metric: One evaluation metric used for semantic segmentation tasks is the Dice Similarity Coefficient (DSC) proposed by Dice (1945). In a binary segmentation task, this

can be represented as the proportion of twice true positives divided by the sum of twice the true positives, the false positives, and the false negatives. Since it measures both the true positives and penalizes false positives and negatives, it acts as an improved metric for measuring precision.

$$Dice = \frac{2 \times TP}{(TP+FP)+(TP+FN)} \quad (7)$$

Experimental Results: Followings figures and table show the results of our crack detection results.

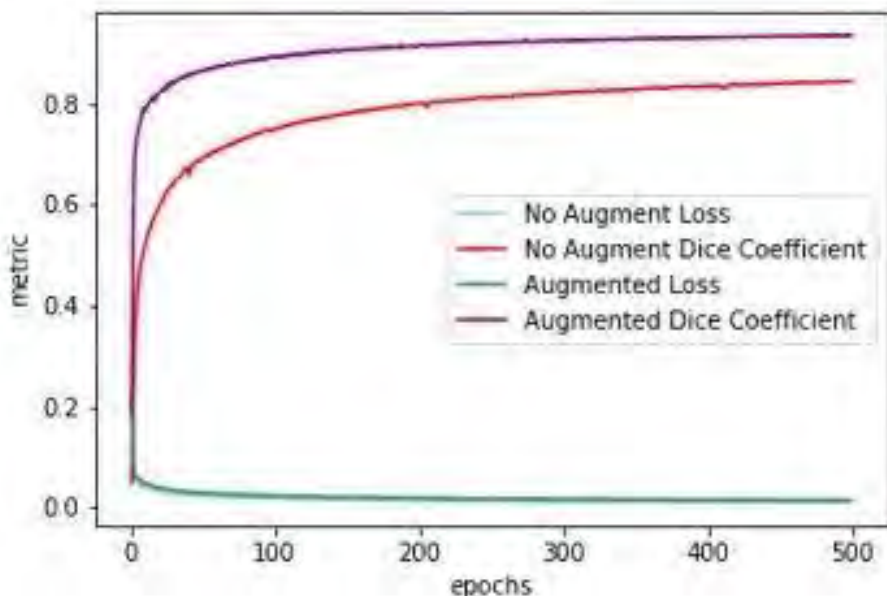


Figure 51. Metrics Over Epochs for Augmented vs. Non-Augmented DeepCrack

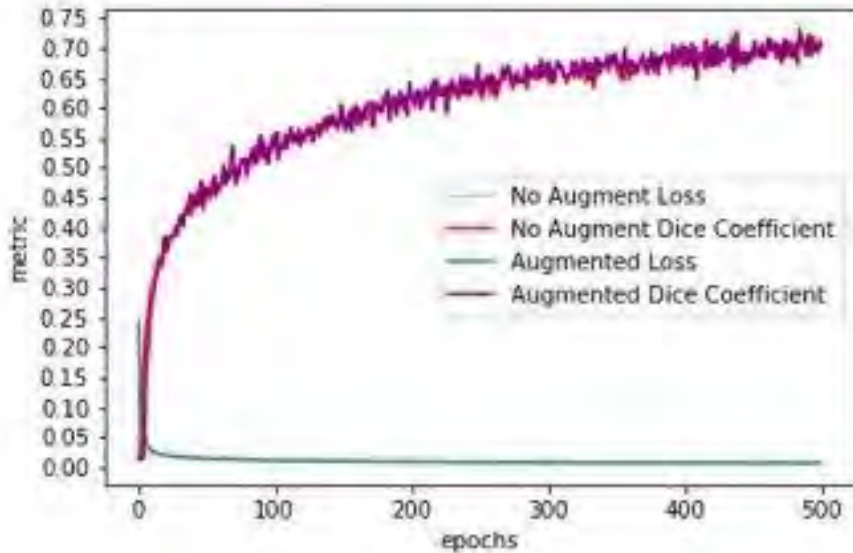


Figure 52. Metrics over Epochs for Augmented vs. Non-Augmented MTO Dataset

TABLE 11. SEMANTIC SEGMENTATION RESULTS

Dataset	Methods	Dice Score
DeepCrack dataset	U-Net	0.724
	U-Net with cGAN	0.882
MTO dataset	U-Net	0.704
	U-Net with cGAN	0.705

Through data augmentation via conditional generative networks, we can observe during the training phase with the DeepCrack dataset, a faster convergence towards the optimal dice coefficient score when using GAN augmented data as compared to the non-GAN augmented data. We find that the final evaluation accuracy is 15.8% higher when augmented as compared to without augmentation. Visualization of the segmentation results can be seen side-by-side in Figure 53.

In the MTO dataset, the overall patterns of training and evaluation are quite small although there appears to be a marginal increase in the accuracy and training convergence of the network using GAN augmented data. In summary, these suggest that augmentation through a GAN based approach improves the semantic segmentation results.

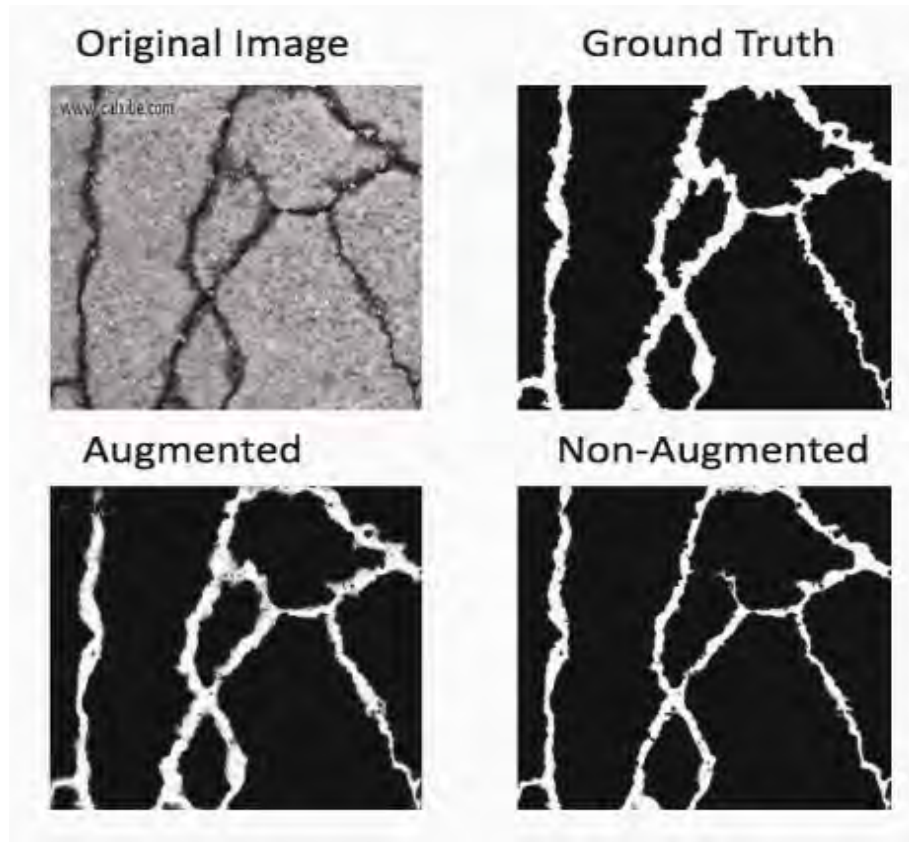


Figure 53: Sample Segmentation Results

Figure 54-56 shows the crack detection results that we produced with the proposed methods over MTO bridge data and semi-open tunnel data. Since we don't have reference labelled data, we were not able to quantitatively measure the performance of the proposed crack detection algorithm, but the results show the detection results qualitatively.



(a) Original imagery (Metal bridge in Niagara Falls)



(b) Crack detection results (Metal bridge in Niagara Falls)

Figure 54: Crack detection results with metal bridge in Niagara Falls



(a) Original imagery (Semi-open Tunnel in Oshawa)

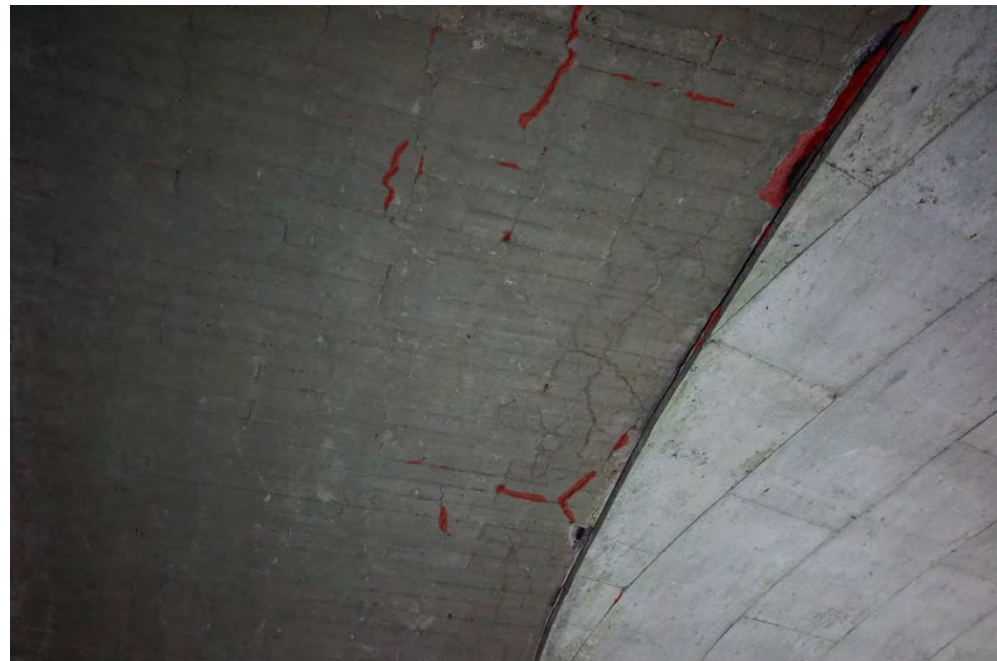


(b) Crack detection results (Semi-open Tunnel in Oshawa)

Figure 55: Crack detection results with semi-open tunnel in Oshawa



(a) Original imagery (Semi-open Tunnel in Oshawa)



(b) Crack detection results (Semi-open Tunnel in Oshawa)

Figure 56: Crack detection results with semi-open tunnel in Oshawa

Conclusions and Future Works

This report has studied the application of conditional generative adversarial networks as a potential route for data augmentation and a source of synthetic data. The experimental results are promising in showing improved performance in a semantic segmentation of cracks. Future experimentation can be done to tune the hyperparameters of the network where we can expect improved overall accuracy and training convergence. This project can also be expanded to include multi-class semantic segmentations. The data augmentation process may be even more useful there to reproduce samples of cracking patterns or severity that are relatively uncommon (e.g. spalling, delamination, etc.) Knowledge transfer may allow us to extend this project's result for other domains in infrastructure maintenance such as buildings or tunnels.

Conclusions and Recommendations

Aerial data collection is an effective way to obtain a better perspective and coverage over an area. Two low-cost UAV mapping platforms were tested as a cost- and time-effective alternative for the mapping and monitoring of highways and their assets. These mapping platforms were the DJI Phantom 2 Vision Plus with the FC200 RGB camera (4384x3288 pixels; nominal $f=5\text{mm}$), a normal/wide angle lens camera, and the DJI M100 with the HERO 5 Black camera (4000x3000 pixels; nominal $f=3\text{mm}$), a wide/super-wide angle lens camera.

UAV images over the UAV Range of the Markham Airport have been captured, where the runway and a taxiway were used to simulate highway environments. Images captured from two altitudes, 40m and 80m to test the effects of the image scale and to lead combined altitude solutions due to relatively flat terrain. To achieve engineering accuracies in the range of 2cm or better using low altitude remote sensing UAV mapping we observed that it is critical to:

- use metric cameras with wide angle lenses
- combine flight from different altitudes and/ or use cross flights
- use large forward and lateral overlaps, in the range of 80%,
- obtain accurate EO, that is incorporating accurate GCP or RTK GNSS, or apply SfM approach
- use check points
- use the rigorous simultaneous bundle adjustment solution with self-calibration

While the above characteristics result in a large number of images, they ensure a geometrically strong photogrammetric bundle network, higher accuracies and prevention of area coverage gaps. A large number of ground points was used to allow for various GCP and CHK points configurations, handling of the camera self-calibration and providing statistical validity of the results. The large number of images required significant processing time and computing capacity.

One of the main objectives of this work is to thoroughly examine the achievable mapping accuracies using UAV photogrammetric means with respect to the engineering accuracies of 2cm (vertical accuracy at 95% confidence interval) required by MTO. Regarding the accuracies obtained, certain photogrammetric network configurations have resulted in accuracies in the 2cm range, such as:

- a) the combination of 40m and 80m altitude images using the Phantom with the FC200, resulted in vertical errors in the range of 3cm for CHK points located on the pavement.
- b) flying from 40m altitude using M100 with the GoProHERO5 camera, results in vertical errors of about 2cm for CHK points located on the pavement.

We also observed that in several occasions the vertical accuracies are compatible to the planimetric accuracies. This is due to the wide angle lens used and the multi-view point geometry for determining the object point coordinates.

The accuracies obtained are affected by the accuracy of the estimation of the parameters of exterior orientation. In our case, where we used the indirect sensor orientation approach relying on the GCPs, the accuracy of GCPs plays significant role. The accuracy of the ground point using land surveying methods was in the range of 2cm. Unfortunately, the GNSS determined points, and especially their elevation did not appear to obtain this level of accuracies. That was due to the inexperience of the operators. Better accuracy of the GCPs, the use of RTK GNSS positioning of the UAV sensors and the use of better cameras (less distortions, better image quality) are expected to improve further the UAV photogrammetric results. Use of sufficient control (GCP or RTK GNSS) minimizes the block deformation which a typical problem when UAV images are used, especially when the block is not supported by well distributed GCPs. If there is a strong geometrically photogrammetric network, applying the SfM approach in the image space followed by a 3D similarity for the absolute orientation can also be another alternative.

In case where multiple flights are required with different camera and flight parameters, as this was the case in the confined space of the Oshawa bridge, a multi-block solution is recommended, where all the image sub-blocks can be integrated to one solution.

The complete and continuous coverage provided by the UAV images allows for the generation of dense Digital Surface Models in the form of point clouds. These points can be used for terrain /object surface generation and the generation of orthoimages, and therefore of image maps. At the Oshawa bridge case, it was demonstrated that the UAV images can result in the generation of a georeferenced 3D model of the geometric shape of the cement bridge tunnel in the forms of 3D point clouds and texture mapping representations. Products that can support engineering works on the bridge. Imagery also provides a complete and continuous temporal coverage and serves as excellent documentation method.

The quick launch of the mapping UAV mapping systems together with the rapid capture of low-altitude images and the availability of data processing application software result in significant time and cost saving compared to the field surveys and human visual inspections. UAV mapping systems can be deployed easily and do not require much mobilization. Obviously, we should not underestimate the role of well-trained operators - UAV pilots- and we must ensure that all safety regulations are met and followed at all times.

In this project, we demonstrated the Q-Drone system and UWB benchmark dataset for supporting UAV positioning research works. The Q-Drone system was designed for positioning a UAV platform using UWB sensors in various types of GNSS-denied environments including indoor, open field, close to buildings, underneath the bridge and semi-open tunnel. Through our intensive experiments, we demonstrated that Q-Drone system can position UAV systems with the accuracy of 74 cm MAE in xyz over the five diverse field datasets, 26 cm for bridge case while 1 meter for semi-open tunnel. These results were obtained only with UWB, not using GPS-guided positioning. This fact suggests potentials of adopting UWB-based positioning and navigation in GPS-denied environments. The results demonstrated were obtained by naïve filtering algorithms

without employing a sophisticated outlier filtering and stochastic positioning algorithms. We found a key negative factor affecting the positioning accuracy is mainly related to multi-path reflection of UAB signals in the semi-open tunnel environments. Therefore, as for our future works, we will focus on modeling statistical characteristics of multi-path signals from UWB sensors and implementing a machine learning algorithm for identifying and removing these outlier signals.

The experimental results are promising in showing improved performance in a semantic segmentation of cracks. Due to the lack of labeling data, our development and experiments are limited to train our deep neural convolutional network over the metal bridge and concrete tunnels. Our AI training was conducted only with the pavement crack data provided by MTO. As for our future research, it is required for developing a comprehensive computer vision tools for helping the MTO to label a range of anomalies with minimal laboring efforts. Preparing a large scale of labeling data is critical to adopt AI strategy in practices. Also, we identified that future experimentation can be done to tune the hyperparameters of the network where we can expect improved overall accuracy and training convergence. This project can also be expanded to include multi-class semantic segmentations. The data augmentation process may be even more useful there to reproduce samples of cracking patterns or severity that are relatively uncommon (e.g. spalling, delamination, etc.).

Acknowledgements

The contributions in the field works and data processing of the YorkU graduate students: Evangelos Bousias-Alexakis, Agata Szeremeta, Zahra Arjmandi, Athina Peidou, Ali Baligh Jahromi, Kunwoo Park, , Sowmya Natesan, Mahya Jodeiri-Rad, John Aggrey, Nacer Naciri, and Sudha Vana are very much appreciated. We wish also to express our special thanks to our post-doctoral fellow Dr. Jungwon Kang for providing all kinds of well-thought technical designs and solutions.

We also express our sincere thanks to Industrial SkyWorks (ISW) for providing UAV platforms and UAV pilots for the UAV surveys at the St Catharines and Oshawa bridges.

Bibliography

- Agisoft PhotoScan User Manual - Professional Edition, Version 1.4, n.d. 127.
- Ahmad, A., 2011. Digital Mapping Using Low Altitude UAV 19, 8.
- Armenakis C, 2017. Associate Editor, Chapter 4: Unmanned aerial systems for low-altitude remote sensing, Manual of Remote Sensing, 4th edition (MRS-4), American Society for Photogrammetry and Remote Sensing, (on-line access).
- Armenakis C, 2019. Chapter 1: Introduction, in Unmanned Vehicle Systems for Geomatics: Towards Robotic Mapping, Editors C Armenakis and P Patias, Whittles Publishing, 288p.
- Armenakis C, 2017. Chapter 4: Unmanned aerial systems for low-altitude remote sensing, Associate Editor, Manual of Remote Sensing, 4th edition (MRS-4), American Society for Photogrammetry and Remote Sensing (on-line access).
- Armenakis C, J Li-Chee-Ming, R A Persad (2019). Chapter 2: Fundamentals for UVS data collection and processing, in Unmanned Vehicle Systems for Geomatics: Towards Robotic Mapping, Editors C Armenakis and P Patias, Whittles Publishing, 288p.
- Armenakis C, P Patias, Editors (2019). Unmanned Vehicle Systems for Geomatics: Towards Robotic Mapping, Whittles Publishing, 288p.
- Astre H. (2018) SFMToolkit3. <http://www.visual-experiments.com/demos/sfmtoolkit/>
- Azmi, S.M., Ahmad, B., Ahmad, A., 2014. Accuracy assessment of topographic mapping using UAV image integrated with satellite images. IOP Conf. Ser.: Earth Environ. Sci. 18, 012015. <https://doi.org/10.1088/1755-1315/18/1/012015>
- Badrinarayanan, V., Kendall, A. and R. Cipolla, 2016. SegNet: A deep convolutional encoder-decoder architecture for image segmentation. arXiv: 1511/00561v3.
- Bay, H., T. Tuytelaars and L. Van Gool. 2006. SURF: Speeded up robust features. Computer vision–ECCV 2006. Springer, Berlin Heidelberg, pp. 404-417.
- N. Bolourian, M. Soltani, A. Albahria, and A. Hammad, "High level frame work for bridge inspection using lidar-equipped uav," in *Proceedings of the International Symposium on Automation and Robotics in Construction*, vol. 34, 2017, pp. 1-o.
- A. V. D. Bossche, R. Dalcé, N. Gonzalez and T. Val, "LocURa: A New Localisation and UWB-Based Ranging Testbed for the Internet of Things," in *International Conference on Indoor Positioning and Indoor Navigation (IPIN)*, Nantes, France, 2018.
- Bourquard, O., Mahony, R., Guenard, N., Chaumette, F., Hamel T., and L. Eck, 2009. "Image-based visual servo control of the translation kinematics of a quadrotor aerial vehicle," IEEE Transaction on Robotics, vol. 25, pp. 743-749.
- M. Chae, H.-s. Yoo, J. Kim and M. Cho, "Development of a wireless sensor network system for suspension bridge health monitoring," *Automation in Construction*, vol. 21, pp. 237-252, 2012.

- Chi, Y.-Y., Lee, Y.-F., Tsai, S.-E., 2016. Study on High Accuracy Topographic Mapping via UAV-based Images. IOP Conf. Ser.: Earth Environ. Sci. 44, 032006. <https://doi.org/10.1088/1755-1315/44/3/032006>
- W. Cui, C. Wu, W. Meng, B. Li, Y. Zhang and L. Xie, "Dynamic Multidimensional Scaling Algorithmfor 3-D Mobile Localization," *Ieee Transactions on Instrumentation and Measurement*, DECEMBER 2016.
- Daramola, O., Olaleye, J., Ajayi, O.G., Olawuni, O., 2017. Assessing the geometric accuracy of UAV-based orthophotos. SA J of Geomatics 6, 395. <https://doi.org/10.4314/sajg.v6i3.9>
- DataMapper, 2018. Professional drone based mapping and analytics, <https://www.datamapper.com/>
- DroneMapper 2018. Imagery processing, precision agriculture and GIS services. <https://dronomapper.com/>
- A. Duzgun, A.R. J.A. Rice, J.R. Martinez, I.R. Lasa, "Comparison of visual inspection and structural health monitoring as bridge condition assessment methods", J. Perform. Constr. Facil., 2016, 30(3): 04015049, 2016.
- Esri. (2018) Drone2Map for ArcGIS, <http://www.esri.com/products/drone2map>
- J. S. Esteves, A. Carvalho and C. Couto, "Generalized geometric triangulation algorithm for mobile robot absolute self-localization," in *IEEE International Symposium on Industrial Electronics*, 2003.
- Federal Communications (2004) "Fcc Amends Rules to Permit New Wideband Unlicensed Devices and Affirms Rules to Authorize The Deployment of Ultra-Wideband Technology," Commission.
- Forlani, G., Dall'Asta, E., Diotri, F., Cella, U.M. di, Roncella, R., Santise, M., 2018. Quality Assessment of DSMs Produced from UAV Flights Georeferenced with On-Board RTK Positioning. Remote Sensing 10, 311. <https://doi.org/10.3390/rs10020311>
- Fraser, R.H., I. Olthof, M. Maloley, R. Fernandes, C. Prevost, and J. van der Sluijs. (2015) UAV photogrammetry for mapping and monitoring of northern permafrost landscapes. UAV-g 2015 Int. Arch. Photogramm. Remote Sens. Spatial Inf. Sci., XL-1/W4, pp.361–361.
- Furukawa and Hernández, 2015. Multi-View Stereo: A Tutorial in Foundations and Trends in Computer Graphics and Vision. 9(1-2):1-148.
- Furukawa Y, Ponce J. 2010. Accurate, dense, and robust multi-view stereopsis. IEEE Trans Pattern Anal Mach Intell (PAMI) 32(8): 1362–1376.
- Gandor F., M. Rehak, J. Skaloud, 2015. Photogrammetric mission planner for RPAS. International Archives of the Photogrammetry, Remote Sensing and Spatial Information Sciences, UAV-g 2015, Volume XL-1/W4, 2015.
- Gerke, M., Przybilla, H.-J., 2016. Accuracy Analysis of Photogrammetric UAV Image Blocks: Influence of Onboard RTK-GNSS and Cross Flight Patterns. Photogrammetrie - Fernerkundung - Geoinformation 2016, 17–30. <https://doi.org/10.1127/pfg/2016/0284>
- Gindraux, S., Boesch, R., Farinotti, D., 2017. Accuracy Assessment of Digital Surface Models from Unmanned Aerial Vehicles' Imagery on Glaciers. Remote Sensing 9, 186. <https://doi.org/10.3390/rs9020186>.

- C. Gomez and H. Purdie , "UAV- based photogrammetry and geocomputing for hazards and disaster risk monitoring - a review," *Geoenvironmental Disasters*, vol. 3, no. 1, p. 23, 2016.
- M.A. Hassanain and R. E. Loov, "Cost optimization of concrete bridge infrastructure," *Canadian Journal of Civil Engineering*, vol. 30, no. 5, pp. 841-849, 2003.
- Hastedt H, T. Ekkela, T. Luhmanna, 2016. Evaluation of the quality of action cameras with wide-angle lenses in UAV photogrammetry, International Archives of the Photogrammetry, Remote Sensing and Spatial Information Sciences, Volume XLI-B1, XXIII ISPRS Congress.
- M. Heydariaan, H. Mohammadmoradi and O. Gnawali, "Toward Standard Non-line-of-sight Benchmarking of Ultra-wideband Radio-based Localization," in *IEEE Workshop on Benchmarking Cyber-Physical Networks and Systems (CPSBench)*, 2018.
- Hexagon Geospatial, 2018. GeoApp.UAS, <http://www.hexagongeospatial.com/brochure-pages/geoapp-uas>
- Hugenholtz C, O Brown, J Walker, T Barchyn, P Nesbit, M Kucharczyk, S Myshak, 2016. Spatial Accuracy of UAV-Derived Orthoimagery and Topography: Comparing Photogrammetric Models Processed with Direct Geo-Referencing and Ground Control Points, *J Geoinformatica*, 70:21-30.
- Joubert, N. Roberts, M. Truong, A., Berthouzoz, F. and P. Hanrahan, 2015. "An interactive tool for designing quadrotor camera shots," *ACM Transactions on Graphics*, 34, pp. 238:1-238:11.
- J. Kang, K. Park, Z. Arjmandi, G. Sohn, M. Shahbazi and P. Ménard, "Ultra-Wideband Aided UAV Positioning Using Incremental Smoothing with Ranges and Multilateration," in *IEEE/RSJ International Conference on Intelligent Robots and Systems (IROS)*, to be published, 2020.
- S. Kim, M. Spenko, S. Trujillo, B. Heyneman, D. Santos and M. R. Cutkosky, "Smooth Vertical Surface Climbing with Directional Adhesion," in *IEEE Transactions on Robotics*, 24(1), 65–74, 2008.
- Kucharczyk M, C H Hugenholtz, X Zou. 2018. UAV-LiDAR Accuracy in Vegetated Terrain, *Journal of Unmanned Vehicle Systems*, 6(4):212-234, <https://doi.org/10.1139/juvs-2017-0030>.
- A. Lederergerber and R. D'Andrea, "Ultra-Wideband Angle of Arrival Estimation Based on Angle-Dependent Antenna Transfer Function," MDPI, 2019a.
- A. Lederergerber and R. D'Andrea, "Dataset to Ultra-wideband angle of arrival estimation based on angle-dependent antenna transfer function," [Online]. Available: <http://hdl.handle.net/20.500.11850/366884>. [Accessed 14 October 2019b].
- Leitão, J P, M Moy de Vitry, A Scheidegger, J Rieckermann, 2016. Assessing the quality of digital elevation models obtained from mini unmanned aerial vehicles for overland flow modelling in urban areas. *Hydrol. Earth Syst. Sci.* 20, 1637–1653. <https://doi.org/10.5194/hess-20-1637-2016>
- J. Li, Y. Bi, K. Li, K. Wang, F. Lin and B. M. Chen, "Accurate 3D Localization for MAV Swarms by UWB and IMU Fusion," in *IEEE 14th International Conference on Control and Automation (ICCA)*, 2018.

- Li-Chee-Ming J, C Armenakis, 2014. Generation of dense 3D point clouds using a small quadcopter, *GEOMATICA*, 68(4):319-330.
- Li-Chee-Ming J., C. Armenakis, 2012. Introduction to a portable stereo-mapping system for unmanned vehicles, *GEOMATICA*, 66(4):181-193.
- Lourakis M. I. A,A. A. Argyros, 2009. SBA: A software package for generic sparse bundle adjustment. *ACM TOMS*, 36(1):1-30.
- Lowe, D.G. 2004. Distinctive Image Features from Scale-Invariant Keypoints. *International Journal of Computer Vision*, 60(2):91–110.
- K.K., Mermigas, “Evolution of Bridge Practices in Ontario, Canada.”, *Conference of the Transportation Association of Canada, Saskatoon, SK2018*.
- L. R. Newcome, *Unmanned aviation: a brief history of unmanned aerial vehicles*. American Institute of Aeronautics and Astronautics, 2004.
- R. Montero, J. Yictores, S. Martinez, A. Jard6n, and C. Balaguer, "Past, present and future of robotic tunnel inspection," *Automation in Construction*, vol. 59, pp. 99-112, 2015.
- J. J. More, "The Levenberg-Marquardt Algorithm: Implementation and Theory," in *Conference on Numerical Analysis University of Dundee*, Scotland, 1977.
- Morel J-M, G Yu, 2009. ASIFT: Anew framework for fully affine invariant image comparison. SIAM, 2(2), <https://doi.org/10.1137/080732730>.
- M. W. Mueller, M. Hamer and a. D'Andrea, "Fusing ultra-wideband range measurements with accelerometers and rate gyroscopes for quadrocopter state estimation," in *IEEE International Conference on Robotics and Automation* , 2015.
- Nielsen M Ø 2004. True orthophoto generation. Master Thesis, Informatics and Mathematical Modelling, Technical University of Denmark, 126p.
- J.-K. Oh, G. Jang, S. Oh, J. H. Lee, B.-J. Yi, Y. S. Moon, J. S. Lee, and Y. Choi, "Bridge inspection robot system with machine vision," *Automation in Construction*, vol. 18, no. 7, pp. 929-941, 2009.
- K. Park, J. Kang, Z. Arjmandi, M. Shahbazi and G. Sohn, "Multilateration Under Flip Ambiguity For Uav Positioning Using Ultrawide-Band," in *International Society for Photogrammetry and Remote Sensing*, to be published, 2020.
- Peppa, M.V., Mills, J.P., Moore, P., Miller, P.E., Chambers, J.E., 2016. Accuracy assessment of a uav-based landslide monitoring system. *Int. Arch. Photogramm. Remote Sens. Spatial Inf. Sci.* XLI-B5, 895–902. <https://doi.org/10.5194/isprsarchives-XLI-B5-895-2016>
- Persad AR, C Armenakis, 2017. Comparison of 2D and 3D approaches for the alignment of UAV and lidar point clouds. *UAV-g 2017 Conference*, Bonn, ISPRS Archives, Vol XLII-2/W6, 275-279, <https://doi.org/10.5194/isprs-archives-XLII-2-W6-275-2017>
- Photosynth, 2016. Capturing and viewing the world in 3D, <https://photosynth.net/about.aspx>
- Pierrot-Deseilligny M, Clery I., 2011. APERO, an Open Source Bundle Adjustment Software for Automatic Calibration and Orientation of Set of Images. *Int. Arch. Photogramm. Remote Sens. Spatial Inf. Sci.*, 38 (5/W16).

- Pierrot-Deseilligny M, Paparoditis N. 2006. A multiresolution and optimization-based image matching approach: an application to surface reconstruction from SPOT5-HRS stereo imagery. *Int. Arch. Photogramm. Remote Sens. Spatial Inf. Sci.*, 36 (1/W41).
- Puri A. 2004. A survey of unmanned aerial vehicles (UAV) for traffic surveillance. Technical Report, Dept. of Computer Science & Engineering, University of South Florida.
- RECAP 360 (2018) ReCap 360 reality capture and 3D scanning software. <http://www.autodesk.com/products/recap-360/overview>.
- Ridolfi E, G Buffi, S Venturi, P Manciola, 2017. Accuracy Analysis of a Dam Model from Drone Surveys. *Sensors* 17, 1777. <https://doi.org/10.3390/s17081777>
- M. Ridolfi, S. Vandermeeren, J. Defraye , H. Steendam, J. Gerlo, D. De Clercq, J. Hoebeka and E. De Poorter , "Experimental Evaluation of UWB Indoor Positioning for Sport Postures," *MDPI*, 2018.
- Rothermel, M., K. Wenzel, D. Fritsch and N. Haala. 2012. SURE: Photogrammetric surface reconstruction from imagery. Proceedings LC3D Workshop. Berlin.
- Roze, A., Zufferey, J.-C., Beyeler, A., and McClellan, A (2014) eBee RTK Accuracy Assessment, Lausanne, Switzerland, 7 pp.
- Sa, I. and Ian Corke, P. (2014) "Vertical Infrastructure Inspection Using a Quadcopter and Shared Autonomy Control," in *Field and Service Robotics*, 219-232, 2014.
- R. Salvini, S. Riccucci, D. Gum, R. Giovannini , C. Vanneschi, and M. Francioni, " Geological application of uav photogrammetry and terrestrial laser scanning in marble quarrying (apuan alps, italy)," in *Engineering Geology for Society and Territory-Volume 5*. Springer, 2015, pp. 979-983.
- Shahbazi M, G Sohn, J Théau, P Menard, 2015. Development and Evaluation of a UAV-Photogrammetry System for Precise 3D Environmental Modeling, *Sensors* 2015, 15(11), 27493-27524; <https://doi.org/10.3390/s151127493>
- Y. Shen and M. Z. Win, "Effect of Path-Overlap on Localization Accuracy in Dense Multipath Environments," in *IEEE International Conference on Communications*, Beijing, China, 2008.
- SimActive, 2018. Correlator3D UAV, <http://www.simactive.com/en/correlator3d-uav/drone-photogrammetry-software/features>.
- Snavely N, Seitz SM, Szeliski R, 2008. Modeling the world from Internet photo collections. *International Journal of Computer Vision* 80(2):189–210.
- Strecha, C. A. Bronstein, M. Bronstein and P. Fua, 2012. LDAHash: Improved matching with smaller descriptors. *IEEE Trans. Pattern Anal. Mach. Intell.* (34):66–78
- Tiemann, J. Schweikowski, F. and C., Wietfeld, 2015. "Design of an UWB indoor-positioning system for UAV navigation in GNSS-denied environments," in *IEEE International Conference on Indoor Positioning and Indoor Navigation (IPIN)*, pp. 1-7.
- Tien Bui, D., Long, N.Q., Bui, X.-N., Nguyen, V.-N., Van Pham, C., Van Le, C., Ngo, P.-T.T., Bui, D.T., Kristoffersen, B., 2018. Lightweight Unmanned Aerial Vehicle and Structure-from-Motion Photogrammetry for Generating Digital Surface Model for Open-Pit Coal Mine Area and Its Accuracy Assessment, in: Tien Bui, D., Ngoc Do, A., Bui, H.-B., Hoang, N.-D. (Eds.), *Advances and Applications in Geospatial Technology and*

- Earth Resources. Springer International Publishing, Cham, pp. 17–33. https://doi.org/10.1007/978-3-319-68240-2_2.
- A. V. Uvarov, A. Uvarov and M. Y. Gerasimov, "On the Fundamental Limitations of Ultra-Wideband Antennas," *Journal of Communications Technology and Electronics*, 2019.
- Vautherin J, S Rutishauser, K Schneider-Zapp, H F Choi, Ve Chovancova, A Glass, C Strecha, 2016. Photogrammetric accuracy and modeling of rolling shutter cameras, ISPRS Annals of the Photogrammetry, Remote Sensing and Spatial Information Sciences, Volume III-3, XXIII ISPRS Congress.
- Wierzbicki D, Nienaltowski, 2019. Accuracy Analysis of a 3D Model of Excavation, Created from Images Acquired with an Action Camera from Low Altitudes, ISPRS International Journal of Geo-Information, 8(83); doi:10.3390/ijgi8020083.
- Wu C. 2018. VisualSfM: A Visual Structure from Motion System, <http://www.cs.washington.edu/homes/ccwu/vsfm/>
- S.-N. Yu, J.-H. Jang, and C.-S. Han, "Auto inspection system using a mobile robot for detecting concrete cracks in a tunnel," *Automation in Construction*, vol. 16 , no. 3, pp. 255-261, 2007.
- S. Zahran, M. M. Mostafa, A. Masiero, A. M. Moussa, A. Vettore and N. El-Sheimy, "Micro-Radar And Uwb Aided Uav Navigation In Gnss Denied Environment," in *International Society for Photogrammetry and Remote Sensing*, 2018.
- W. Zhao, A. Goudar, J. Panerati and A. P. Schoellig, "Learning-based Bias Correction for Ultra-wideband Localization of Resource-constrained Mobile Robots," 2020. [Online]. Available: <https://arxiv.org/abs/2003.09371>.
- Y. Zhou, J. Li and L. Lamont , "Multilateration localization in the presence of anchor location uncertainties," in *Global Communications Conference (GLOBECOM)*, Anaheim, CA, USA , 2012.
- N. Greening and R. Landgren, *Sulfate discoloration of concrete flatwork*. Portland Cement Association, Research and Development Laboratories, 1966, no. 203.
- Z. Fan, Y. Wu, J. Lu, and W. Li, "Automatic pavement crack detection based on structured prediction with the convolutional neural network," *arXiv preprint arXiv:1802.02208*, 2018.
- F. Ozgenel, "Concrete crack segmentation dataset," 2019. [Online]. Available: <https://data.mendeley.com/datasets/jwsn7tfbrp/1>
- Y. Shi, L. Cui, Z. Qi, F. Meng, and Z. Chen, "Automatic road crack detection using random structured forests," *IEEE Transactions on Intelligent Transportation Systems*, vol. 17, no. 12, pp. 3434- 3445, 2016.
- S. Chambon and J.-M. Moliard , "Automatic road pavement assessment with image processing : review and comparison," *International Journal of Geophysics*, vol. 2011, 2011.
- S. Liu, J. Zhang, Y. Chen, Y. Liu, Z. Qin, and T. Wan, "Pixel level data augmentation for semantic image segmentation using generative adversarial networks," in *ICASSP 2019-2019 IEEE International Conference on Acoustics, Speech and Signal Processing (ICASSP)* . IEEE, 2019, pp. 1902-1906.

- A. Krizhevsky, I. Sutskever, and G. E. Hinton, " Imagenet classification with deep convolutional neural networks," in *Advances in neural information processing system s*, 2012, pp. 1097-1105.
- D. C. Cirean, U. Meier, J. Masci, L. M. Gambardella, and J. Schmidhuber," High-performance neural networks for visual object classification," *arXiv preprint arXiv:1102.0183*, 2011.
- P. Y. Simard, D. Steinkraus, J. C. Platt *et al.*, "Best practices for convolutional neural ne tworks applied to visual document analysis." in ICDAR, vol. 3, no . 2003, 2003.
- M. D. Zeiler and R. Fergus , " Visualizing and understanding convolutional ne tworks," in *European conference on computer vision*. Springer, 2014, pp. 818-833.
- H. Noh, S. Hong, and B. Han, " Learning deconvolution network for semantic segmentation," in *Plvceedings of the IEEE International Conference on computer vision*, 2015, pp. 1520- 1528.
- R. Wu, S. Yan, Y. Shan , Q. Dang , and G. Sun, " Deep image : Scaling up image recognition," *arXiv preprint arXiv:1501.02876*, 2015.
- Y.-J. Cha, W. Choi, and O. Biiyiikiztiirk , "Deep learning-based crack damage detection using convolutional neural networks ," *Computer- Aided Civil and Infrastructure Engineering*, vol. 32, no. 5, pp. 361- 378, 2017.
- B. Kim and S. Cho, "Automated vision- based detection of cracks on concrete surfaces using a deep learning technique," *Sensors*, vol. 18, no. 10, p. 3452, 2018.
- M. Thoma, "A survey of semantic segmentation". *arXiv preprint arXiv:1602.06541*, 2016.
- M. R. Jahanshahi and S. F. Masri, "A new methodology for non- contact accurate crack width measurement through photogrammetry for automated structural safety evaluation," *Smart materials and structures*, vol. 22, no. 3, p. 035019, 2013.
- M. R. Jahanshahi, S. F. Masri, C. W. Padgett, and G. S. Sukhatme, "An innovative methodology for detection and quantification of cracks through incorporation of depth perception," *Machine vision and application s*, vol. 24, no. 2, pp. 227-241, 2013.
- B. Shan, S. Zheng , and J. Ou, "A stereovision-based crack width detection approach for concrete surface assessment," *KSCE Journal of Civil Engineering*, vol. 20, no. 2, pp. 803-812, 2016 .
- Y. Fan, Q. Zhao, S. Ni, T. Rui , S. Ma, and N. Pang, "Crack detection based on the mesoscale geometric features for visual concrete bridge inspection," *Journal of Electronic Imaging*, vol. 27, no. 5, p. 053011, 2018.
- V. Hoskere, Y. Narazaki, T. Hoang, and B. Spencer Jr, " Vision-based structural inspection using multiscale deep convolutional neural networks," *arXiv preprilll arXiv:1805.01055*, 2018.
- D. Lee, J. Kim, and D. Lee, "Robust concrete crack detection using deep learning-based semantic segmentation," *International Journal of Aeronautical and Space Sciences*, vol. 20, no. I, pp. 287-299, 2019.
- Z. Fan, Y. Wu, J. Lu, and W. Li, "Automatic pavement crack detection based on structured prediction with the convolutional neural network," *arXiv preprint arXiv:1802.02208*, 2018.

- P. Liskowski and K. Krawiec, "Segmenting retinal blood vessels with deep neural networks," *IEEE transactions on medical imaging*, vol. 35, no. 11, pp. 2369-2380, 2016.
- I. Goodfellow, et al. "Generative adversarial nets." *Advances in neural information processing systems*. 2014.
- S. Liu, J. Zhang, Y. Chen, Y. Liu, Z. Qin, and T. Wan, "Pixel level data augmentation for semantic image segmentation using generative adversarial networks," in *ICASSP 2019-2019 IEEE International Conference on Acoustics, Speech and Signal Processing (ICASSP)*. IEEE, 2019, pp. 1902-1906.
- J. Wang and L. Perez, "The effectiveness of data augmentation in image classification using deep learning," *Convolutional Neural Networks Vis. Recognit.*, 2017.
- T. Iqbal and H. Ali, "Generative adversarial network for medical images," *Journal of medical systems*, vol. 42, no. 11, p. 231, 2018.
- T. Neff, C. Payer, D. Stern, and M. Urschler, "Generative adversarial network based synthesis for supervised medical image segmentation," in *Pmc. OAGM and ARW Joint Workshop*, 2017.
- C. Bowles, L. Chen, R. Guerrero, P. Bentley, R. Gunn, A. Hammers, D. A. Dickie, M. V. Hernandez, J. Wardlaw, and D. Rueckert, "Ganaugmentation: augmenting training data using generative adversarial networks," *arXiv preprint arXiv:1810.10863*, 2018.
- C. Tan, et al. "A survey on deep transfer learning." *International conference on artificial neural networks*. Springer, Cham, 2018.
- O. Ronneberger, P. Fischer, and T. Brox. "U-net: Convolutional networks for biomedical image segmentation." *International Conference on Medical image computing and computer-assisted intervention*. Springer, Cham, 2015.
- P. Isola, et al. "Image-to-image translation with conditional adversarial networks." *Proceedings of the IEEE conference on computer vision and pattern recognition*. 2017.
- Q. Zou, et al. "Deepcrack: Learning hierarchical convolutional features for crack detection." *IEEE Transactions on Image Processing* 28.3 (2018): 1498-1512.
- L.R. Dice. "Measures of the amount of ecologic association between species." *Ecology*. 1945;26:297–302, 1945.

Appendix A: Markham Ground Survey

GROUND COORDINATES DETERMINATION USING LAND SURVEYING

In the Markham survey area, 44 points were surveyed using GNSS methods, while a total of 47 points were surveyed using a total station. For the ground surveying task a TS11 Leica Total Station has been used. In all three locations a small number of points has been selected to be used as set-up/station points. A traverse of 4 points was set for the total station survey. This was between points S1, 210, S3, and 208. Initially, it was desired to have a network of 5 points (including station S2). However, due to observations errors to and from this station, it was omitted and disregarded from further observations.

When a single point was observed multiple times throughout the traverse (that is, from different setups), the point's computed coordinates were averaged. Upon further investigation, it was found that points 7, 8, 10, 12, 15, and S2 (each observed from at least two traverse stations) had multiple computed coordinates that differed by over approximately 5cm from each other. The provided transformed coordinates for these points are based on their average position however, these points may need to be omitted from final aerial survey processing, as it is unclear which observation (and final coordinate) is correct. As point S2 was initially a traverse station but was classified as incorrect, all observations taken from that station (point 202 and 204) were disregarded, as it was assumed their coordinates would also be incorrect). Point 204 was only surveyed using the total station, as it could not be located at the time of the GNSS survey. Thus, in end, only 45 points were observed using the total station.

The station points have been solved in all cases in a local coordinate system as a network with the minimum number of constraints, without taking into account the coordinates derived from the GPS observations. The rest of the points have been measured from multiple stations and their coordinates have been averaged.

LAND SURVEY NETWORK ADJUSTMENT

To perform the network adjustment and determine the coordinates of the 4 control points, a total of 23 observations were used – 7 directional angles, 8 zenith angles, and 8 slope distances. The system had 12 degrees of freedom, with a total of 12 unknowns (the XYZ of each of the S1, 210, and S3 control points). It was assumed that the coordinates of point 208 were fixed at (1000, 1000, 1000) m. To perform traverse network adjustments, GNU Gamma (an open-source adjustment software) was used. In each survey region case, a solution was determined in local coordinates. Then, applying tachymetric techniques, the local coordinates of the remaining survey points were determined. Once the locally defined

coordinates of each network's points were determined, a transformation was performed to bring the network to the desired coordinate system (discussed in the Coordinate Conversion report).

Solving the network at a confidence level of 95% resulted in the following local coordinates for the remaining control points.

Table A-1: Results of Markham (Local) Traverse Network

Point	Coordinate Component	Approximate Value (m)	Adjusted Value (m)	Standard Deviation (mm)
208	X	1000.000	1000.000	0.0
	Y	1000.000	1000.000	0.0
	Z	1000.000	1000.000	0.0
210	X	1000.00000	1000.00000	0.0
	Y	1254.62100	1254.62468	3.8
	Z	997.72400	997.85863	5.4
S1	X	943.86176	943.86161	4.6
	Y	1254.90354	1254.90947	5.2
	Z	997.76812	997.90148	5.8
S3	X	978.39868	978.40122	3.7
	Y	1143.33370	1143.33397	3.8
	Z	998.71518	998.85110	4.7

Approximate values were determined based on the observations performed to construct the network. The mean errors and parameters of the error ellipses of the remaining control were determined as follows.

Table A-2: Mean Errors and Parameters of the Error Ellipses of Markham (Local) Traverse Network

Point	mp (mm)	mxy (mm)	Mean Error Ellipse			Confidence Error Ellipse		g
			a (mm)	b	Alpha (gons)	a' (mm)	b'	
210	2.8	2.7	3.8	0.0	100.0	10.5	0.0	0.0
S1	6.9	4.9	5.2	4.6	99.5	14.4	12.8	0.0
S3	5.3	3.8	3.8	3.7	134.3	10.7	10.3	0.0

LEVELLING SURVEY

The determined CGVD28 HT2_2010v70 system orthometric heights (from the coordinate conversion process) of the GNSS surveyed points were used to transfer elevation to the

remaining observed points through either differential levelling or trigonometric levelling techniques.

In the Markham survey area, spirit levelling was performed in two loops between the points outlined below. The first was conducted in a single-run manner, while the second in a double-run.

Table A-3: Points in Markham Survey Area Level Loop

Loop 1 Levelled Points	Loop 2 Levelled Points
S1	S3
201	206
210	207
205	208
206	209
S3	212
S2	211
203	-
202	-

The GNSS-based orthometric elevation of S1 was propagated through to the remaining loop points, as per standard differential levelling techniques (that is, height differencing and adjustment). The determined height of point S3 found in loop 1 was then treated as the fixed elevation in loop 2 differential levelling was applied again. In both cases, adjustments to the raw determined heights were applied based on the number of setups in the levelling loops.

Having orthometric heights for all points of the traverse (S1, 210, 208, S3), remaining orthometric heights of surveyed points were determined by applying trigonometric levelling techniques on the total station survey data. The previously determined orthometric heights at the traverse station points were used as the instrument setup elevations in the remaining levelling calculation process.

As GNSS data was collected for most surveyed points, the total station derived and GNSS orthometric heights were compared. Unfortunately, a random discrepancy appears between the two determined heights. The cause of this is unclear.

GROUND COORDINATES DETERMINATION USING GNSS

DATA COLLECTION

GNSS surveying of the positions of these targets was performed using post-processed relative positioning. To do so, the Leica GS15 receivers have been used.

First, stakeout of the GCPs was performed. Approximate positions of the GCPs were already pre-determined and so the stakeout function in the Leica receivers were used to place the targets in their pre-determined spots. To do so, the GCP coordinates were converted to the right format before inputting them into the Leica receivers. The latter then gives directions that lead to the spot where the GCP should be placed. This was repeated until all GCPs were placed around the highway.

For the surveying part, one of the receivers has been set up as a base station (target “S1”) which was left running for the whole duration of the data collection.



FigureA-1 - Leica CS15 used for the GNSS surveying

All the receivers were set up on tribrachs and tripods which were levelled and centered so that they point at the center of the targets. Because of the limited number of receivers that were available for the data collection, the surveying of the targets wasn't done simultaneously. For each receiver, it was placed on a target, levelled and centered, and the data collection was initiated. The collection was done for at least 10 minutes before stopping it and storing the logged data. The height of the antenna (from the GCP) was recorded separately using a measuring tape before moving the receiver, antenna, tribrach and tripod to a new GCP. This procedure has been followed for all GCPs except for point P204 which couldn't be located on the field.

DATA PROCESSING PROCEDURE

The data was extracted from the Leica receivers using USBs and sorted into a computer (Fig.A-2). A first check was done to make sure that all the points have been extracted properly and that they are properly named for the processing. Once that was done, all the points were imported into the Leica Infinity software. Point “S1” was set up as a base station in the software while the rest of the points were set up as rovers. The RTK solution was then initiated and reports for each of the files were generated by the software.

The next step was to extract the final positions from the reports as well as other relevant information, compute the 2D and 3D standard deviations and put everything together into one document.

COORDINATE SYSTEMS AND TRANSFORMATIONS

The coordinates found through the GNSS surveys of each site were converted from the WGS84 coordinate system to NAD83(CRS)v6 2010 MTM Zone 10 system using Natural Resources Canada’s TRX tool. As suggested by NRCan, WGS84 was considered equivalent to the ITRF2008 reference system. When inputting the surveyed latitude, longitude and ellipsoid height values, the ITRF2008 system at epoch 2010-01-01 was used. The orthometric heights at such points were converted from GNSS derived ellipsoid height using Natural Resources Canada’s GPS-H tool. The previously derived NAD83(CRS) MTM Zone 10 coordinates were used as input. The vertical datum was selected to be CGVD28, while the geoid model as HT2_2010v70.

Next, having easting and northing coordinates of the survey area’s GNSS points in the NAD83(CRS) MTM Zone 10 systems, it was necessary to convert the coordinates of the total station (TS) points, previously found in the arbitrarily defined local system. Matlab generated software was used to determine the rotation and shift transformation parameters that converted the local coordinates to easting and northing of the NAD83(CRS) MTM Zone 10 coordinate system. The scale factor of such transformations was kept constant at 1.0 for each survey area case. In cases where multiple local coordinates were found (due to redundant observations of a point), the coordinates were averaged prior to being transformed to the desired system.

Coordinates

	Reference - BASERIGHT2 Rover - P01		Reference - BASERIGHT2	Rover - P01
Point Role:	Navigated RTK	Fixed PP		
WGS84 Latitude:	43° 56' 03.39" N	43° 56' 06.67" N	Easting:	-
WGS84 Longitude:	79° 16' 01.04" W	79° 16' 02.01" W	Northings:	-
WGS84 Ellip. Height:	196.9978 m	196.8435 m	Ortho. Height:	-
WGS84 Cartesian X:	856,801.3664 m	856,767.0186 m		
WGS84 Cartesian Y:	-4,520,201.7313 m	-4,520,136.5847 m		
WGS84 Cartesian Z:	4,402,972.1086 m	4,403,044.9575 m		
Baseline Vector and Quality - WGS84				
ΔLatitude:	0° 00' 03.28"	SD ΔLatitude:	0.0001 m	
ΔLongitude:	-0° 00' 00.97"	SD ΔLongitude:	0.0001 m	
ΔHeight:	-0.1543 m	SD ΔHeight:	0.0002 m	
ΔX:	-34.3478 m	SD ΔX:	0.0001 m	
ΔY:	65.1466 m	SD ΔY:	0.0001 m	
ΔZ:	72.8489 m	SD ΔZ:	0.0001 m	
Slope Dist.:	103.5896 m	SD Slope Dist.:	0.0001 m	
M0:	0.2771 m	CQ 1D:	0.0002 m	
Q11:	0.00000007	CQ 2D:	0.0001 m	
Q12:	-0.00000005	CQ 3D:	0.0002 m	
Q22:	0.00000024			
Q13:	0.00000002			
Q23:	-0.00000015			
Q33:	0.00000029			
Frequency:	L1/L2	GDOP:	2.2 - 2.3	GPS SVs: 8/8
Solution Optimisation:	None	PDOP:	1.9 - 2.0	GLONASS SVs: -
Solution Type:	Phase Fixed	HDOP:	0.9 - 1.0	Beidou SVs: -
		VDOP:	1.7 - 1.8	Galileo SVs: -
				QZSS SVs: -
Ephemeris Type:				
GPS	Broadcast			

Figure A-2: Example of extracted output of the Leica Infinity processing

Table A-4: Notable Points in Markham Area Survey

GNSS Surveyed Points	Total Station Traverse Points
S1	S1
210	210
208	208
S3	S3

To perform the transformation, the local coordinates of the traverse points were shifted from 210_Local to 210_GNSS and rotated by the difference in azimuths of the lines 210_Local to 208_Local and 210_GNSS to 208_GNSS.

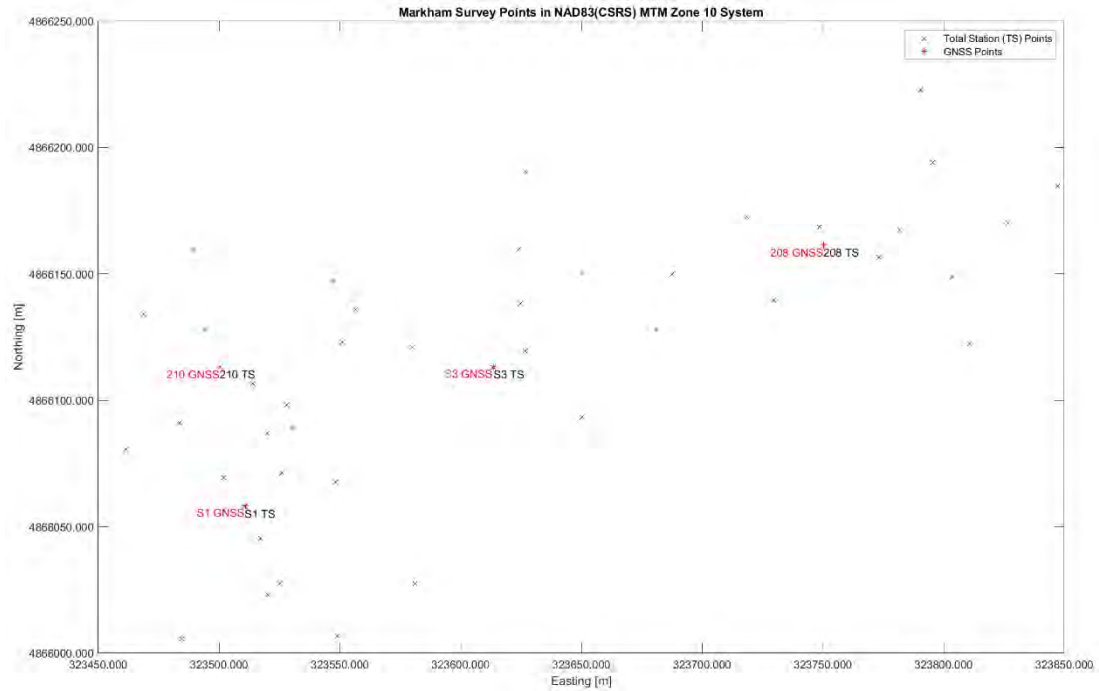


Figure A-3: Transformed Markham Area Total Station Coordinates Compared Against GNSS Measured Points

Table A-5: Markham Area Point Coordinates Based on GNSS Survey

Point	WGS84			NAD83(CSRS) MTM Zone 10			
	Latitude (North)	Longitude (West)	Ellipsoid Height [m]	Easting [m]	Northing [m]	Ellipsoid Height [m]	Orthometric Height [m]
P1	43°56'06.67"	79°16'02.01"	196.8435	323488.946	4866159.460	197.958	234.144
P2	43°56'05.84"	79°16'02.92"	196.5749	323468.724	4866133.788	197.689	233.876
P3	43°56'04.46"	79°16'02.25"	196.6012	323483.786	4866091.241	197.716	233.903
P4	43°56'04.11"	79°16'03.24"	196.0632	323461.738	4866080.378	197.178	233.366
P5	43°56'01.68"	79°16' 02.17	196.4476	323485.812	4866005.453	197.563	233.751
P6	43°56'05.66"	79°16'01.77"	196.8688	323494.387	4866128.305	197.984	234.171
P7	43°56'04.97"	79°16'00.89"	191.542	323514.072	4866107.066	192.657	228.844
P8	43°56'04.69"	79°16'00.26"	197.4989	323528.147	4866098.465	198.614	234.801
P9	43°56'03.82"	79°16'00.33"	196.7826	323526.661	4866071.611	197.898	234.085
P10	43°56'03.75"	79°16'01.42"	196.4492	323502.358	4866069.382	197.564	233.751
P11	43°56'02.97"	79°16'00.72"	197.0543	323518.038	4866045.355	198.169	234.357
P12	43°56'02.40"	79°16'00.36"	196.6702	323526.116	4866027.787	197.785	233.973
P13	43°56'01.73"	79°15'59.29"	197.0969	323550.038	4866007.177	198.212	234.4
P14	43°56'03.70"	79°15'59.34"	197.5923	323548.751	4866067.970	198.707	234.894
P15	43°56'02.39"	79°15'57.86"	197.4727	323581.872	4866027.636	198.588	234.775
P16	43°56'05.90"	79°15'58.99"	197.8607	323556.364	4866135.887	198.976	235.162
P17	43°56'06.27"	79°15'59.41"	197.2235	323546.965	4866147.279	198.339	234.525

P18	43°56'05.42"	79°15'57.93"	197.9065	323580.046	4866121.140	199.021	235.207
P19	43°56'07.67"	79°15'55.83"	197.5817	323626.682	4866190.711	198.697	234.882
P20	43°56'06.66"	79°15'55.96"	198.0433	323623.871	4866159.533	199.158	235.343
P21	43°56'05.37"	79°15'55.83"	198.5086	323626.884	4866119.730	199.624	235.81
P22	43°56'04.52"	79°15'54.78"	198.2097	323650.375	4866093.565	199.325	235.511
P23	43°56'06.37"	79°15'54.77"	198.3927	323650.436	4866150.658	199.508	235.693
P24	43°56'06.00"	79°15'53.47"	198.5552	323679.460	4866139.322	199.67	235.855
P25	43°56'07.08"	79°15'51.71"	198.7383	323718.616	4866172.764	199.853	236.038
P26	43°56'06.01"	79°15'51.22"	198.7401	323729.638	4866139.774	199.855	236.04
P27	43°56'06.55"	79°15'49.27"	199.3412	323773.078	4866156.563	200.456	236.641
P28	43°56'08.70"	79°15'48.48"	199.8521	323790.506	4866222.965	200.967	237.151
P29	43°56'07.77"	79°15'48.26"	199.5523	323795.495	4866194.278	200.667	236.851
P30	43°56'06.31"	79°15'47.90"	199.3474	323803.652	4866149.244	200.462	236.647
P31	43°56'05.44"	79°15'47.58"	199.5162	323810.866	4866122.415	200.631	236.816
P32	43°56'06.95"	79°15'50.36"	198.9612	323748.734	4866168.838	200.076	236.261
P201	43°56'04.32"	79°16'00.62"	197.5931	323520.150	4866087.023	198.708	234.895
P202	43°56'01.92"	79°16'01.20"	196.3626	323507.424	4866012.920	197.478	233.666
P203	43°56'02.26"	79°16'00.60"	197.0637	323520.776	4866023.451	198.179	234.367
P205	43°56'05.49"	79°15'59.23"	198.1821	323551.047	4866123.219	199.297	235.483
P206	43°56'05.97"	79°15'55.93"	198.2377	323624.601	4866138.240	199.353	235.539
P207	43°56'06.35"	79°15'53.11"	198.9759	323687.458	4866150.146	200.091	236.276
P208	43°56'06.71"	79°15'50.29"	199.0586	323750.316	4866161.436	200.174	236.359
P209	43°56'06.90"	79°15'48.88"	199.4629	323781.745	4866167.389	200.578	236.762
P210	43°56'05.17"	79°16'01.51"	197.105	323500.228	4866113.199	198.22	234.407
P211	43°56'07.46"	79°15'45.94"	199.9267	323847.262	4866184.860	201.042	237.226
P212	43°56'06.98"	79°15'46.86"	199.4234	323826.787	4866169.987	200.538	236.722
S1	43°56'03.39"	79°16'01.04"	196.9978	323510.864	4866058.296	198.113	234.301
S2	43°56'04.38"	79°16'00.14"	197.308	323530.850	4866088.905	198.423	234.61
S3	43°56'05.16"	79°15'56.43"	198.1078	323613.521	4866113.211	199.223	235.409

Table 1: Markham Area Point Coordinates Based on Total Station Survey

Point ID	Easting [m]	Northing [m]
1	323489.274	4866159.386
2	323468.941	4866133.955
3	323483.658	4866091.160
4	323461.428	4866080.566
5	323484.754	4866005.508
6	323494.475	4866128.090
7	323514.014	4866106.781
8	323528.027	4866098.291
9	323526.076	4866071.391
10	323501.889	4866069.302
11	323517.255	4866045.333
12	323525.282	4866027.644
13	323549.042	4866006.948
14	323548.442	4866067.711

15	323581.247	4866027.527
16	323556.439	4866135.870
17	323547.072	4866147.152
18	323579.980	4866120.925
19	323626.688	4866190.534
20	323623.804	4866159.540
21	323626.773	4866119.490
22	323650.308	4866093.463
23	323650.526	4866150.615
24	323680.953	4866128.238
25	323718.581	4866172.559
26	323729.695	4866139.601
27	323773.133	4866156.549
28	323790.428	4866222.728
29	323795.587	4866194.013
30	323803.576	4866149.083
31	323810.901	4866122.383
32	323748.664	4866168.579
201	323519.994	4866086.921
203	323520.270	4866023.166
205	323551.039	4866122.969
206	323624.674	4866138.248
207	323687.477	4866149.862
208	323750.244	4866161.422
209	323781.727	4866167.248
210	323500.228	4866113.199
211	323847.315	4866184.733
212	323826.746	4866169.992
S1	323510.580	4866058.023
S2	323530.483	4866088.911
S3	323613.595	4866113.068

Table A-6: TS VS GNSS

Point	GNSS Derived Coordinates			Total Station Derived Coordinates			Difference (GNSS - TS)					
	E [m]	N [m]	Orthometric Height [m]	E [m]	N [m]	Orthometric Height [m]	D_E [m]	D_N [m]	D_Z [m]	2D Positional [m]	3D Positional [m]	
1	323488.946	4866159.46	234.144	323489.274	4866159.386	234.142	-0.3280	0.0737	0.0020	0.3362	0.3362	
2	323468.724	4866133.788	233.876	323468.9414	4866133.955	233.849	-0.2174	-0.1673	0.0270	0.2744	0.2757	
3	323483.786	4866091.241	233.903	323483.6578	4866091.16	233.896	0.1282	0.0811	0.0070	0.1517	0.1519	
4	323461.738	4866080.378	233.366	323461.4278	4866080.566	233.555	0.3102	-0.1881	-0.1890	0.3628	0.4090	
5	323485.812	4866005.453	233.751	323484.7541	4866005.508	233.742	1.0579	-0.0554	0.0090	1.0594	1.0594	
6	323494.387	4866128.305	234.171	323494.4754	4866128.09	234.062	-0.0884	0.2150	0.1090	0.2324	0.2567	
7	323514.072	4866107.066	228.844	323514.0136	4866106.781	234.495	0.0584	0.2848	-5.6510	0.2907	5.6585	
8	323528.147	4866098.465	234.801	323528.0272	4866098.291	234.701	0.1198	0.1739	0.1000	0.2112	0.2337	
9	323526.661	4866071.611	234.085	323526.0755	4866071.391	234.47	0.5855	0.2204	-0.3850	0.6256	0.7346	
10	323502.358	4866069.382	233.751	323501.8893	4866069.302	234.125	0.4687	0.0798	-0.3740	0.4754	0.6049	
11	323518.038	4866045.355	234.357	323517.2548	4866045.333	234.372	0.7832	0.0215	-0.0150	0.7835	0.7836	
12	323526.116	4866027.787	233.973	323525.2824	4866027.644	234.323	0.8336	0.1433	-0.3500	0.8458	0.9154	
13	323550.038	4866007.177	234.4	323549.0419	4866006.948	234.589	0.9961	0.2291	-0.1890	1.0221	1.0394	
14	323548.751	4866007.97	234.894	323548.4422	4866007.711	234.985	0.3088	0.2590	-0.0910	0.4030	0.4132	
15	323528.872	4866027.636	234.775	323528.1468	4866027.527	234.999	0.6252	0.1089	-0.2240	0.6346	0.6730	
16	323556.364	4866135.887	235.162	323556.4393	4866135.857	234.921	-0.0753	0.0169	0.2410	0.0772	0.2531	
17	323546.965	4866147.279	234.525	323547.0721	4866147.152	234.486	-0.1071	0.1267	0.0390	0.1659	0.1704	
18	323580.046	4866121.14	235.207	323579.9803	4866120.925	235.129	0.0657	0.2149	0.0780	0.2248	0.2379	
19	323626.682	4866190.711	234.882	323626.688	4866190.534	234.95	-0.0060	0.1772	-0.0680	0.1773	0.1899	
20	323623.871	4866159.533	235.343	323623.8037	4866159.54	235.262	0.0673	-0.0066	0.0810	0.0676	0.1055	
21	323626.884	4866119.73	235.81	323626.7734	4866119.49	235.464	0.1106	0.2398	0.3460	0.2641	0.4353	
22	323650.375	4866093.565	235.511	323650.3075	4866093.463	235.581	0.0675	0.1017	-0.0700	0.1220	0.1407	
23	323650.436	4866150.658	235.693	323650.5261	4866150.615	235.664	-0.0901	0.0430	0.0290	0.0998	0.1039	
25	323718.616	4866172.764	236.038	323718.5813	4866172.559	236.197	0.0347	0.2049	-0.1590	0.2078	0.2617	
26	323729.638	4866139.774	236.04	323729.6952	4866139.601	236.061	-0.0572	0.1725	-0.0210	0.1818	0.1830	
27	323773.078	4866156.563	236.641	323773.1327	4866156.549	236.45	-0.0547	0.0142	0.1910	0.0565	0.1992	
28	323790.506	4866222.965	237.151	323790.4281	4866222.728	237.194	0.0779	0.2369	-0.0430	0.2494	0.2531	
29	323795.495	4866194.278	236.851	323795.5867	4866194.013	236.648	-0.0917	0.2646	0.2030	0.2801	0.3459	
30	323803.652	4866149.244	236.647	323803.5756	4866149.083	236.621	0.0764	0.1608	0.0260	0.1780	0.1799	
31	323810.866	4866122.415	236.816	323810.9008	4866122.383	236.994	-0.0348	0.0317	-0.1780	0.0470	0.1841	
32	323748.734	4866168.838	236.261	323748.6644	4866168.579	236.377	0.0696	0.2585	-0.1160	0.2677	0.2918	
201	323520.15	4866087.023	234.895	323519.9942	4866086.921	234.535	0.1558	0.1021	0.3600	0.1863	0.4053	
203	323520.776	4866023.451	234.367	323520.2696	4866023.166	234.256	0.5064	0.2847	0.111	0.5809	0.5914	
205	323551.047	4866123.219	235.483	323551.0389	4866122.969	234.961	0.0081	0.2501	0.522	0.2503	0.5789	
206	323624.601	4866138.24	235.539	323624.6745	4866138.248	235.46	-0.0735	-0.0077	0.079	0.0739	0.1081	
207	323687.458	4866150.146	236.276	323687.4769	4866149.862	235.966	-0.0189	0.2840	0.31	0.2846	0.4209	
208	323750.316	4866161.436	236.359	323750.2445	4866161.422	236.386	0.0715	0.0138	-0.027	0.0728	0.0777	
209	323781.745	4866167.389	236.762	323781.7269	4866167.248	236.548	0.0181	0.1409	0.214	0.1421	0.2569	
210	323500.228	4866113.199	234.407	323500.228	4866113.199	234.257	0.0000	0.0000	0.15	0	0.15	
211	323847.262	4866184.86	237.226	323847.3154	4866184.733	236.861	-0.0534	0.1267	0.365	0.1375	0.3900	
212	323826.787	4866169.987	236.722	323826.746	4866169.992	236.744	0.0410	-0.0049	-0.022	0.0413	0.0468	
S1	323510.864	4866058.296	234.3	323510.5804	4866058.023	234.300	0.2836	0.2733	0	0.3939	0.3939	
S2	323530.85	4866088.905	234.61	323530.4826	4866088.911	234.553	0.3674	-0.0063	0.057	0.3675	0.3719	
S3	323613.521	4866113.211	235.409	323613.5952	4866113.068	235.238	-0.0742	0.1426	0.171	0.1607	0.2347	
							avg diff	0.1574	0.1213	-0.0987	0.2970	0.4797
							std dev diff	0.3152	0.1198	0.8783	0.2528	0.8367
24	323679.46	4866139.322	235.855	323680.9527	4866128.238	235.705	-1.4927	11.0840	0.1500	11.1840	11.1851	
202	323507.424	4866012.92	233.666	-	-	-	-	-	-	-	-	

Table A-7: Markham Area Point Orthometric Heights

Point ID	GNSS Derived Orthometric Height [m]			Total Station Derived Orthometric Height [m]		
1	234.144			234.142		
2	233.876			233.849		
3	233.903			233.896		
4	233.366			233.555		
5	233.751			233.742		
6	234.171			234.062		
7	228.844			234.495		
8	234.801			234.701		
9	234.085			234.47		
10	233.751			234.125		
11	234.357			234.372		
12	233.973			234.323		
13	234.400			234.589		
14	234.894			234.985		
15	234.775			234.999		
16	235.162			234.921		
17	234.525			234.486		

18	235.207	235.129
19	234.882	234.95
20	235.343	235.262
21	235.810	235.464
22	235.511	235.581
23	235.693	235.664
24	235.855	235.705
25	236.038	236.197
26	236.040	236.061
27	236.641	236.450
28	237.151	237.194
29	236.851	236.648
30	236.647	236.621
31	236.816	236.994
32	236.261	236.377
201	234.895	234.535
203	233.666	234.256
205	234.367	234.961
206	235.483	235.460
207	235.539	235.966
208	236.276	236.386
209	236.359	236.548
210	236.762	234.257
211	234.407	236.861
212	237.226	236.744
S1	236.722	234.300
S2	234.300	234.553
S3	234.610	235.238

Appendix B: Oshawa Bridge Ground Survey

PLANIMETRIC SURVEY NETWORK

Three points were surveyed using GNSS methods (given in Appendix D), while a total of 44 points were surveyed using a total station. A traverse of 4 points was set for the total station survey TOPO1, RIVER1, TOPO2, and S1. Besides the ground targets, we have also used reflective tape survey targets for the areas that were accessible and landmarks (graffiti edges- cracks- cement plates connections) for the inaccessible areas.

Table B-1: Notable Points in Oshawa Area Survey

GNSS Surveyed Points	Total Station Traverse Points
TOPO1	TOPO1
RIVER1	RIVER1
TOPO2	TOPO2
-	S1

To solve the network, a total of 24 observations were used – 8 directional angles, 8 zenith angles, and 8 slope distances. The system had 12 degrees of freedom, with a total of 16 unknowns (the XYZ of each of the 4 points). Being constrained, the coordinates of S1 and TOPO2 were held fixed during the adjustment process.

Solving the network at a confidence level of 95% resulted in the following.

Table B-2: Results of Oshawa (Local) Traverse Network

Point	Coordinate Component	Approximate Value (m)	Adjusted Value (m)	Standard Deviation (mm)
RIVER1	X	951.82679	951.82688	5.5
	Y	1032.17431	1032.17340	4.2
	Z	996.80851	996.80617	2.5
S1	X	1000.00000	1000.00000	0.0
	Y	1020.47200	1020.47061	2.5
	Z	995.94200	995.94526	1.5
TOPO1	X	942.47610	942.47533	5.3
	Y	1027.28742	1027.28701	5.0
	Z	999.53185	999.53125	2.4
TOPO2	X	1000.00000	1000.00000	0.0
	Y	1000.00000	1000.00139	2.5

	Z	1000.00000	1000.00000	0.0
--	---	------------	------------	-----

The mean errors and parameters of the error ellipses of the control points were determined as follows.

Table B-3: Mean Errors and Parameters of the Error Ellipses of Oshawa (Local) Traverse Network

Point	mp (mm)	mxy (mm)	Mean Error Ellipse			Confidence Error Ellipse		g
			a (mm)	b	Alpha (gons)	a' (mm)	b'	
RIVER1	6.9	4.9	5.5	4.2	194.5	15.4	11.7	0.1
S1	2.5	1.8	2.5	0.0	100.0	7.0	0.0	0.0
TOPO1	7.3	5.2	5.4	4.9	172.0	15.2	13.7	0.1
TOPO2	2.5	1.8	2.5	0.0	100.0	7.0	0.0	0.0

VERTICAL SURVEY NETWORK

Like in the St. Catharine's survey area, only trigonometric levelling was performed in the Oshawa survey area. Similarly, first the orthometric heights of the defined traverse points were found and adjusted, then heights were propagated to remaining survey points.

Traverse points in the survey area consisted of TOPO1, TOPO2, RIVER1, and S1 (shown in figure below). As observation to each traverse point were made in both directions (ex. from TOPO2 to S1 and S1 to TOPO2), loops were treated in a double-run manner. The GNSS orthometric height at point TOPO1 was used as the fixed elevation and propagated through to the remaining traverse points. As in the St. Catharine's survey area, each loop was adjusted based on a weighted contribution of distance to the total misclosure. That is, loop segments were adjusted based on the distance between points to the total distance of the loop. The calculated elevations for the control points through the double-run were then averaged.

Again, the remaining elevations of survey points were found by applying standard trigonometric levelling techniques. The elevations determined from the above loop calculations were used as station elevations for each setup, accordingly. Obtained elevations for any remaining survey point observed multiple times (from different station setups) were averaged.

It is observed that a particularly large discrepancy exists between the GNSS derived orthometric height and levelling determined orthometric height for point RIVER1. It is believed that this is a result of a poor GNSS survey of the point. Again, it is believed that

the GNSS survey points have had incorrect antenna heights entered when processing and surveying, therefore causing errors in determined ellipsoid and orthometric heights.

It should be noted that the following differences were made to the total station collected data, due to errors that occurred when storing observations in the instrument:

-Target height of S1 from TOPO2 changed from 1.461m to 1.457m

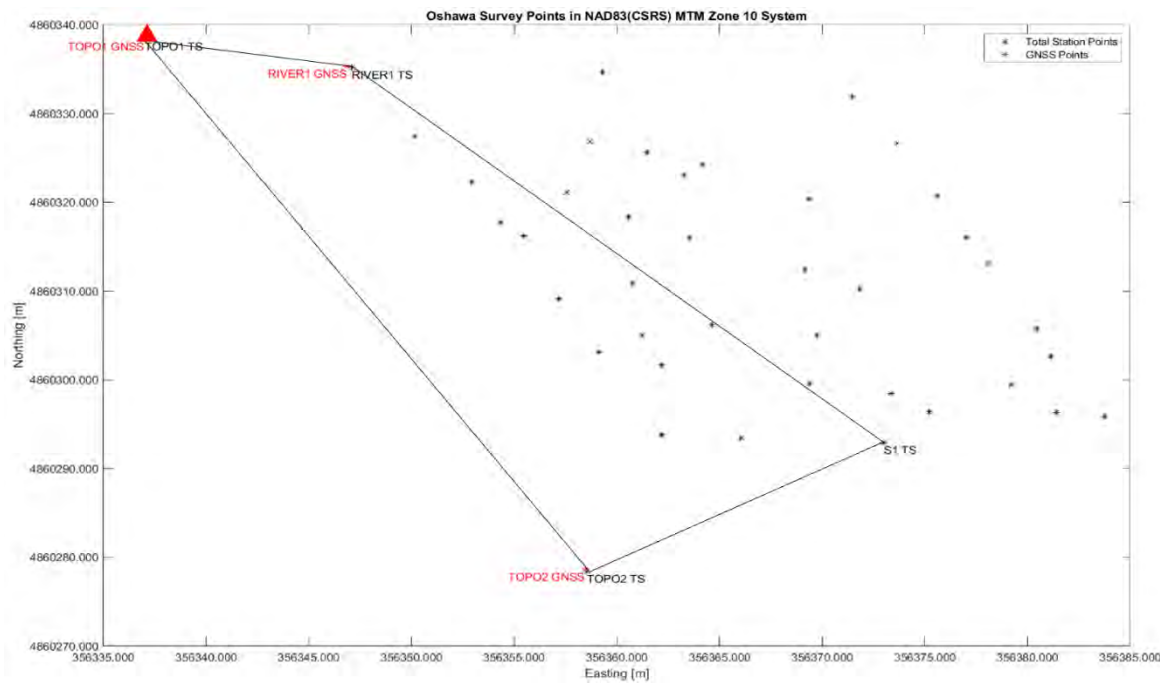


Figure B-1 – Ground points and levelling loop of the Oshawa Survey site

Table B-4: Oshawa Area Point Coordinates Based on GNSS Survey

Point	WGS84			NAD83(CRS) MTM Zone 10			
	Latitude (North)	Longitude (West)	Ellipsoi d Height [m]	Easting [m]	Northing [m]	Ellipsoi d Height [m]	Orthometri c Height [m]
TOPO 1	43°52'52.42 "	78°51'31.19 "	54.6393	356337.02 0	4860338.32 1	55.758	92.036
TOPO 2	43°52'50.48 "	78°51'30.25 "	54.5718	356358.46 7	4860278.61 4	55.691	91.970
RIVER 1	43°52'52.32 "	78°51'30.75 "	51.3691	356346.86 5	4860335.31 1	52.488	88.766

Table B-5: Oshawa Area Point Coordinates Based on Total Station Survey

Point	Easting [m]	Northing [m]
C1	356359.2994	4860334.6826
25	356357.5679	4860321.0864
23	356363.5267	4860315.9626
29	356360.7486	4860310.8196
29	356360.7457	4860310.8253
28	356369.1539	4860312.3710
28	356369.1560	4860312.3788
24	356364.1833	4860324.2090
P6	356350.1474	4860327.4124
W1	356371.4661	4860331.8919
W2	356373.6444	4860326.6256
W3	356375.6087	4860320.6594
C2	356358.6942	4860326.8237
C3	356363.2619	4860323.0324
C4	356361.4710	4860325.6331
C5	356347.0949	4860335.1870
C6	356377.0338	4860316.0099
W4	356380.4437	4860305.7055
C7	356360.5577	4860318.3025
C8	356373.3424	4860298.4275
26	356366.0383	4860293.4506
22	356362.1767	4860301.6285
31	356369.7391	4860304.9810
27	356375.2027	4860296.3699
P1	356362.2008	4860293.7768
P2	356359.1298	4860303.0892
P3	356357.1795	4860309.1559
P4	356354.3499	4860317.7639
P5	356352.9307	4860322.2606
W5	356383.7351	4860295.8731
W6	356381.4013	4860296.3280
W7	356379.2055	4860299.4376
W8	356381.126	4860302.649
W9	356378.065	4860313.152
C10	356369.388	4860299.588
C11	356364.646	4860306.172
C12	356361.221	4860304.990
C13	356371.829	4860310.239
C14	356355.465	4860316.215

C15	356369.344	4860320.380
TOPO1	356337.020	4860338.321
TOPO2	356358.543	4860278.402
RIVER1	356347.095	4860335.187
S1	356372.983	4860292.910

Table B-6: Oshawa Area Point Orthometric Heights

Point ID	GNSS Derived Orthometric Height [m]	Total Station Derived Orthometric Height [m]
TOPO1	92.036	92.036
TOPO2	91.970	92.505
RIVER1	88.766	89.311
S1	-	88.449
C1	-	95.719
C2	-	95.594
C3	-	95.789
C4	-	95.783
C5	-	90.714
C6	-	92.063
C7	-	95.456
C8	-	95.676
C10	-	95.772
C11	-	95.464
C12	-	94.563
C13	-	95.411
C14	-	93.243
C15	-	95.282
W1	-	90.335
W2	-	90.014
W3	-	90.623
W4	-	89.612
W5	-	91.139
W6	-	93.932
W7	-	94.403
W8	-	92.466
W9	-	90.737
P1	-	90.381
P2	-	90.846
P3	-	90.539
P4	-	91.017
P5	-	90.112
P6	-	90.556
22	-	88.603

23	-	88.937
24	-	88.629
25	-	88.941
26	-	88.690
27	-	88.497
28	-	88.774
29	-	88.946
31	-	88.911

Appendix C: St. Catharine's Bridge Ground Survey

PLANIMETRIC SURVEY NETWORK

In the St. Catharine's survey area, 4 points were surveyed using GNSS methods while a total of 45 points, including the previous 4, were surveyed using a total station (TS). A traverse of 6 points was set for the total station survey.

Table C-1: Notable Points in St. Catharines' site Survey

GNSS Surveyed Points	Total Station Traverse Points
P24	P24
P25	P25
BASE	BASE
G1	G1
-	S1
-	S2

To perform the transformation, the local coordinates of the total station observed points were shifted from P25_Local to P25_GNSS and rotated by the difference in azimuths of P25_Local-BASE_Local and P25_GNSS-BASE_GNSS.

Transformation residuals between expected coordinates (ex. GNSS derived coordinates) and transformed coordinates suggest an error to occur in the GNSS measured coordinate of point G1. This is further supported by the error in 3D position provided in it's GNSS post-processing report.

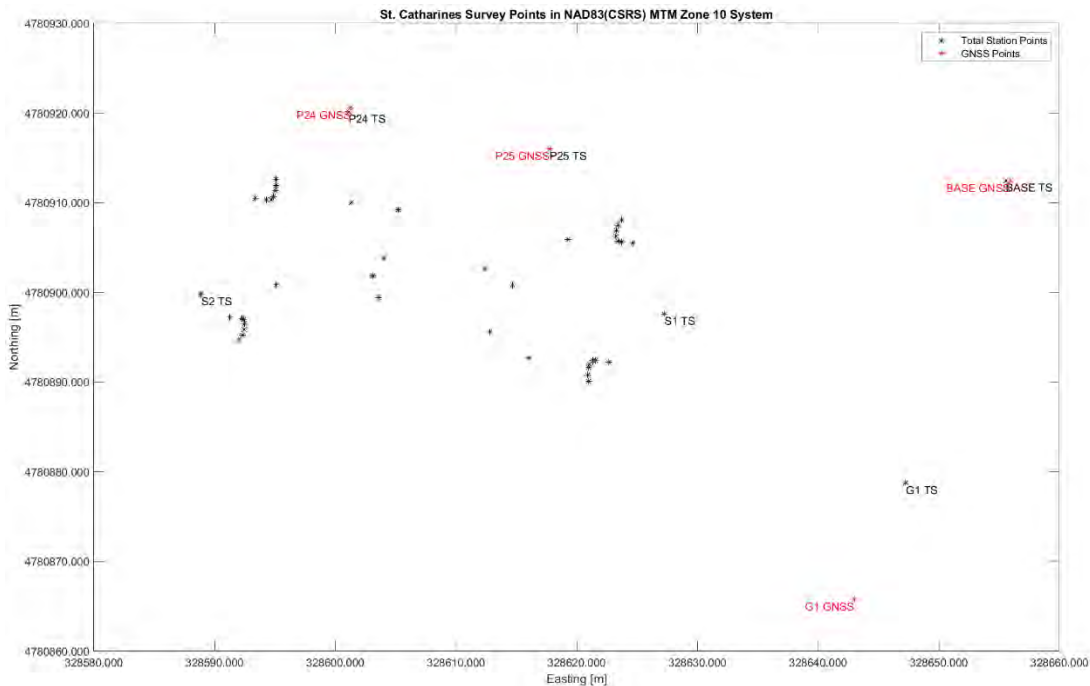


Figure C-1 - Transformed St. Catharine's Area Total Station Coordinates Compared Against GNSS Measured Points

PLANIMETRIC SURVEY NETWORK ADJUSTMENT

A total of 6 control points was used when traversing in the Oshawa region – S2, P24, P25, BASE, G1, and S1.

To solve the network, a total of 57 observations were used – 19 directional angles, 19 zenith angles, and 19 slope distances. The system had 37 degrees of freedom, with a total of 24 unknowns (the XYZ of each of the 6 points). Being constrained, the coordinates of S2 and P24 were held fixed.

Solving the constrained network at a confidence level of 95% resulted in the following coordinates.

Table C-2: Results of St. Catharines' (Local) Traverse Network

Point	Coordinate Component	Approximate Value (m)	Adjusted Value (m)	Standard Deviation (mm)
P24	X	1000.00000	1000.00000	0.0
	Y	1023.74200	1023.74235	0.9
	Z	1000.12400	1000.07537	0.3
P25	X	1016.39445	1016.39425	1.8

	Y	1028.76682	1028.76762	1.3
	Z	1000.23222	1000.18375	0.5
BASE	X	1050.61268	1050.61167	2.6
	Y	1045.19020	1045.19330	2.8
	Z	1000.02004	999.97301	0.9
G1	X	1060.86417	1060.86545	2.6
	Y	1012.01897	1012.02292	3.2
	Z	1000.14225	1000.09363	0.9
S1	X	1033.99993	1034.00059	2.1
	Y	1017.88438	1017.88664	0.8
	Z	1000.29817	1000.35343	0.7
S2	X	1000.00000	1000.00000	0.0
	Y	1000.00000	999.99965	0.9
	Z	1000.00000	1000.04863	0.3

The mean errors and parameters of the error ellipse were determined as summarized below.

Table C-3: Mean Errors and Parameters of the Error Ellipses of St. Catharine's (Local) Traverse Network

Point	mp (mm)	mxy (mm)	Mean Error Ellipse			Confidence Error Ellipse		g
			a (mm)	b	Alpha (gons)	a' (mm)	b'	
P24	0.9	0.6	0.9	0.0	100.0	2.3	0.0	0.0
P25	2.2	1.6	1.9	1.2	178.0	4.8	3.0	0.0
BASE	3.8	2.7	2.9	2.5	61.4	7.5	6.3	0.0
G1	4.1	2.9	3.3	2.5	114.3	8.3	6.5	0.0
S1	2.8	2.0	2.2	1.7	169.3	5.6	4.3	0.0
S2	0.9	0.6	0.9	0.0	100.0	2.3	0.0	0.0

VERTICAL SURVEY NETWORK

In the St. Catharines' survey area, only trigonometric levelling was performed. However, in a similar manner as in differential levelling, first the orthometric heights of the defined traverse points were found and adjusted, then heights were propagated to remaining survey points.

Recalling, traverse points in the survey area were P25, P24, S2, S1, G1, and BASE (shown in figure below). As observation to each traverse point were made in both directions (ex. from P25 to P24 and P24 to P25), loops were treated in a double-run manner. The GNSS

orthometric height at point P25 was used as the fixed elevation and propagated through to the remaining traverse points. Each loop was adjusted based on a weighted contribution of distance to the total misclosure. That is, loop segments were adjusted based on the distance between points to the total distance of the loop. The calculated elevations for the control points through the double-run were then averaged.

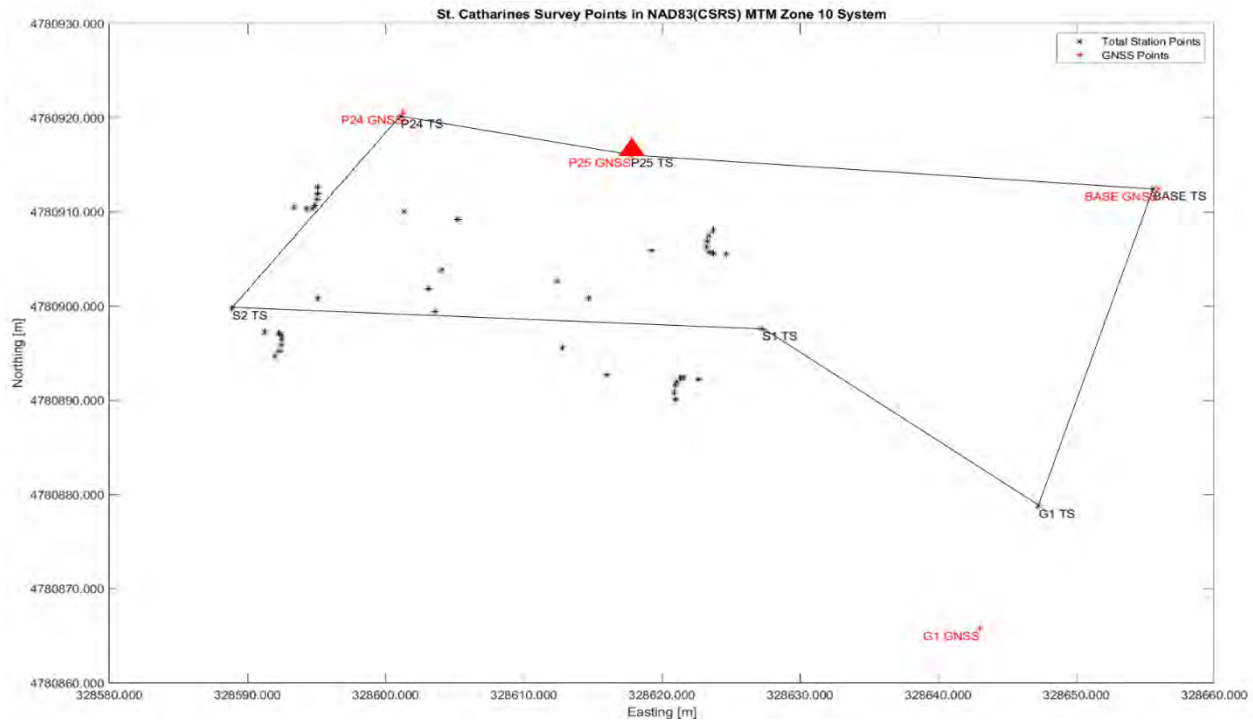


Figure C-2 - Levelling Loop of St. Catharine's Survey Area

The remaining elevations of survey points were found by applying standard trigonometric levelling techniques. The elevations determined from the above loop calculations were used as station elevations for each setup, accordingly. Obtained elevations for any remaining survey point observed multiple times (from different station setups) were averaged.

It is observed that a large discrepancy exists between the GNSS derived orthometric heights and levelling determined orthometric heights for points G1 and BASE. It is believed that this is a result of a poor GNSS survey of the points (as suggested by their large positional errors in the GNSS processing report). It is believed that the GNSS survey points have had incorrect antenna heights entered when processing and surveying, therefore causing errors in determined ellipsoidal and orthometric heights.

It should be noted that the following differences were made to the total station collected data, due to errors that occurred when storing observations in the instrument:

-Target height of P24 from station P25 was changed from 1.456m to 1.460m

-Target height of BASE from station P25 was changed from 1.458m to 1.438m

-Target height of BASE from station G1 was changed from 1.465m to 1.448m

Table C-4: St. Catharines Site Point Coordinates Based on GNSS Survey

Point	WGS84			NAD83(CRS) MTM Zone 10			
	Latitude (North)	Longitude (West)	Ellipsoid Height [m]	Easting [m]	Northing [m]	Ellipsoid Height [m]	Orthometric Height [m]
P24	43°10'03.97 "	79°12'26.23 "	65.4882	328601.25 8	4780920.58 5	66.627	102.507
P25	43°10'03.82 "	79°12'25.50 "	65.5897	328617.76 2	4780916.01 4	66.729	102.609
BASE	43°10'03.70 "	79°12'23.81 "	66.0074	328655.94 6	4780912.44 4	67.146	103.026
G1	43°10'02.19 "	79°12'24.39 "	58.7509	328643.00 9	4780865.80 5	59.890	95.769

Table C-5: St. Catharine's Area Point Coordinates Based on Total Station Survey

Point ID	Easting [m]	Northing [m]
23	328604.0439	4780903.8299
31	328601.3577	4780910.0538
P1	328593.3590	4780910.4863
P2	328594.2873	4780910.3266
P3	328591.2689	4780897.2659
P4	328592.2491	4780897.0995
P5	328623.4224	4780907.5251
P6	328623.2973	4780906.9051
P7	328623.2297	4780906.2738
P8	328621.0850	4780891.9699
P9	328620.9964	4780891.6475
P10	328620.9086	4780890.8195
22	328612.3840	4780902.6664
28	328619.2767	4780905.8912
T1	328612.8132	4780895.5839
T2	328616.0029	4780892.6945
T3	328614.6981	4780900.8616
T4	328621.0037	4780890.0765
T5	328621.3540	4780892.4218
T6	328623.3955	4780905.7205
T7	328623.7047	4780908.0905
P11	328622.6737	4780892.2476

P12	328621.5832	4780892.4207
P13	328624.6353	4780905.5009
P14	328623.7172	4780905.6404
P15	328592.2910	4780895.2617
P16	328592.4262	4780895.8734
P17	328592.5019	4780896.5103
P18	328594.8883	4780910.6633
P19	328595.0301	4780911.3363
P20	328595.1069	4780911.9539
T9	328595.0822	4780900.8152
T8	328603.5954	4780899.4369
T10	328603.1264	4780901.8357
T11	328605.2218	4780909.2277
T12	328592.0174	4780894.6935
T13	328592.4209	4780897.0068
T14	328594.6732	4780910.3282
T15	328595.0665	4780912.6558
P24	328601.1200	4780920.1456
P25	328617.7620	4780916.0140
BASE	328655.5529	4780912.4808
G1	328647.2674	4780878.7648
S1	328627.2546	4780897.6219
S2	328588.8973	4780899.7907

Table C-6: St. Catharines' Area Point Orthometric Heights

Point ID	GNSS Derived Orthometric Height [m]	Total Station Derived Orthometric Height [m]
24	102.507	102.501
25	102.609	102.609
BASE	103.026	102.396
G1	95.769	102.516
S1	-	102.776
S2	-	102.474
22	-	102.665
23	-	102.579
28	-	102.633
31	-	102.472
P1	-	104.752
P2	-	104.805
P3	-	104.747
P4	-	104.831
P5	-	104.612

P6	-	103.602
P7	-	104.408
P8	-	104.798
P9	-	103.632
P10	-	104.734
P11	-	104.916
P12	-	105.073
P13	-	104.393
P14	-	104.534
P15	-	104.699
P16	-	103.872
P17	-	104.704
P18	-	104.819
P19	-	104.096
P20	-	104.862
T1	-	116.663
T2	-	116.824
T3	-	116.576
T4	-	111.260
T5	-	111.268
T6	-	111.222
T7	-	111.203
T8	-	116.317
T9	-	116.060
T10	-	116.234
T11	-	116.169
T12	-	110.157
T13	-	110.160
T14	-	110.179
T15	-	110.180

Appendix D: GNSS Surveying St Catharines & Oshawa Bridges

DATA COLLECTION PROCEDURES

For the MTO/UAV project, GNSS points were set up around the two bridges that need surveying. In total, three points were surveyed in the St Catharines bridge and two points were surveyed at the Oshawa bridge. GNSS surveying of the positions of these targets was performed using post-processed relative positioning. The Leica GS15 receivers have been used for this purpose.



Figure D-1 - Leica CS15 used for the GNSS surveying

In order to perform the relative positioning, one receiver must be set-up as a reference receiver (or base). For each of the bridges, an additional point has been surveyed and its position used as a reference to perform relative positioning.

Table 1 shows the names of each of the points surveyed. In order to get the precise position of the base receiver (BASE in ST-CATH and TOP1 in OSHAWA), one of the other points is temporarily used as a reference.

Table D-1: Configuration of the points in the processing

	Reference receiver/point	Rover
ST CATHARINES	BASE	G1
	BASE	P25
	BASE	P24
	P25	BASE
OSHAWA	TOP1	TOP2
	TOP1	RIVER1
	TOP2	TOP1

All the receivers were set up on tribrachs and tripods which were levelled and centered so that they point at the center of the targets. The GNSS data collection is started on each receiver and the heights from the ground point to the GNSS antenna were measured. Figures 1 and 2 show the duration of the data collection for each point in both bridges.



Figure D-2 - Data collection duration in ST CATHARINES

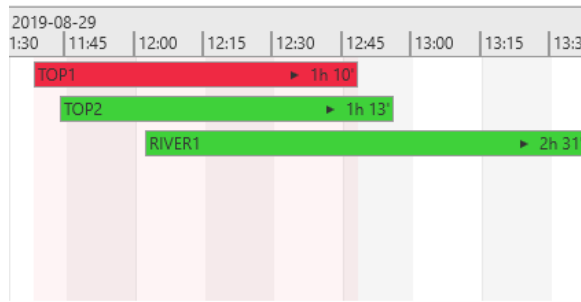


Figure D-3 - Data collection duration in OSHAWA

At the Oshawa bridge, both rovers (TOP2 and RIVER1) were left collecting data after the base (TOP1) was stopped. In the processing, the rovers are only processed when both measurements from the base and rover are available.

DATA PROCESSING PROCEDURE

The data was extracted from the Leica receivers using USBs and sorted using a computer. A first check was done to make sure that all the points have been extracted properly and that they are properly named for the processing. Once that was done, all the points were imported into the Leica Infinity software. The RTK solution was then initiated by choosing

the appropriate base and rover and reports for each of the files were generated by the software.

The next step was to extract the final positions from the reports as well as other relevant information, compute the 2D and 3D standard deviations and put everything together into one document.

Coordinates

	Reference - TOP1	Rover - TOP2	Reference - TOP1	Rover - TOP2
Point Role:	Navigated RTK	Fixed PP	-	-
WGS84 Latitude:	43° 52' 52.42" N	43° 52' 50.48" N	Easting:	-
WGS84 Longitude:	78° 51' 31.20" W	78° 51' 30.25" W	Northing:	-
WGS84 Ellip. Height:	54.1876 m	54.5718 m	Ortho. Height:	-
WGS84 Cartesian X:	889,760.2070 m	889,788.9731 m		
WGS84 Cartesian Y:	-4,517,890.9275 m	-4,517,927.9896 m		
WGS84 Cartesian Z:	4,398,626.7240 m	4,398,583.6858 m		

Baseline Vector and Quality - WGS84

ΔLatitude:	-0° 00' 01.95"	SD ΔLatitude:	0.0002 m
ΔLongitude:	0° 00' 00.94"	SD ΔLongitude:	0.0001 m
ΔHeight:	0.3843 m	SD ΔHeight:	0.0004 m
ΔX:	28.7661 m	SD ΔX:	0.0001 m
ΔY:	-37.0621 m	SD ΔY:	0.0003 m
ΔZ:	-43.0381 m	SD ΔZ:	0.0002 m
Slope Dist.:	63.6661 m	SD Slope Dist.:	0.0001 m
M0:	0.8233 m	CQ 1D:	0.0004 m
Q11:	0.00000002	CQ 2D:	0.0002 m
Q12:	-0.00000004	CQ 3D:	0.0004 m
Q22:	0.00000016		
Q13:	0.00000002		
Q23:	-0.00000009		
Q33:	0.00000009		
Frequency:	L1/L2	GDOP:	2.9 - 10.9
Solution Optimisation:	None	PDOP:	2.5 - 8.9
Solution Type:	Phase Fixed	HDOP:	1.0 - 4.1
		VDOP:	2.3 - 8.3
Ephemeris Type:		GPS SVs:	7/7
GPS	Broadcast	GLONASS SVs:	-
		Beidou SVs:	-
		Galileo SVs:	-
		QZSS SVs:	-

Figure D-4 - Example of extracted output of the Leica Infinity processing

The final positions are attached in the tables below. It can be noted that the accuracy of point G1 in the St. Catharines bridge is almost at the meter level. The reason behind that is that the float RTK solution wasn't reliable enough to be able to get a fixed solution with the desired accuracy. This could be because point G1 was surrounded by an area populated by high and dense vegetation which leads to multipath and therefore measurements that are not 'good enough' to be able to fix the ambiguities. Figures 5 and 6 show the signals tracked by both G1 and P24 and it is noticeable how G1 measurements are discontinuous and filled with cycle-slips which affect fixing the ambiguities.

Table D-2: Final positions in Oshawa

Base station	Rover	WGS84 Latitude	WGS84 Longitude	WGS84 Height [m]	3D RMS [m]
BASE	G1	43°10'02.17" N	79°12'24.38" W	58.5312	0.8417
BASE	P25	43°10'03.82" N	79°12'25.50" W	65.4907	0.0002
BASE	P24	43°10'03.97" N	79°12'26.23" W	65.5662	0.0007
P25	BASE	43°10'03.70" N	79°12'23.81" W	66.1064	0.0002

Table 11: Final positions in St. Catharines

Base station	Rover	WGS84 Latitude	WGS84 Longitude	WGS84 Height [m]	3D RMS [m]
BASE	G1	43°52'50.48" N	79°12'24.38" W	54.5718	0.0004
BASE	P25	43°52'52.32" N	78°21'30.75" W	51.3691	0.0010
P25	BASE	43°52'52.42" N	78°51'31.19" W	64.6393	0.0004

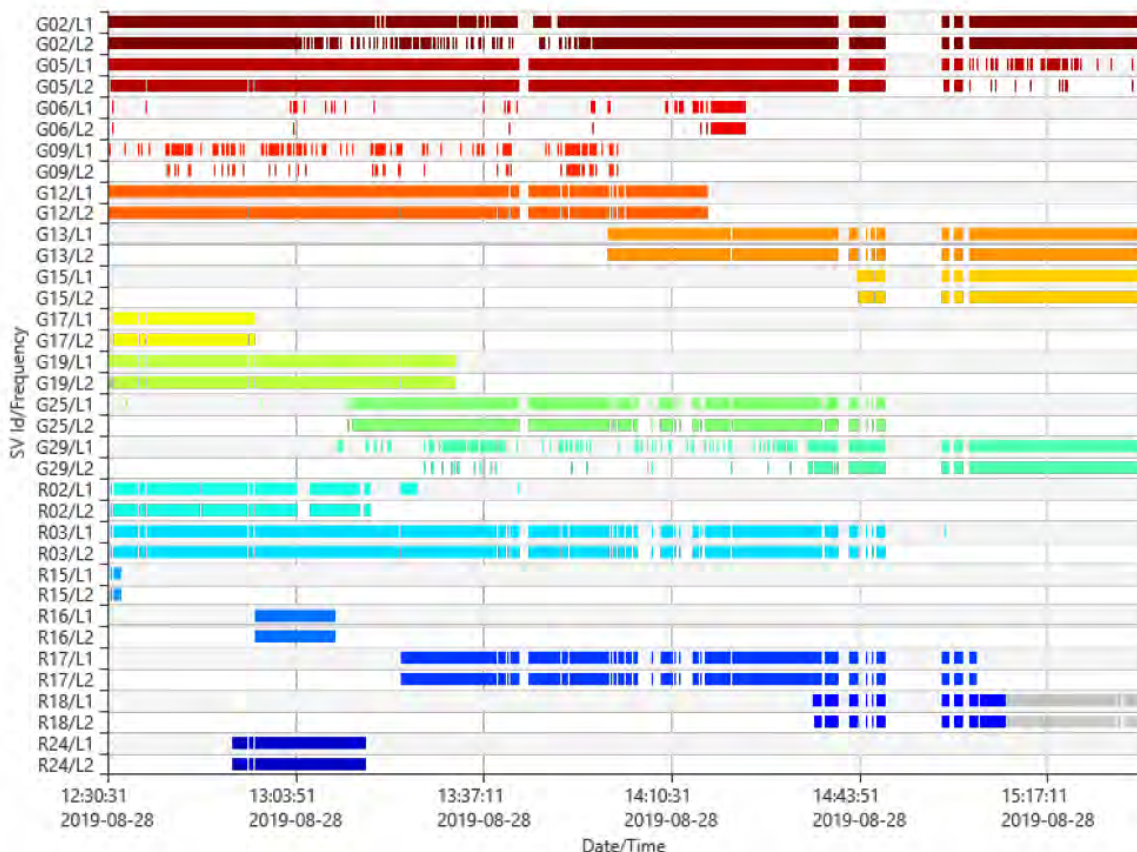


Figure D-5 - Signals tracked by receiver G1 in St. Catharines

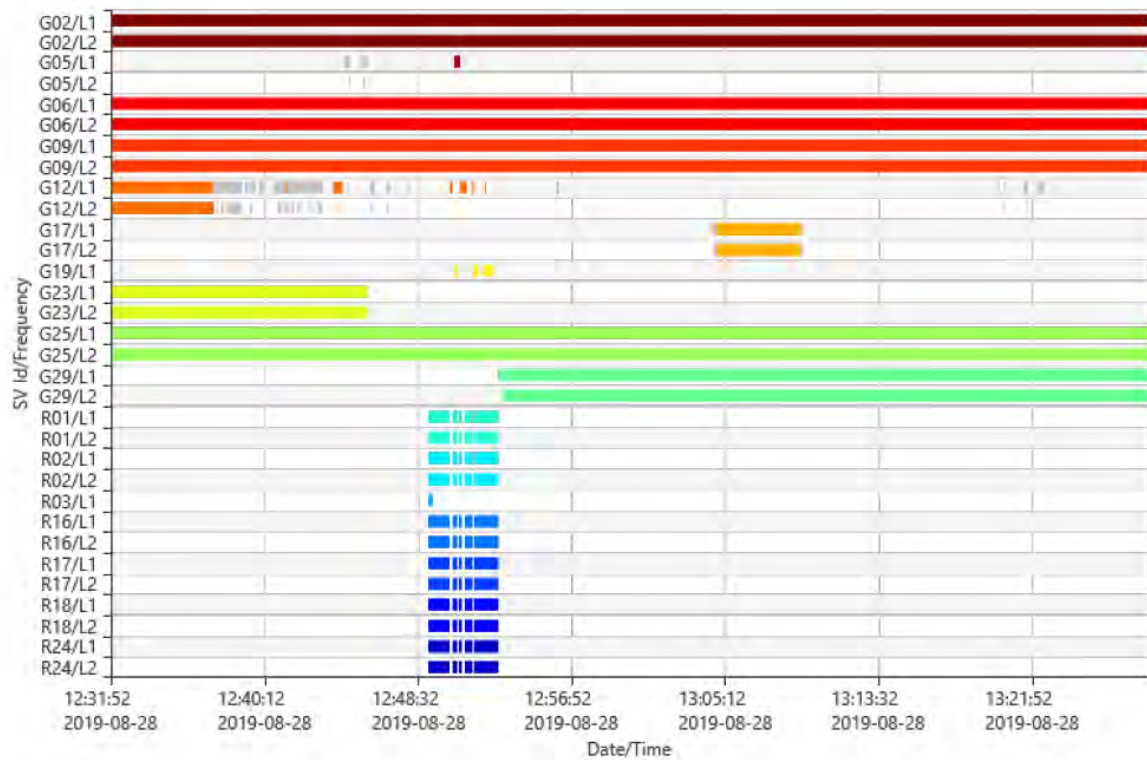


Figure D-6 - Signals tracked by receiver P24 in St. Catharines

Appendix E: Photos from the Bridges









